

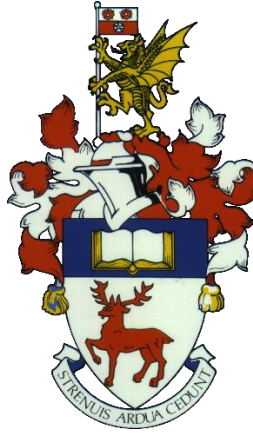
University of Southampton Research Repository ePrints Soton

Copyright © and Moral Rights for this thesis are retained by the author and/or other copyright owners. A copy can be downloaded for personal non-commercial research or study, without prior permission or charge. This thesis cannot be reproduced or quoted extensively from without first obtaining permission in writing from the copyright holder/s. The content must not be changed in any way or sold commercially in any format or medium without the formal permission of the copyright holders.

When referring to this work, full bibliographic details including the author, title, awarding institution and date of the thesis must be given e.g.

AUTHOR (year of submission) "Full thesis title", University of Southampton, name of the University School or Department, PhD Thesis, pagination

UNIVERSITY OF SOUTHAMPTON



FACULTY OF ENGINEERING AND THE ENVIRONMENT

National Centre for Advanced Tribology at Southampton (nCATS)

**Wetting of Textured Surfaces and their Application to
Drag and Friction Reduction**

by

Ben Peter Lloyd

Thesis for the degree of Doctor of Philosophy

December 2015

UNIVERSITY OF SOUTHAMPTON

ABSTRACT

FACULTY OF ENGINEERING AND THE ENVIRONMENT

National Centre for Advanced Tribology at Southampton (nCATS)

Thesis for the degree of Doctor of Philosophy

Wetting of Textured Surfaces and their Application to Drag and Friction Reduction

Ben Peter Lloyd

The presence of a layer of gas trapped at a submerged surface leads to significant drag reductions in laminar and turbulent flows. However this gas is easily lost. The focus of this work is to characterise the wetting properties of a range of surfaces made of hydrophobic cavities and where possible to modify the surfaces to increase the lifetime of the gas and optimise for drag and friction reduction. For the majority of this work surfaces are made using a templated electrodeposition method which can produce a range of cavity widths and heights in a close packed arrangement.

The wetting properties of hydrophobic surfaces consisting of micron sized cavities are investigated which shows the surface displays the 'petal effect'; high contact angle and high contact angle hysteresis, and has the ability to form hexagonally shaped droplets due to the close packed arrangement of the cavities. This surface is then modified to allow the top up of the gas as it dissolves and the determination of the wetted area and using electrochemical methods. This work is built upon to allow full reintroduction of gas from a fully wetted state using much larger cavities.

The wetting of sub-micron sized cavities is investigated using atomic force microscopy which reveals the presence of nanobubbles within the cavities. These have an exceptionally long lifetime and the cavity structure is shown to prevent coalescence. The frictional properties of this surface, as well as flat hydrophobic and hydrophilic surfaces are investigated using a custom built tribometer which simulates conditions found in microelectromechanical systems.

Table of Contents

Table of Contents	i
DECLARATION OF AUTHORSHIP	v
Acknowledgements	vii
Chapter 1: Introduction	1
1.1 Thesis Overview	1
1.1.1 Superhydrophobic Surfaces	1
1.1.2 Nanobubbles	1
1.1.3 Common Themes	2
1.2 Chapter Overviews	3
Chapter 2: Literature Review	5
2.1 Wetting and Superhydrophobic Surfaces	5
2.1.1 The Fundamentals of Capillarity and Wetting	5
2.1.2 Surface Tension & Energy	5
2.1.3 The Young Equation	6
2.1.4 Laplace Pressure and Curvature	7
2.1.5 Rough Surfaces	7
2.1.6 Contact Angle Hysteresis	9
2.1.7 Predicting the Wetting State and Wetting Transitions	10
2.1.8 Dissolution of the Gas Film	10
2.1.9 Dewetting; Reversing the Cassie-Wenzel Transition	11
2.1.10 Fabrication of Superhydrophobic Surfaces	15
2.1.11 Applications	17
2.1.12 Summary of Section 1	18
2.2 Surface Nanobubbles	19
2.2.1 Introduction	19
2.2.2 Nucleation	20
2.2.3 Detection	22
2.2.4 Stability	22

2.2.5	The Nanobubble Bridging Capillary Force	25
2.2.6	Application.....	25
2.2.7	Summary of Section 2	26
2.3	Slip, Drag and Friction.....	26
2.3.1	Introduction.....	26
2.3.2	Intrinsic Slip on Flat Solid Surfaces without a Gas Layer	27
2.3.3	Flow Over a Lubricating Gas Layer	29
2.3.4	Drag Reduction	29
2.3.5	Effect of Superhydrophobic Surface Geometry on Slip Length	30
2.3.6	Experimental Evidence	31
2.3.7	Slip in tribology.....	33
2.3.8	Summary of Section 3	37
2.4	General Conclusion of Literature Review	37
2.5	References.....	39
Chapter 3:	Materials and Methods	45
3.1	Electrochemical	45
3.1.1	Reference Electrode	45
3.1.2	Electrochemical Deposition.....	45
3.2	Templated Electrodeposition	46
3.3	Contact Angle Measurement	47
3.4	Spin Coating.....	47
3.5	Scanning Electron Microscopy	48
3.6	Atomic Force Microscopy	48
3.7	References.....	48
Chapter 4:	Wetting of Surfaces made of Hydrophobic Cavities	49
4.1	Introduction.....	49
4.2	Experimental.....	51
4.3	Results and Discussion.....	51
4.4	Conclusions.....	57
4.5	References.....	58

Chapter 5:	Active Gas Replenishment and Sensing of the Wetting State in a Submerged Superhydrophobic Surface	59
5.1	Introduction	59
5.2	Experimental	61
5.3	Results and Discussion	63
5.4	Conclusions	70
5.5	References	70
Chapter 6:	Full Dewetting of a Cavity	73
6.1	Introduction	73
6.2	Results and Discussion	75
6.2.1	Dewetting	82
6.2.2	Lower Dewetting.....	82
6.2.3	Upper Dewetting	84
6.2.4	Measurement of Wetted Area	86
6.2.5	Loss of Gas Volume.....	87
6.3	Conclusion.....	88
6.4	References	89
Chapter 7:	Control of Nanobubble Size, Shape and Location by Sub-Micron Cavity Structures	91
7.1	Introduction	91
7.2	Experimental.....	93
7.3	Conclusion.....	104
7.4	References	104
Chapter 8:	Effect of Hydrophilic, Hydrophobic & Nanostructured Surfaces and Presence of Nanobubbles on Friction in a MEMS Contact.....	107
8.1	Introduction	107
8.2	Experimental	111
8.3	Results and Discussion	118
8.3.1	Hydrophilic/Hydrophilic & Hydrophilic/Hydrophobic No Nanobubbles.....	118

8.3.2	Flat Hydrophilic/Hydrophobic Nanobubbles & No Nanobubbles.....	120
8.3.3	Hydrophilic/Nanostructured Nanobubbles & No Nanobubbles.....	120
8.3.4	Hydrophobic/Hydrophobic & Hydrophilic/Hydrophobic No Nanobubbles	121
8.3.5	Analysis of Surfaces Post-Testing	122
8.4	General Discussion and Conclusion.....	123
8.5	References.....	124
Chapter 9:	Conclusions and Future Work	127
9.1	Conclusion of Results Chapters	127
9.1.1	General Conclusion on Superhydrophobic Work Chapters 4, 5 & 6.....	127
9.1.2	General Conclusion on Nanobubble Work Chapters 7 & 8.....	128
9.2	Future Work.....	128
9.2.1	Superhydrophobic Surfaces	128
9.2.2	Nanobubbles	129
9.3	References.....	130
List of References	133

DECLARATION OF AUTHORSHIP

I, Ben Peter Lloyd

declare that this thesis and the work presented in it are my own and has been generated by me as the result of my own original research.

I confirm that:

1. This work was done wholly or mainly while in candidature for a research degree at this University;
2. Where any part of this thesis has previously been submitted for a degree or any other qualification at this University or any other institution, this has been clearly stated;
3. Where I have consulted the published work of others, this is always clearly attributed;
4. Where I have quoted from the work of others, the source is always given. With the exception of such quotations, this thesis is entirely my own work;
5. I have acknowledged all main sources of help;
6. Where the thesis is based on work done by myself jointly with others, I have made clear exactly what was done by others and what I have contributed myself;
7. Parts of this work have been published as:

Lloyd, B. P.; Bartlett, P. N.; Wood, R. J. Wetting of Surfaces made of Hydrophobic Cavities. *Langmuir* 2015, 31 (34), 9325-9330.

Signed:

Date: 18th December 2015

Acknowledgements

Firstly I would like to thank my academic supervisors; Philip Bartlett and Robert Wood. Your support has been extremely valuable throughout this work. At times this support has taken the form of scientific discussion of and at others it has been in the form of trust to allow me steer the direction of the Thesis for which I am very grateful.

In parts of this work I collaborated with other researchers. I would like to thanks Orestis Androitidis for help with the AFM imaging in Chapters 4 and 7. I would also like to thank Jason Zhang and Tom Reddyhoff of Imperial College London for giving me access to their MEMS tribometer and helping with testing in Chapter 8. I'd also like to thank the many members of the Bartlett and nCATS groups who have helped me in the lab or in discussion.

I would like to acknowledge the many friends I have made over the course of my studies at the University of Southampton, there are too many to mention, it has been a pleasure spending this period of my life surrounded by such excellent company. To the many I have shared a rope or boulder pad with whilst rock climbing which has kept my mind fresh thanks for the belays and encouragement. I would like to thank my girlfriend Emma for her endless support and smile.

Finally I would like to give thanks to my family for their support. To my Dad for helping me develop a curious mind from a young age and find the pleasure of making things. To my Brother for competitiveness and friendship. To my Mum who sadly passed away in 2013, for her Love, patience and her desire to help those who needed it the most.

Chapter 1: Introduction

1.1 Thesis Overview

The work in this thesis seeks to deliver surfaces capable of reducing skin friction drag by trapping a layer of gas on the surface. This general aim is approached from two angles. Firstly using superhydrophobic surfaces and secondly using surface nanobubbles.

1.1.1 Superhydrophobic Surfaces

Superhydrophobic surfaces trap a layer of gas between themselves and water using hydrophobic surface textures. They have fascinated the research community as a way to significantly reduce skin friction drag; the low viscosity gas layer can be sheared with ease leading to significant drag reductions. This effect has been well studied over the past decade in a range of conditions using laminar and turbulent flows and agrees well with theoretical predictions based on the superhydrophobic surface geometry. In well controlled conditions and for short periods of time superhydrophobic surfaces have shown impressive results. However their fragile gas layer is easily removed through spontaneous wetting transitions promoted by high static or transient pressure and also through dissolution. Larger scale tests of superhydrophobic surfaces have shown conflicting results; these tests have neglected to measure the state of the gas film and have no method to reintroduce gas once it has been lost. If the drag reducing effect of superhydrophobic surfaces which has been demonstrated in the lab could be applied to large scale water systems such as in pipes and the hulls of ships significant efficiency savings could be made.

The aim of the work looking at superhydrophobic surfaces is to develop methods to reintroduce gas to the surface and to measure the volume of gas present at the surface.

1.1.2 Nanobubbles

Nanobubbles are small gaseous domains up to 1 μm in width and 100 nm in height found on hydrophobic surfaces when submerged in water. Only first observed in the year 2000, many properties of nanobubbles remain unexplained such as their very long lifetime and large contact angle. There have been many suggestions that nanobubbles could reduce drag. However the effect - if present - should be much smaller than that found at superhydrophobic surfaces. Many researchers have modelled or considered the theory behind this but convincing experimental evidence is lacking. A considerable advantage of drag reduction using nanobubbles would be their

Chapter 1

surprisingly long lifetime, ease of nucleation and low profile. If nanobubbles do have the ability to reduce drag they could be used in small scale fluid systems such as MEMS devices.

The aim of the work looking at nanobubbles seeks to generate surfaces which can maximise the potential for drag reduction and then to test the frictional properties of the surfaces.

1.1.3 Common Themes

The general theme of this thesis is to allow water to flow past surfaces with a lower energy cost. In large scale systems such as ships this would be manifested as increased speed through the water and lower fuel consumption, particularly relevant to current efforts to reduce both the money spent on fuel and the volume of harmful emissions when it is burnt. On a smaller scale MEMS systems could feel a reduction in friction between moving parts and in microfluidic systems faster flow rates could be achieved.

For both of these themes surfaces textured on a micro and nano scale are used to trap a gas film or bubbles at the surface. These surfaces are mostly made using a technique called templated electrodeposition whereby a metal is electrodeposited around a template of spheres in a close packed arrangement to a desired height. The spheres can then be removed to reveal an array of cavities. The size of spheres, the height of deposition and surface modification with self assembled monolayers all can be tailored to create the desired surface.

The outline of this Thesis is shown in figure 1.1, highlighting the two strands of results chapters. Superhydrophobic surfaces are considered in Chapters 4, 5 and 6 and nanobubbles in Chapters 7 and 8.

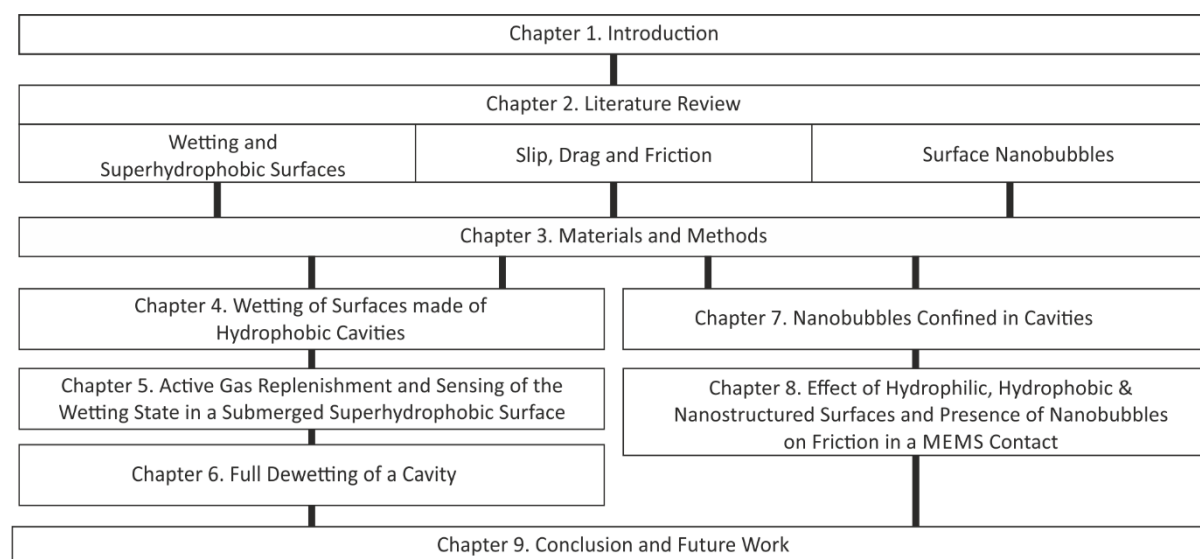


Figure 1.1: Thesis Outline

1.2 Chapter Overviews

Chapter 2 Literature Review

The Literature review discusses previous work relevant to this Thesis and is divided in to three sections. Section 1 discusses the fundamentals of surface tension, wetting and super hydrophobicity. Section 2 discusses nanobubbles; how they can be nucleated and detected, and how their physics differs from macro sized bubbles. Section 3 discusses the phenomena of slip and how it could relate to reductions in drag and friction in fluidic systems.

Chapter 3 Materials and Methods

The general methods and materials used throughout this work are listed. To achieve the micro and nano sized surface textures used in chapters 4, 5, 6 and 8 a templated electrodeposition based method is used which discussed in detail here.

Chapter 4 Wetting of Surfaces made of Hydrophobic Cavities

Hydrophobic cavity structures are made and the wetting properties are investigated. Measurement of the advancing and receding contact angles shows the surface displays the 'petal effect'. Theoretical models of the wetting are discussed and show good agreement with the experimental results.

Chapter 5 Active Gas Replenishment and Sensing of the Wetting State in a Submerged Superhydrophobic Surface

The surface used in chapter 4 is modified for measurement of the wetted area, which shows the trapped gas readily dissolves into the surrounding liquid. The gas within the cavities is topped up by electrolytic splitting of water into hydrogen gas.

Chapter 6 Full Dewetting of a Cavity

The work of chapter 5 is built upon to allow the total dewetting of the cavities once all of the gas has been removed. A new surface design is introduced which can reliably nucleate gas at the base of cavities which can be grown to fully dewet the cavity.

Chapter 7 Nanobubbles Confined in Cavities

An atomic force microscopy study of a range of surfaces covered in sub-micron cavities is undertaken which shows the presence of nanobubbles within the cavities when it is submerged in water. The shape of the nanobubbles varies with the surface structure. Increased nucleation stability is observed as well as resistance to coalescence.

Chapter 1

Chapter 8 Effect of Hydrophilic, Hydrophobic & Nanostructured Surfaces and Presence of Nanobubbles on Friction in a MEMS Contact

A custom built tribometer which simulates conditions found in microelectromechanical devices is used to test hydrophilic, hydrophobic and the nanostructured surface which supports nanobubbles from chapter 7 in water lubricated conditions. Hydrophobic surfaces show the lowest friction throughout a range of sliding speeds.

Chapter 9 Conclusions and Future Work

Conclusions of Chapters 4 to 8 are discussed and areas in future work could be conducted are highlighted.

Chapter 2: Literature Review

This Chapter reviews the literature relevant to the work in the Thesis and is composed of three sections. 1: Wetting and Superhydrophobic Surfaces, 2: Surface Nanobubbles and 3: Slip, Drag and Friction.

2.1 Wetting and Superhydrophobic Surfaces

This section of the literature review considers the fundamentals of surface tension, wetting and capillarity, and how these can explain the observed properties of superhydrophobic surfaces.

2.1.1 The Fundamentals of Capillarity and Wetting

Wetting and capillarity is the study of interfaces between phases. The ground was laid in the early 19th century by Thomas Young¹ and Pierre Simon Laplace², who recognised the importance of surface tension and curvature. More recently the study of this area has profited greatly from advances in micro and nano structuring techniques, allowing greater control of wetting properties.

2.1.2 Surface Tension & Energy

The origin of surface tension is found in the cohesive forces between molecules *eg.* hydrogen bonding and Van der Waals interactions. In the bulk, any given molecule will feel these forces pulling from every direction leading to no net force. However a molecule on the surface will only feel half of these forces pulling from the direction of the bulk which leads to the driving force for interfaces to reduce their areas.

Every interface has an associated energy with its formation or destruction, be it solid-liquid, solid-gas, liquid-gas or liquid-liquid, equation 2.1. However, only the liquid-gas and liquid-liquid interfaces are deformable, allowing it to find its lowest energy state by changing its shape.

Depending on the problem in hand it can be useful to frame it in terms of surface energy (J m^{-2}), equation 1 or surface tension (N m^{-1}) equation 2.2 which given the symbol γ .

The work done, W to change the area of an interface dA with surface tension γ , is:

$$dW = \gamma dA \quad (2.1)$$

The Force, F needed to move an interface of length L is:

$$F = \gamma L \quad (2.2)$$

2.1.3 The Young Equation

Two distinct regimes of wetting can occur when a drop of water is placed on a solid surface. Either the liquid spreads over the surface, creating a thin film, or the water beads up in to a ball from which a definite contact angle (θ), the angle between solid-gas and liquid-gas interfaces, can be measured as shown in figure 1. In this second regime we define surfaces where contact angles $< 90^\circ$ as *hydrophilic* and $> 90^\circ$ as *hydrophobic*. Generally surfaces where the contact angle exceeds 150° are known as *superhydrophobic* however there is debate to whether other factors such as small contact angle hysteresis (difference between the contact angle of the advancing and receding edges of the drop) should also considered.

Using the Young equation (equation 2.3) the contact angle formed on a flat surface can be derived from a force balance approach. Forces being exerted on the three phase contact line (black circle in figure 2.1) which are parallel to the surface must sum to zero if the system is at equilibrium. The perpendicular force exerted by the liquid-gas interface is balanced by the solid surface which is assumed to be inflexible.

Therefore:

$$\gamma_{sg} = \gamma_{sl} + \gamma_{lg} \cos\theta \quad (2.3)$$

Where subscript sg refers to solid-gas, sl to solid-liquid, lg to liquid gas and θ to the contact angle.

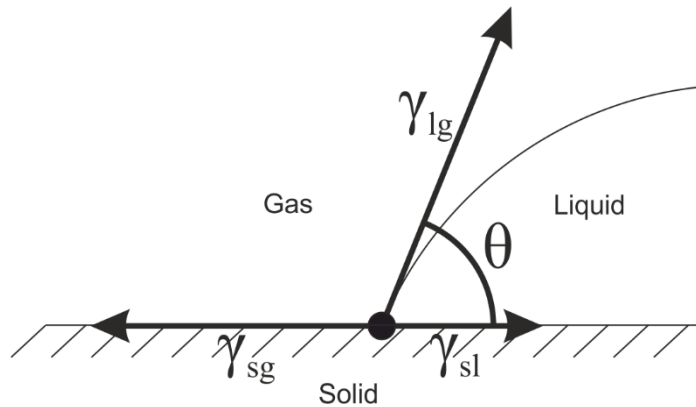


Figure 2.1 Derivation of the Young equation from the force balance approach.

2.1.4 Laplace Pressure and Curvature

Surface tension leads to a pressure difference generated between the inside and outside of a curved interface and is known as the Laplace pressure, equation 2.4.

$$\Delta p = \gamma \left(\frac{1}{r_1} + \frac{1}{r_2} \right) \quad (2.4)$$

Where r_1 and r_2 are the radii of curvature of the interface. Bubbles and drops are often spherical, where r_1 and r_2 are equal so that equation 2.4 simplifies to:

$$\Delta p = \frac{2\gamma}{r} \quad (2.5)$$

2.1.5 Rough Surfaces

The Young equation holds for flat surfaces, however when the surface is roughened or textured the situation changes. Two wetting states can be envisaged when a drop is deposited on to a heavily roughened surface. In one the liquid could penetrate the features completely wetting the surface, in another the water could sit on top of them with a gas layer underneath; these two situations were approached by Wenzel in 1936³ and Cassie and Baxter in 1944⁴ respectively, figure 2.

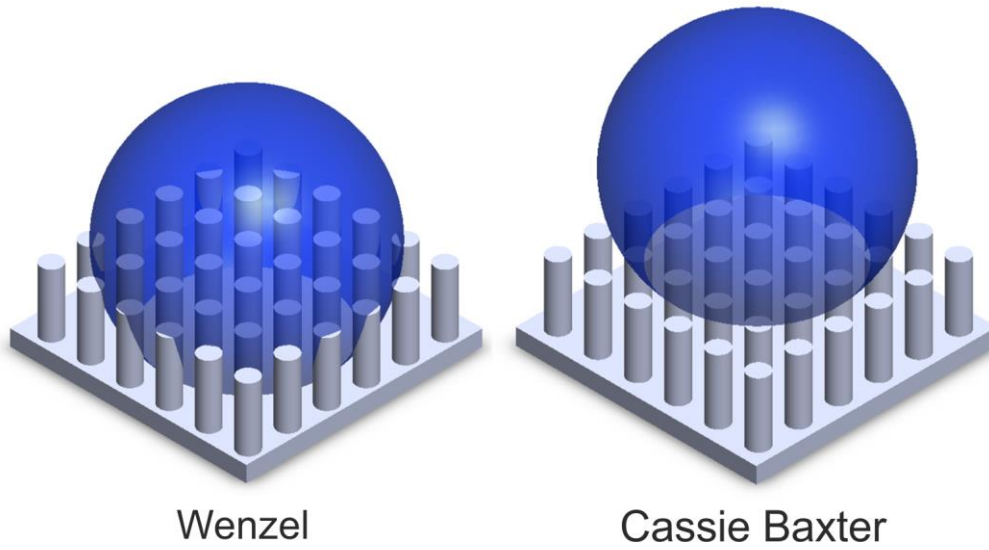


Figure 2.2 A drop of water on a surface made of a square array of posts. The drop in the Wenzel state penetrates the space between the posts and wets the bottom of the surface. In the Cassie-Baxter state the drop sits on top of the posts with cushion of air beneath it.

2.1.5.1 Wenzel

The first regime where the surface is completely wetted was considered by Wenzel³. The surface is characterised by a roughness factor (R_f) which is the actual over the projected area, whilst the surface chemistry is kept homogenous and θ is the contact angle of the solid when the surface is flat. The contact angle due to the roughness according to the Wenzel equation is θ_w . This takes into account the change in force at the three phase contact line which is longer as it follows the roughness of the surface.

$$\cos\theta_w = R_f \cos\theta \quad (2.6)$$

The Wenzel equation predicts that the degree of roughness will amplify the wetting character of the surface *ie.* hydrophilic surfaces become more hydrophilic and hydrophobic more hydrophobic. The Wenzel equation of wetting is plotted in figure 2.3 a).

2.1.5.2 Cassie-Baxter

Cassie and Baxter (often abbreviated to Cassie) considered a flat surface where the surface energy varied throughout⁴. When the liquid is assumed not to enter the roughness features the area beneath the drop is composed of partly solid-liquid and partly liquid-gas interfaces, which is the case in a superhydrophobic surface⁴. The solid fraction of the surface is: ϕ_s . Here we assume the

contact angle on the gaseous regions to be 180° and the solid fraction to have contact angle θ . The contact angle predicted by the Cassie-Baxter equation, θ_c is:

$$\cos\theta_c = \Phi_s \cos\theta - (1 - \Phi_s) \quad (2.7)$$

The Cassie-Baxter equation predicts that as the solid fraction is reduced, the contact angle will increase to 180° (even if the solid fraction is itself hydrophilic.) The Cassie-Baxter model of wetting is plotted in figure 2.3 b).

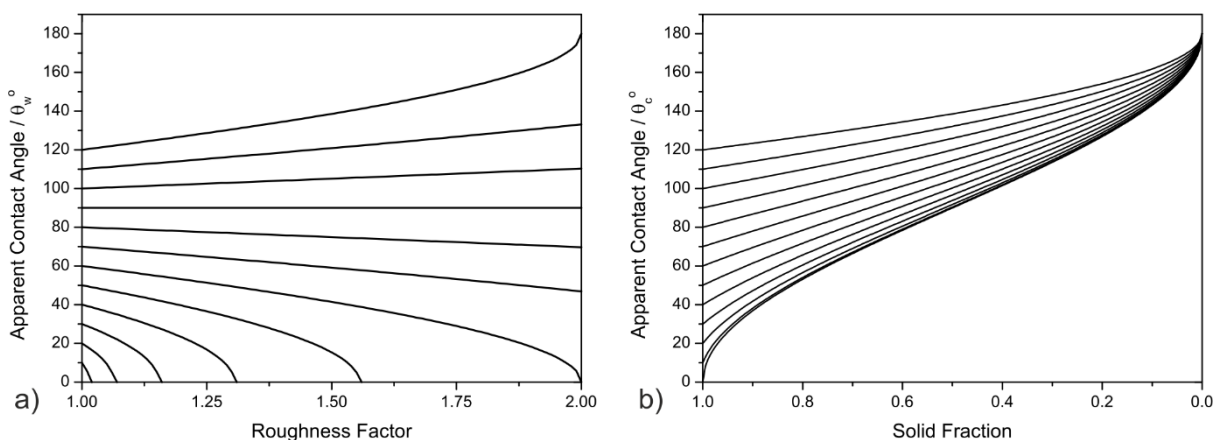


Figure 2.3 a) The Wenzel equation plotted as a function of the roughness factor showing the change in contact angle starting with a flat solid surface ($R_f = 1$) and increasing the roughness factor. B) The Cassie-Baxter equation plotted as a function of the solid fraction showing the change in contact angle starting with a flat solid surface ($\Phi_s = 1$) and decreasing the solid fraction.

2.1.6 Contact Angle Hysteresis

On a real surface there is always a range in which the contact angle falls, the upper and lower bounds can be found by advancing and receding the three phase contact line over the surface. The contact angle hysteresis is the difference between these two values, and determines the degree of mobility a drop will have on the surface. Contact angle hysteresis is caused by chemical and structural heterogeneity causing 'pinning' of the three phase contact line.

Typically superhydrophobic surfaces have a very small contact angle hysteresis, which leads to a very small force being required to initiate drop movement. A tiny tilt to the substrate will allow the

drop to roll off, picking up any debris on the surface and taking it with it, this is known as the self-cleaning or the lotus effect⁵.

2.1.7 Predicting the Wetting State and Wetting Transitions

The contact angles of the Cassie and the Wenzel wetting states can be predicted using the discussed equations. However, they do not give an insight into which wetting state will actually be taken when a drop is placed on a surface. This is heavily dependent on the particular shape and structure of the solid surface as well as the surface energies.

Crucially to maintain the Cassie state, the pressure of the liquid (whether this be from static, transient pressure) must be less than the capillary pressure acting on the side walls of the posts⁶, above this pressure wetting state will transition to the Wenzel state. The following equations show the maximum liquid pressure posts (equation 2.8), grates (equation 2.9) and holes (equation 2.10) can withstand before the Cassie to Wenzel wetting transition occurs: by dividing the capillary forces generated in a unit cell of the surface by the area of the cell. Where φ is the gas fraction, D is the diameter of the posts, L is the pitch of the grates and r is the radius of the hole.

$$\text{Circular Posts square array} \quad p = \frac{4 \gamma (1 - \varphi) \cos \theta}{D} \quad (2.8)$$

$$\text{Grates} \quad p = \frac{2 \gamma \cos \theta}{L (1 - \varphi)} \quad (2.9)$$

$$\text{Holes} \quad p = \frac{2 \gamma \cos \theta}{r} \quad (2.10)$$

This means the larger the gas fraction and spacing between features the lower the pressure which leads to the Cassie to Wenzel transition.

2.1.8 Dissolution of the Gas Film

When a superhydrophobic surface is submerged underwater and the gas is no longer connected to the atmosphere the gas may dissolve into the surrounding water and transition from the Cassie to the Wenzel state. Both Lv *et al.*⁷ and Muchen *et al.*⁸ presented a model to approximate the dissolution of trapped gas, equation 2.11. The model assumes that the diffusion is 2 rather than 3 dimensional, however shows reasonable agreement with experiment.

Where V is air volume, t is time, k_p is the mass transfer coefficient across the interface, A is the interface area, p_H is the hydrostatic pressure, γ is the liquid/gas surface tension, R is the radius of curvature of the interface, p_{atm} is atmospheric pressure, k_H is the Henrys' constant, c is the concentration of dissolved gas.

$$\frac{dV(t)}{dt} = -k_p A(t) \left[p_H - \frac{\gamma}{R(t)} + p_{\text{atm}} - k_H c \right] \quad (2.11)$$

Both Lv *et al.* ⁷ and Muchen *et al.* ⁸ showed that there are two distinct phases of the dissolution: stage 1 where the contact line remains pinned at the top of the edge of the cavity and the curvature of the interface changes as gas dissolves and stage 2 where contact line starts to slide down the side of the cavity and the curvature remains constant (and so $A(t)$ and R dependant on geometry and local contact angle of surface) dV/dt is smallest at end of phase 1 where A and R become constant so offers the highest resistance to dissolution.

This reduces to the well known relation for capillary rise by finding maximum depth at which $dV/dt = 0$ so no diffusion occurs⁸, shown for a cylindrical cavity in equation 2.12. Where H_c is the maximum depth (where $dV/dt = 0$), θ is the contact angle, r is the radius of the cavity, ρ is the density of the liquid, and g is the acceleration due to gravity.

$$H_c = \frac{2\gamma \cos \theta}{r \rho g} \quad (2.12)$$

This shows that when the dissolved gas in the water is in equilibrium with the atmosphere the critical depth is the point where hydrostatic pressure overcomes Laplace pressure – the same pressures in equations 2.8, 2.9 and 2.10. For surfaces with a geometry capable of generating a significant drag reduction this critical depth is generally less than 10 cm.

2.1.9 Dewetting; Reversing the Cassie-Wenzel Transition

The Wenzel mode of wetting is a thermodynamically lower energy state than the Cassie mode. Therefore reversing the Cassie to Wenzel transition is energetically unfavourable and must require some external input of energy. The onset of the wetting transition or gas dissolution can be delayed by making the distance between surface structures smaller and the solid fraction larger. However

as discussed later in this Chapter, when using a superhydrophobic surface to maximise drag reduction the structures should be spaced as far apart and with the smallest solid fraction possible. This means that an active mechanism to replenish gas to surfaces is highly desirable.

Dewetting of individual drops has been shown to be possible through vibration⁹ and heating¹⁰, however neither are appropriate for submerged use.

2.1.9.1 Dewetting Surface by Kim *et al.*

Despite the demand, only one group has managed to create a surface which can reverse the wetting transition, led by CJ Kim^{11, 12}. A critical analysis is made of their approach to this problem.

In their work surface geometries structured with post and grating geometries used. To dewet the surface from the Wenzel state to the Cassie state they reasoned that gas must spread laterally throughout the surface *ie.* through the posts and along the gratings, rather than vertically *ie.* leaving the surface as bubbles figure 2.4 a). To achieve this they showed that the capillary pressure of lateral spreading must be less than that of vertical spreading.

By considering the geometries involved and the contact angles of the materials used the scenarios in which lateral spreading occurs could be identified and were shown graphically as minimum height to pitch (H/L) ratio of the features (figure 2.4 b). They also identified the height to pitch ratio at which the bubble collapses prematurely due to sagging (red line in figure 2.4 b) - where H/L is so low that the meniscus reaches the base of the sample between the posts or gratings.

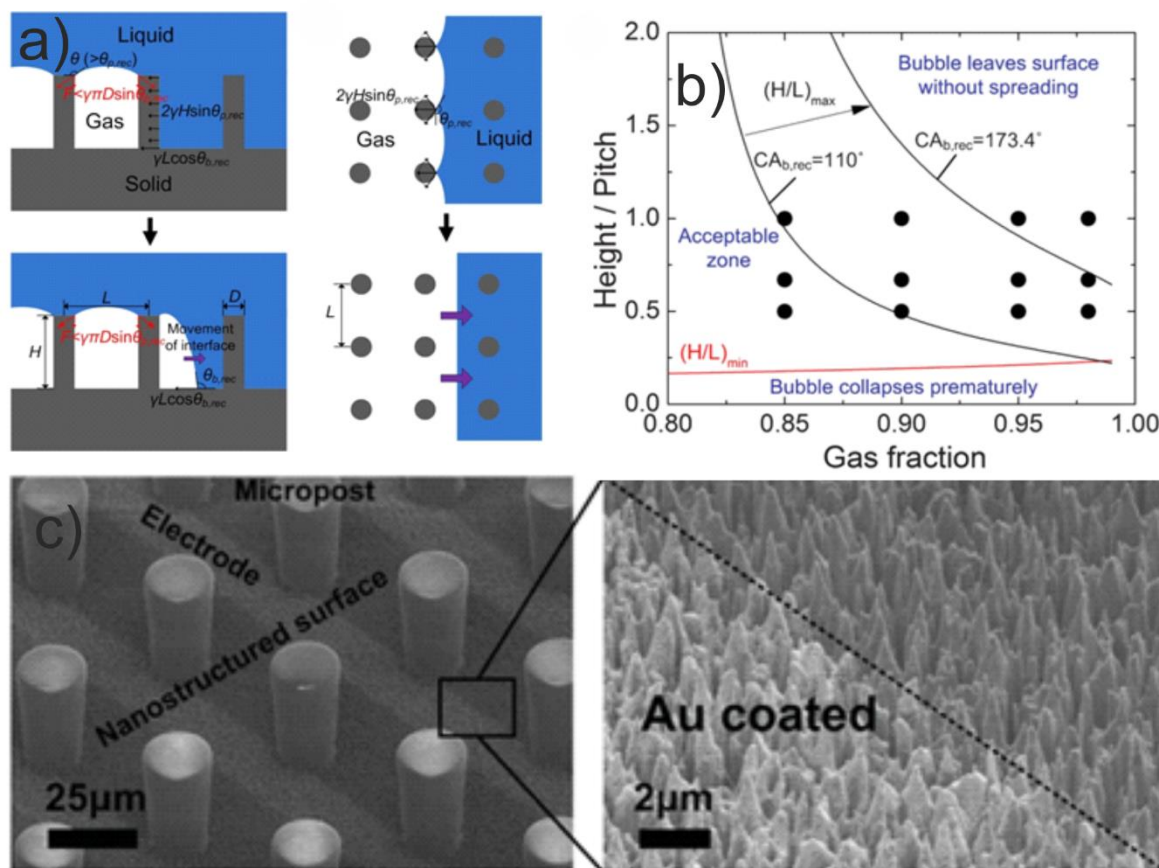


Figure 2.4 The surface made by Lee and Kim¹¹. a) schematic showing lateral and vertical pressures generated in the surface. b) Graph showing where lateral spreading will occur in a post geometry surface plotted as height/pitch against gas fraction. c) A scanning electron microscope image of the surface with a close up of the nanostructured base.

As demonstrated in figure 2.4 b), by increasing the contact angle of the base of their surface (labelled $CA_{b,rec}$ in figure 2.4) from 110° – a flat hydrophobic surface to 173.4° – a nanostructured superhydrophobic surface, the region in which lateral spreading occurs is increased. For this reason they made a surface which combines two layers of structural hierarchy; micron sized posts or gratings with a nanostructured base; both are superhydrophobic in their own right (figure 2.4 c). To generate gas regions of the base were coated in gold which acted as an electrode from which to generate hydrogen via electrolysis.

The key result from their work was that they showed that using the nanostructured base, the surface could be successfully dewetted, figure 2.5 b). However if the nanostructured base itself became wetted the surface this functionality was lost and the surface would not dewet figure 2.5 c). This is a very undesirable situation in real world conditions as the only way to recover the functionality of the surface would be to remove the surface from the water and let it dry.

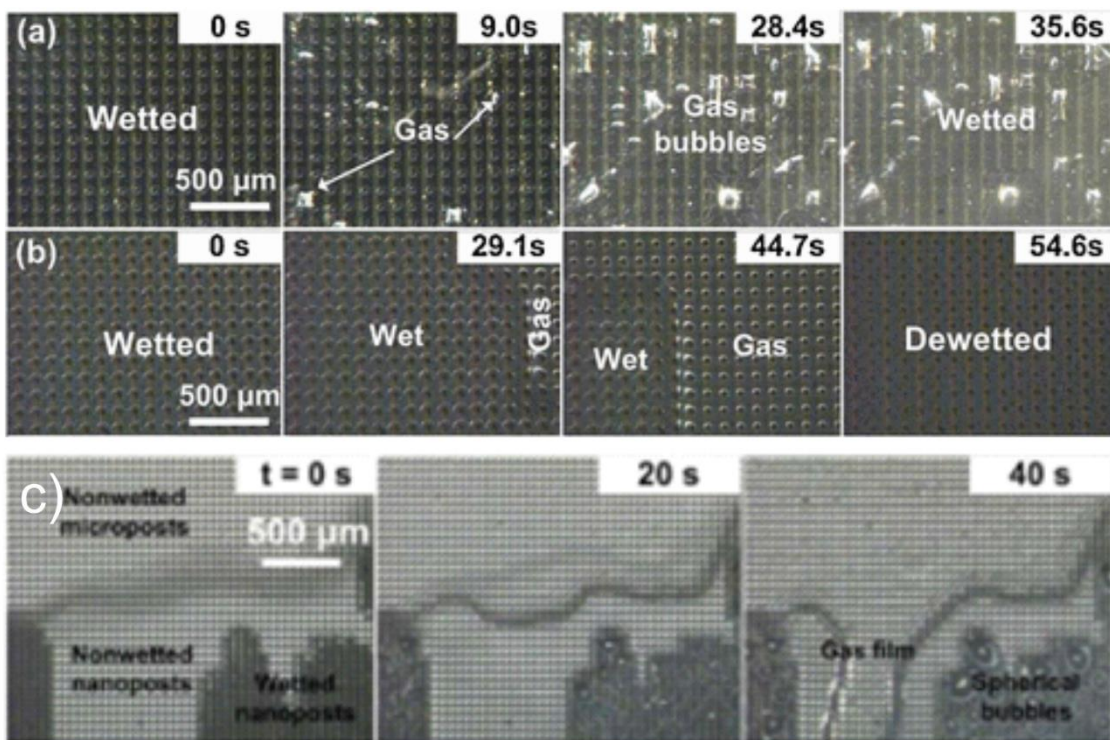


Figure 2.5 The dewetting behaviour of the surfaces made by Lee and Kim^{11, 12}. a) Flat base, 100 μm pitch, 50 μm height and 95% gas fraction. The hydrogen gas leaves the surface as bubbles and does not spread throughout the posts. b) Nanostructured base, 100 μm pitch, 50 μm height and 95% gas fraction. c) Images showing that if the nanostructured base becomes wetted the gas leaves the surface as bubbles and does not dewet (surface geometry unspecified).

In figure 2.4 b) there are clearly regions in which their criteria for lateral spreading is fulfilled with a flat surface with contact angle 110° and the nanostructured base is not required. As discussed the nanostructured base has the considerable down fall that if it becomes wetted the dewetting functionality of the surface is lost. Therefore if one could produce a surface which did not rely on a nanostructured base it would be both superior in terms of functionality and much easier to manufacture. It is interesting to note however that results for these areas using a flat base are not

presented. It seems unlikely that these conditions were not tested so could hint that for some reason they did not work.

2.1.10 Fabrication of Superhydrophobic Surfaces

Superhydrophobic surfaces can be divided into two groups: highly roughened quasi random *eg.* electrospun plastics¹³ or designed with a repeating unit cell *eg.* a square array of posts¹⁴.

The first group of quasi random surfaces have the advantage of being cheap, mass producible, and generally don't require specialist equipment¹⁵. The second group are more expensive and thus only small ($< 1 \text{ cm}^2$) areas are patterned, however they have much more suited to the understanding of the wetting phenomena as the surface structure is known. Certain applications (*eg.* the reduction of drag) are very sensitive to the spacing between surface features and therefore precisely controlled surfaces are often employed¹⁶.

2.1.10.1 Quasi-Random

The most famous quasi-random surface is probably the leaf of the lotus plant⁵, which is covered in a two tier hierarchy of larger protrusions (papillae) on which smaller wax crystals are found. The double layer of roughness has been mimicked by many authors and is an effective way of reducing the solid fraction of the surface. The structure acts to keep the leaf clean from contamination; droplets collect dirt then easily run off. Figure 2.6 shows a range of quasi-random surface structures and how they are made.

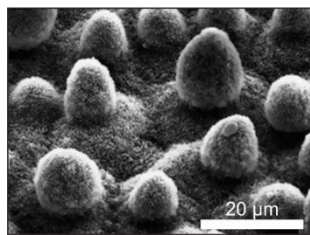
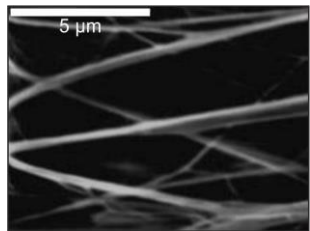
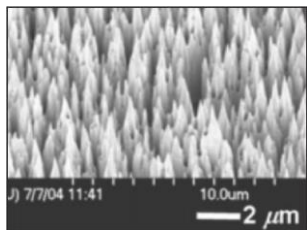
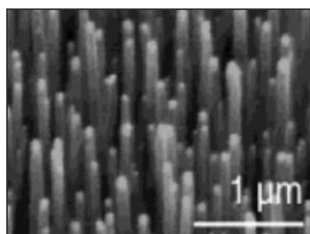
Image	Description	Method of Manufacture	Authors & Paper
	Lotus leaf	Grown from the <i>Nelumbo nucifera</i> plant	Barthlott & Neinhuis ⁵
	Teflon fibres	Stretched Teflon tape	Zhang et al. ¹⁷
	Needles (black silicon)	Reactive ion etched silicon coated with teflon	Choi and Kim ¹⁸
	Carbon nanotubes	plasma enhanced chemical vapour deposition, treated with Teflon	Lau et al. ¹⁹

Figure 2.6 A table showing a range of quasi-random superhydrophobic surfaces

2.1.10.2 Rationally Designed Surfaces with Repeating Unit Cells

More control of surface features allows more control of the surface wetting features, a few interesting examples are shown which capitalise on this figure 2.7.

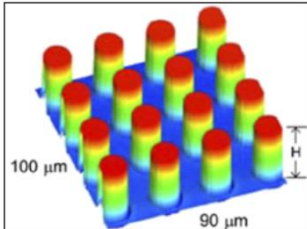
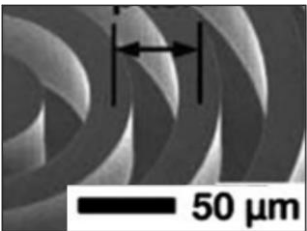
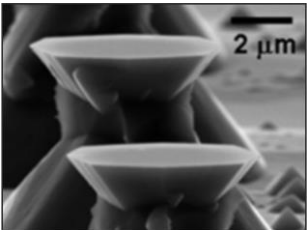
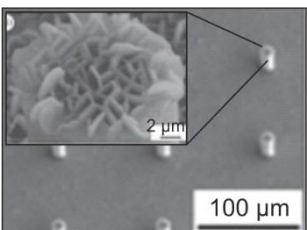
Image	Description	Method of Manufacture	Authors & Paper
	square array of circular posts	photolithography and subsequent attachment of a hydrophobic self assembled monolayer	Bhushan and Jung ²⁰
	concentric grating structures	used photolithography with a silicon wafer substrate which was spin coated with Teflon	Kim and Lee ¹⁶
	square array of overhanging silicon structures	photolithography and a series of etching steps	Cao <i>et al.</i> ²¹
	square array of posts	dental wax in a photolithographically generated cast N-hexatriacontane was evaporated on to the structures to produce a second level of hierarchy	Bhushan and Her ²²

Figure 2.7 A table showing a range of ordered, rationally designed superhydrophobic surfaces

2.1.11 Applications

2.1.11.1 Applications based on low hysteresis

Superhydrophobic surfaces have extremely low contact angle hysteresis which leads to a very small angle of tilt to initiate rolling. The most famous implication of this is the lotus or self-cleaning effect; as the drop rolls off any debris on the surface preferentially adheres to the drop and is carried away.

The low angle of tilt required to shed the water from the surface, reduces the time the drop is in contact with the surface and minimises standing water which can solve many industrially relevant problems. Anti-icing²³, anti-corrosion²⁴ and anti-bacterial²⁵ properties are often cited.

The criterion for a surface of this kind is a large contact angle and low contact angle hysteresis. To avoid wetting transitions from droplet impacts *eg.* rain, the surface features can become as small as possible (the order of 10 to 1000 nm) to increase the pressure required to transition from the Cassie to the Wenzel state. The surface features do not need to be particularly ordered to achieve this, therefore costs can be minimised by choosing a random surface geometry which can be applied as a paint or spray. A two part coating of this kind has recently become available for the domestic market in the United States which can coat fabrics, wood, metal and plastics²⁶.

2.1.11.2 Drag reduction

Recently interest has been shown in the drag reducing effect of superhydrophobic surfaces against fluid flow²⁷. Here the water molecules in contact with the gas film trapped by the surface structure, which are usually stationary for a solid surface, are free to move, this is called slip.

These kinds of drag reducing surfaces could be applied to situations where water flows past a surface for example on the hulls of ships or in pipe networks.

Superhydrophobic surfaces for drag reduction are being very actively researched and many questions must be answered before they can be applied. Initial large scale towing tank tests show a 30 % reduction in drag, and it is likely this value will be increased²⁸. A major problem is the surface transitioning from the Cassie to the Wenzel state, in which the drag reducing properties are lost¹¹. Section 3 of this chapter deals with slip and drag reduction in much more detail.

2.1.12 Summary of Section 1

Superhydrophobic surfaces have a high surface roughness and low surface energy which leads to the trapping of a gas film beneath the drop in the Cassie state. The reduced contact with the solid massively increases the contact angle.

The Cassie to Wenzel wetting transition occurs when the capillary forces are overcome by the pressure of the liquid or if the trapped gas in the surface dissolves into the surrounding liquid. It is energetically unfavourable to reverse this transition from the Wenzel to the Cassie state.

There are two promising areas in which superhydrophobic surfaces can be applied. Firstly a surface which is self-cleaning, anti-icing, anti-corrosion and anti-bacterial where the surface interacts with individual droplets which are quickly shed due to low contact angle hysteresis. These are typically made of randomly ordered but nanoscale features. Secondly a surface which reduces drag by fluid slip along the liquid-gas interface. Well controlled surface geometries outperform random ones, the larger the gas fraction and pitch the better, however this surface could easily transition from Cassie to Wenzel states, losing the low drag properties.

2.2 Surface Nanobubbles

This section of the literature review discusses experimental observations of nanobubbles, their properties and the proposed theories for how these properties arise.

2.2.1 Introduction

Surface nanobubbles are gas filled nano-sized bubbles found at solid-liquid interfaces. On flat surfaces they form spherical caps which are typically < 100 nm tall and < 1 μm in width, figure 2.8. They have been detected on many hydrophobic surfaces but never on a hydrophilic surface.

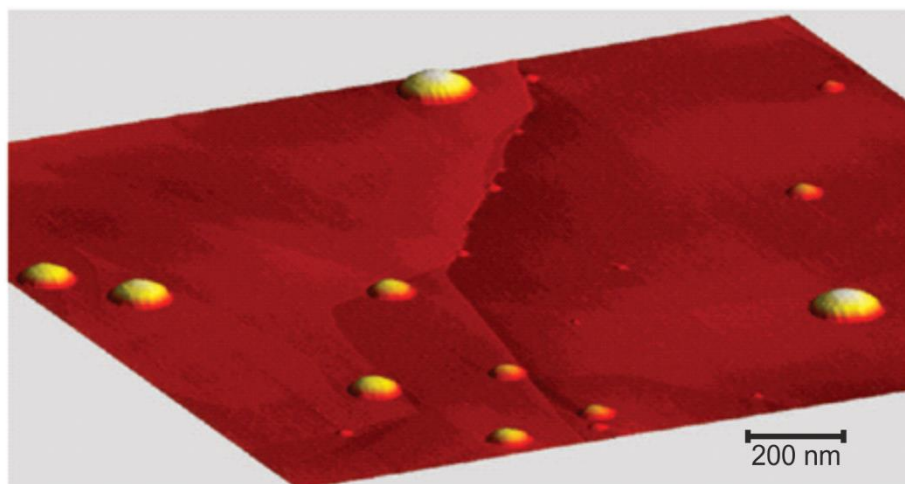


Figure 2.8 A 3d atomic force microscope image of a highly ordered pyrolytic graphite surface with nanobubbles. From Borkent *et al.*²⁹, the image dimensions are 2000 x 2000 x 40 nm and is shown to scale.

The existence of nanobubbles was first proposed by Parker *et al.* in 1994 to explain the attractive force they observed when two hydrophobic surfaces were brought within ~100 nm of one another when submerged in water³⁰. Ishida *et al.*³¹ and Lou *et al.*³² presented the first experimental observations of what were thought to be nanobubbles using tapping mode atomic force microscopy (AFM). Zhang *et al.* confirmed that the soft domains were indeed filled with gas and not some other surface contamination by distinguishing between dissolved and gaseous CO₂ using infrared spectroscopy³³.

The curvature of the liquid-gas interface implies an over pressure of the gas within the nanobubbles, according to the Laplace equation ($\Delta p = 2\gamma / r$)² which can be as high as 10 atmospheres. Bubbles of this size are not predicted to last more than a few microseconds according to classical thermodynamic models^{34, 35}; however they appear to be particularly resilient to dissolution and can last at least 10 orders of magnitude longer than this³⁶.

Equally as puzzling is the contact angle, which is found to be around 160°; much larger than in the macroscopic case^{31, 37}. The surface chemistry of the substrate does not seem to change the contact angle as one might expect from the Young equation. In some situations the contact angle has shown dependence on the radius of curvature and gas type³⁸.

2.2.2 Nucleation

Nanobubbles can be nucleated as the surface is being submerged by controlling the temperature and gas saturation of the water, which have been found to be the most important parameters for nucleation. Seddon *et al.* showed that the water must be either saturated or super-saturated for nanobubbles to be formed and the temperature must be between 33°C and 46°C; this nucleation phase space is shown in figure 2.9 where red crosses indicate nanobubbles are present. After the nucleation has occurred the system can move away from this phase space and the nanobubbles remain stable unless the water is actively degassed³⁹.

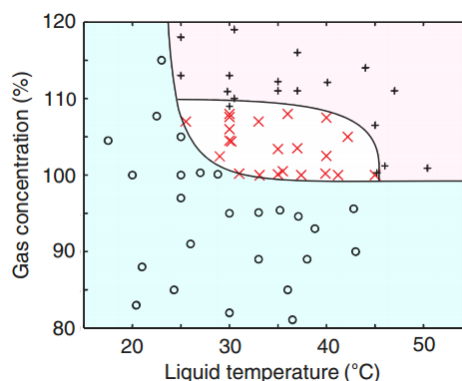


Figure 2.9 Nucleation phase space of nanobubbles on a hydrophobized silicon surface in water as a function of gas concentration and liquid temperature. Circles refer to nothing found, red crosses to nanobubbles found and pluses to micro-pancakes (From Seddon *et al.*⁴⁰).

Nucleation of nanobubbles *in situ* after the surface has been submerged can be achieved by heating the substrate.^{41, 42} The nucleation probably occurs due to the super saturation achieved by the heating (the gas is less soluble at higher temperature), although surprisingly a maximum coverage occurs at ~ 35 °C and a clear reduction occurs at ~ 40 °C; it is unclear why this happens.

A more popular route to nucleating nanobubbles which does not require determination of gas concentration and heating of the liquid is the solvent exchange method. Here, an alcohol (usually ethanol) covers the substrate first, which is then displaced by water. The mixing of the two liquids is exothermic, which raises the temperature and supersaturates the solution, forming nanobubbles.⁴³

Nanobubbles have also been formed by the electrolysis of water to gaseous hydrogen when a cathodic potential is applied to the substrate.⁴⁴ This method is not dependent on dissolved gases or temperature of the water and can result in up to 90% surface coverage when hydrogen is evolved.⁴⁵ A major finding of this work is that the nanobubbles grew to a certain size, then stopped growing, despite the potential difference still being applied. The nanobubbles produced by electrolysis are stable after the production of hydrogen has stopped; this can be explained by either another gas is influxing to the bubble or a diffusion preventing contaminant has coated the hydrogen bubble.

2.2.3 Detection

The most popular way to image nanobubbles directly is with tapping mode atomic force microscopy (AFM), in which the cantilever is vibrated, touching the substrate at the bottom of each stroke^{31, 32, 40, 45, 46, 47}. This is generally a less invasive technique than contact mode AFM imaging, where the tip traces the surface, although some groups have shown contact mode imaging to be possible.⁴⁸

Other methods, from which the presence of gas can be inferred, are rapid cryofixation/freeze fracture (figure 2.10)⁴⁹, infrared spectroscopy^{33, 36}, small angle x-ray spectroscopy⁴⁷ and quartz crystal micro balance measurements^{50, 51}, however these do not give key structural information such as radius of curvature and contact angle.

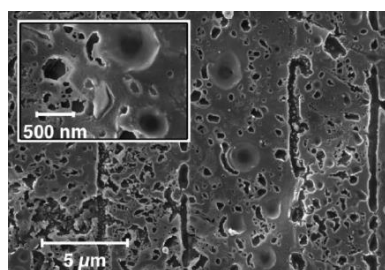


Figure 2.10 Images of nanobubbles from a scanning electron microscope image of a Pt replica of a silicon surface with nanobubbles made by the rapid cryofixation/freeze fracture method (Switkes *et al.*⁴⁹)

2.2.4 Stability

The dissolution of nanobubbles in a gas saturated solution has not been observed, the longest experiment was 5 days, the only change they observed was a small amount of Oswald ripening³⁶. The stable nature of nanobubbles is contradictory to what is predicted by current theory^{34, 35}. Several explanations have been proposed, although there is not enough evidence to form a consensus yet.

An obvious culprit could be contamination, which would lower the surface tension (reducing the internal pressure) and provide an impermeable barrier to diffusion of gas molecules^{52, 53}. It is conceivable that any insoluble contaminant would be concentrated at the liquid-gas interface as

the bubbles shrank. However if this is the key to nanobubble stability a 'universal' contamination of all experiments is required, with many different materials and setups, which is questionable.

Brenner and Lohse proposed the "dynamic equilibrium" model, here the gas outflux at the apex of the bubble is perfectly balanced by an influx at the three phase contact line⁵⁴. The model suggests that smaller bubbles should grow whilst larger bubbles should shrink, so at a certain size an equilibrium should be reached.

There are a few implications of this model which are yet to be addressed. Firstly, the outfluxing gas must be returned somehow to the surface. The recirculating gas loop must require an energy input but where this energy would come from is not clear, however this process cannot be run for free.

The model was added to by Seddon *et al.* who noted the gas found within nanobubbles was typically of Knudsen type⁵⁵. A Knudsen gas is one in which molecules rarely collide with one another, but frequently collide with the side of the containing body. The Knudsen number is the ratio of the mean free path to the typical length of the container (the bubble height). Seddon *et al.* propose that due to the asymmetric geometry of the system (one side is the flat surface, the other the curved liquid-gas interface) there is a bulk gas flow within the bubbles that would not be present in a non-Knudsen environment as the gas molecules are deflected towards the apex, figure 2.11. This bulk movement exerts a sheer stress in the liquid which drives a circulating gas-rich liquid stream.

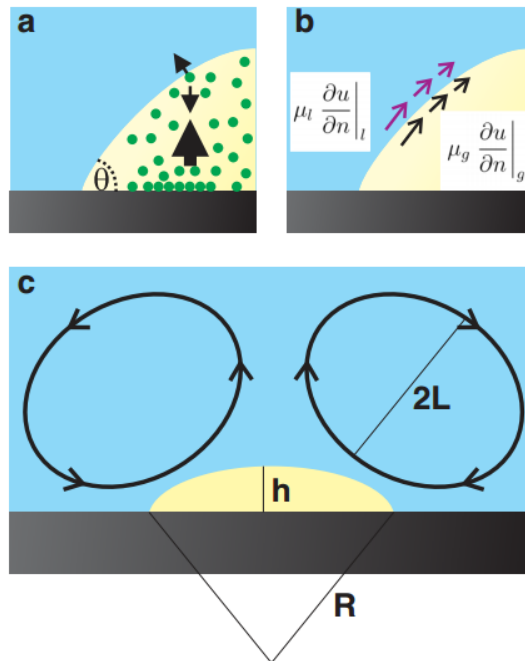


Figure 2.11 Schematic of the model proposed by Seddon *et al.* a) The broken symmetry leads to a bulk flow of gas to the top of the bubble. b) The tangential component of the gas flow drives a liquid flow. c) The gas rich liquid flow recirculates to the three phase contact line. Image from Seddon *et al.* ⁵⁵.

Weijs and Lohse propose that it is the gas transfer from the bulk liquid to the atmosphere that limits the dissolution of nanobubbles, not the transfer from nanobubble to liquid which increases the bubble life time⁵⁶. The dissolution is further slowed by the pinning of the edge of the bubbles, leading to a reduced radius of curvature and therefore a lower internal pressure which drives the dissolution.

Pinning of the contact line has been shown to be of importance to the stabilisation of nanobubbles in a. Liu *et al.* studied contact line pinning of nanobubbles in a computer simulation showing that local heterogeneities to the substrate can significantly increase nanobubble stability{Liu, 2014 #255}.

Nanobubbles are stable to shock wave induced cavitation at pressures of -6 MPa (relative to atmospheric pressure)⁵⁷. From nucleation theory bubbles with a radius of curvature < 10 nm should shrink and > 10 nm should grow to micron sized bubbles. Surfaces with coverages up to 80 bubbles per μm^2 showed no cavitation activity when a shock wave of 6 MPa was induced. In other nanobubble laden surfaces cavitation nuclei only grew exclusively from micron sized cracks. It is

worth noting that as well as withstanding the large tensile stress, the bubbles must also persist through the initial compression of +6 MPa of the shock wave.

2.2.5 The Nanobubble Bridging Capillary Force

When two submerged hydrophobic surfaces are brought within several hundred nanometres of one another an attractive force is felt between the two. This phenomena used to be called the long range hydrophobic attraction, before nanobubbles had been identified as the cause of this force.

The cause of the force originates from the coalescence of nanobubbles between the two surfaces (or a single nanobubbles and a hydrophobic surface) which forms a capillary bridge which acts to pull the two surfaces together⁵⁸, shown in figure 2.12. The nanobubble bridging capillary force has been shown to increase friction between hydrophobized silicon surfaces due to the increased adhesion force in an AFM study⁵⁹.

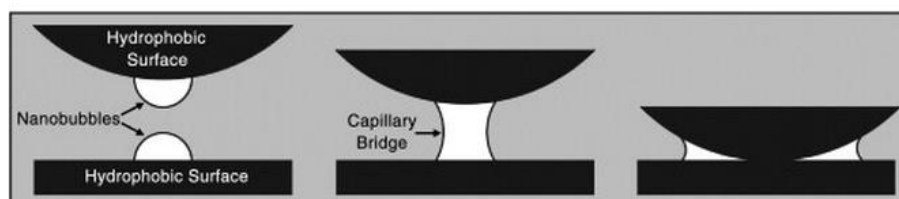


Figure 2.12 Schematic of the nanobubble bridging capillary force between two hydrophobic surfaces from Hampton and Nguyen⁵⁸.

2.2.6 Application

Surface nanobubbles have been cited by many as a way to reduce drag in microfluidic environments^{47, 60, 61, 62, 63}. Meinhart showed that dissolved gas concentration dramatically effects the boundary condition in a microchannel, which allows the fluid to slip on the channel side wall which minimised pressure drop⁶⁴. The effect of nanobubbles on slip and drag reduction is discussed in detail in Section 3.

2.2.7 Summary of Section 2

Nanobubbles are a nano-sized gas state which has an unexpectedly long life time and the contact angle of the bubbles differs considerably from their macroscopic counterparts. They cause the long range force experienced between hydrophobic surfaces.

Nanobubbles can be nucleated on hydrophobic surfaces by immersion in saturated or supersaturated water at $\sim 35^\circ \text{C}$, by heating the surface whilst immersed or by ethanol solvent exchange.

Several theories have been put forward to explain the long lifetime of nanobubbles, however no real consensus has been made. Current popular theories include contamination, dynamic equilibrium, diffusion limited gas transfer and contact line pinning. Slip, Drag and Friction

2.3 Slip, Drag and Friction

This section discusses the phenomena of slip and it leads to a reduction in drag and how the geometry of superhydrophobic surfaces are linked to the slip length. Evidence for link between nanobubbles and slip is reviewed and why they made be useful in reduce drag in small scale fluidic environments, for example in a small scale hydrodynamic bearing.

2.3.1 Introduction

The proper boundary condition to impose on a solid body in hydrodynamics has been subject to much debate since the 19th century⁶⁵. The conclusion was reached that the molecules adjacent to the surface are stationary was appropriate, due to good agreement between (macroscopic) experiment and theory; this is known as the no-slip condition, figure 2.13 a.)

However more recently investigations have shown a slip effect where molecules on the surface are not stationary and move along the surface with the flow. To quantify the slipping movement of the molecules on the surface, the Navier slip length model is used figure 2.13 b) and equation 2.13)⁶⁶. A simple shear driven flow (Couette flow) between two parallel plates is modified to account for the velocity of the liquid at the slip surface, u_o . The slip length, b is defined as the extrapolated length beneath the solid surface that the liquid velocity reaches zero. When u is the velocity of the flow and y is the height within the channel the velocity of the fluid at the slip surface is:

$$u_o = b \frac{du}{dy} \quad (2.13)$$

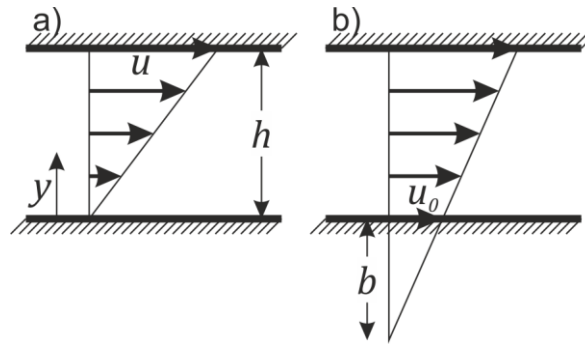


FIGURE 2.13 Schematic of fluid slip at a solid interface. Where u is velocity, y is the height above the surface, u_o is the velocity at the surface and b is the slip length.

2.3.2 Intrinsic Slip on Flat Solid Surfaces without a Gas Layer

The mechanisms which allow slip of fluids against flat solid surfaces without a gas layer present as shown in figure 2.13 b) in some situations but not in others are not well understood. However well controlled experimental studies have found several factors which are important for this phenomenon to arise.

2.3.2.1 Contact Angle

The contact angle of the surface has been shown many times to be linked to slip; where large contact angles (hydrophobic surfaces), indicating a weak interaction between liquid and solid, have shown slip and small contact angles (hydrophilic surfaces) do not.

Baudry *et al.* demonstrated using a surface force apparatus a slip of 40 nm using glycerol against a cobalt surface modified with a hydrophobic surface monolayer (contact angle 101°); the slip was not present without the monolayer⁶⁷. Choi *et al.* monitored flow rate and pressure drop of water through 1 and 2 μm hydrophobic and hydrophilic micro channels. They found a slip length of ~ 30 nm in the hydrophobic channel and no slip for the hydrophilic channel however this could be due to the presence of nanobubbles⁶⁸.

2.3.2.2 Surface Roughness

Understanding the relationship between surface roughness and slip is difficult as it is impossible to control and quantifying surface roughness without effecting the surface wetting. Most investigations have shown that slip is suppressed by surface roughness⁶⁹. However in a thin film drainage experiment Bonaccorso *et al.* showed the slip was shown to increase with surface roughness up to maximum tested roughness of 12.2 nm rms⁷⁰.

2.3.2.3 Shear Rate

Shear rate dependence of the slip length is again debatable. The Navier model of slip does not include a shear rate dependence and many investigations show that slip length remains constant⁶⁹. Some reports indicate that, whilst at relatively low shear rates a constant slip length model is correct, as a critical shear rate is reached the slip increases with shear rate⁷¹.

2.3.2.4 Nanobubbles and Slip

The nucleation of nanobubbles on hydrophobic surfaces and their total absence from hydrophilic surfaces has led to many suggestions that nanobubbles could be the cause of slip in some experiments using water⁶¹. However the link remains tenuous due to difficulty measuring both bubble coverage and slip *in situ*⁷².

Tretheway and Meinhart observed slip in the micron range at hydrophobic walls in a microchannel which was not present for hydrophilic walls⁷³. They proposed that the presence of nanobubbles on the hydrophobic surface caused slip on the liquid/gas interface⁷⁴. Finger and Johannsmann used a quartz crystal microbalance to measure the hydrodynamic drag on gold surfaces covered with electrochemically generated nanobubbles. Where the supporting electrolyte was KNO₃ or NaCl the drag increased whereas where it was NaBr the drag decreased.⁷⁵

There is split opinion on the theoretical effect a coverage of nanobubbles could have on the slip length over a hydrophobic surface and whether it could be significantly greater than the intrinsic slip discussed above. The system has been modelled in many different ways leading to some to suggest that nanobubbles enhance slip⁷⁶ and others who say the effect is negligible⁷⁷. Some studies have shown the importance of the shape of the nanobubbles on the effective slip length, where the more the bubbles protrude into the flow the lesser the slip effect⁷⁸. Estimates of slip length generally range between 10nm and 100 nm. Many experiments investigating the intrinsic slip effect

on hydrophobic surfaces were done prior to the detection of nanobubbles around 15 years ago. This means that the presence of nanobubbles was not controlled for so may have inadvertently been measuring slip over nanobubbles which could confuse the situation further.

2.3.3 Flow Over a Lubricating Gas Layer

Introduction of a lubricating gas layer on a surface such a coverage of nanobubbles or with a superhydrophobic surface leads to what is termed an apparent or effective slip where shear stress is exerted on the lower viscosity gas layer, figure 2.14. This is distinct from a ‘true’ slip (figure 2.13 b) where liquid molecules move along a solid surface as discussed above and can be several orders of magnitude larger. The slip is proportional to the difference in the viscosity between the lubricating layer and the surrounding liquid (equation 2.14); in the case of water and air there is roughly a factor of 50 difference in viscosity between the two. Equation 2.14 gives the slip length, b , of a fluid with a higher viscosity μ_h over a fluid with a lower viscosity of μ_l and height δ .

$$b = \delta \left(\frac{\mu_h}{\mu_l} - 1 \right) \quad (2.14)$$

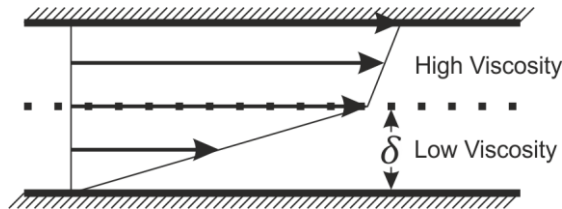


FIGURE 2.14 Couette flow with high and low viscosity fluids where δ is the height of the low viscosity layer.

2.3.4 Drag Reduction

The drag reduction (DR) in a Couette flow from the change in the shear forces, τ , due to the presence of slip is:

$$DR = \frac{\tau_{\text{no-slip}} - \tau_{\text{slip}}}{\tau_{\text{no-slip}}} \quad (2.15)$$

Which is related to the slip length, b , and channel height, h , (figure 2.13 b) dimensions by¹⁸:

$$DR = \frac{b}{h + b} \quad (2.16)$$

Equation 2.16 is plotted in figure 2.15 showing the drag reduction as a function of channel height where $b = 0.1, 1, 10$, and $100 \mu\text{m}$. This graph demonstrates the importance of matching the slip length to the size of the system. The slip length found on flat hydrophobic surfaces between 100 nm and $1 \mu\text{m}$ can be useful in lubricating the side walls in micro and nano fluidic environments. However much larger slip lengths must be generated to reduce the drag of larger scaled situations, for example the boundary layer around a ship is typically the order of millimetres, so slip lengths of at least hundreds of microns are required for a significant effect.

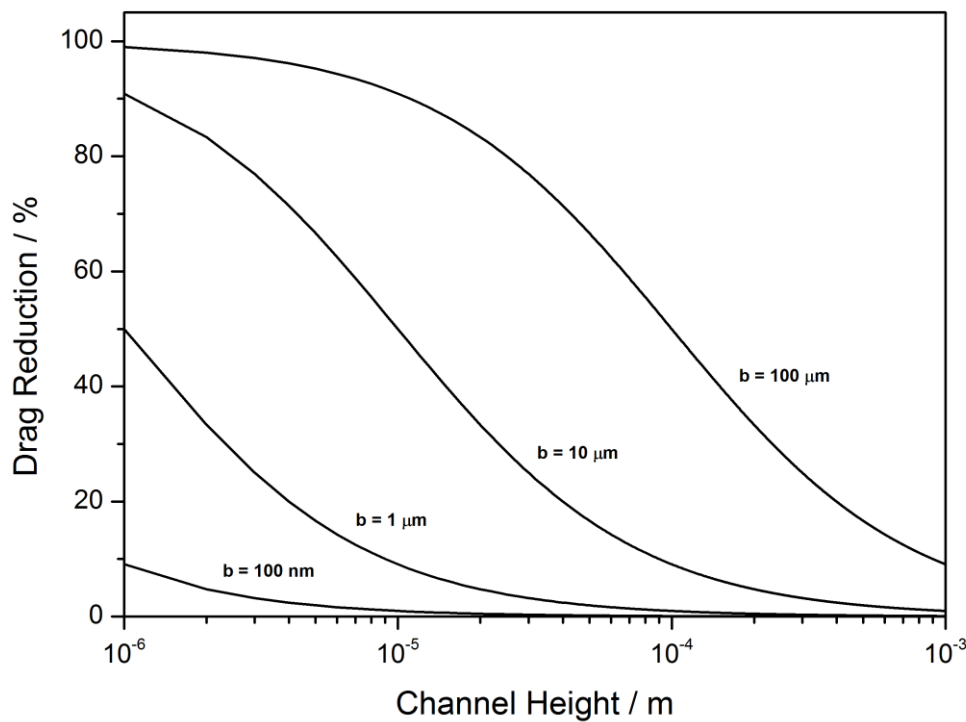


Figure 2.15 Drag reduction in a Couette flow at different slip lengths as a function of channel height.

2.3.5 Effect of Superhydrophobic Surface Geometry on Slip Length

Superhydrophobic surfaces do not have a continuous air film, as surface structures are required to suspend the interface. Ybert *et al.* investigated the effect of the superhydrophobic surface structure

on slip length for post, grating and hole geometries as the solid fraction, ϕ_s , approached 0 in a laminar flow⁷⁹. They assumed that the liquid-gas interface was shear free and flat and the areas touching solid held the no-slip condition. The term b_{eff} is the effective slip length which averaged over the surface and L is the pitch between features.

They estimate the effective slip length for gratings and holes to be:

$$b_{\text{eff}} \sim -L \log(\phi_s) \quad (2.17)$$

And for posts to be:

$$b_{\text{eff}} \sim \frac{L}{\sqrt{\phi_s}} \quad (2.18)$$

2.3.6 Experimental Evidence

Lee and Kim investigated the effect of feature spacing and gas fraction on the slip length in post and grating geometries¹⁶. The surfaces were made using photolithography and the slip length was measured using cone and plate rheometry. The gas fraction was changed independently of the pitch and *vice versa*. Their post and grating surfaces with constant pitch are shown figure 2.16.

The slip length was calculated from the torque measurement in a cone and plate rheometry setup, where the volume of water was carefully monitored by imaging the meniscus between the cone and plate with a digital camera. The flow condition was estimated to be laminar. The slip length was plotted as a function of gas fraction and also pitch (figure 2.16 d) and e)). The experimental results agreed very well with theoretical predictions of slip for both the post and grating structures in equations 2.17 and 2.18^{79, 80}. Others have done similar experiments which also agree very well with the predicted slip length for both posts and gratings^{27, 81}. Slip lengths on the order of hundred of micrometers have been reported for superhydrophobic surfaces{Choi, 2006 #48}{Daniello, 2009 #246} with a maximum of 400 μm by Lee and Kim{Lee, 2009 #142}.

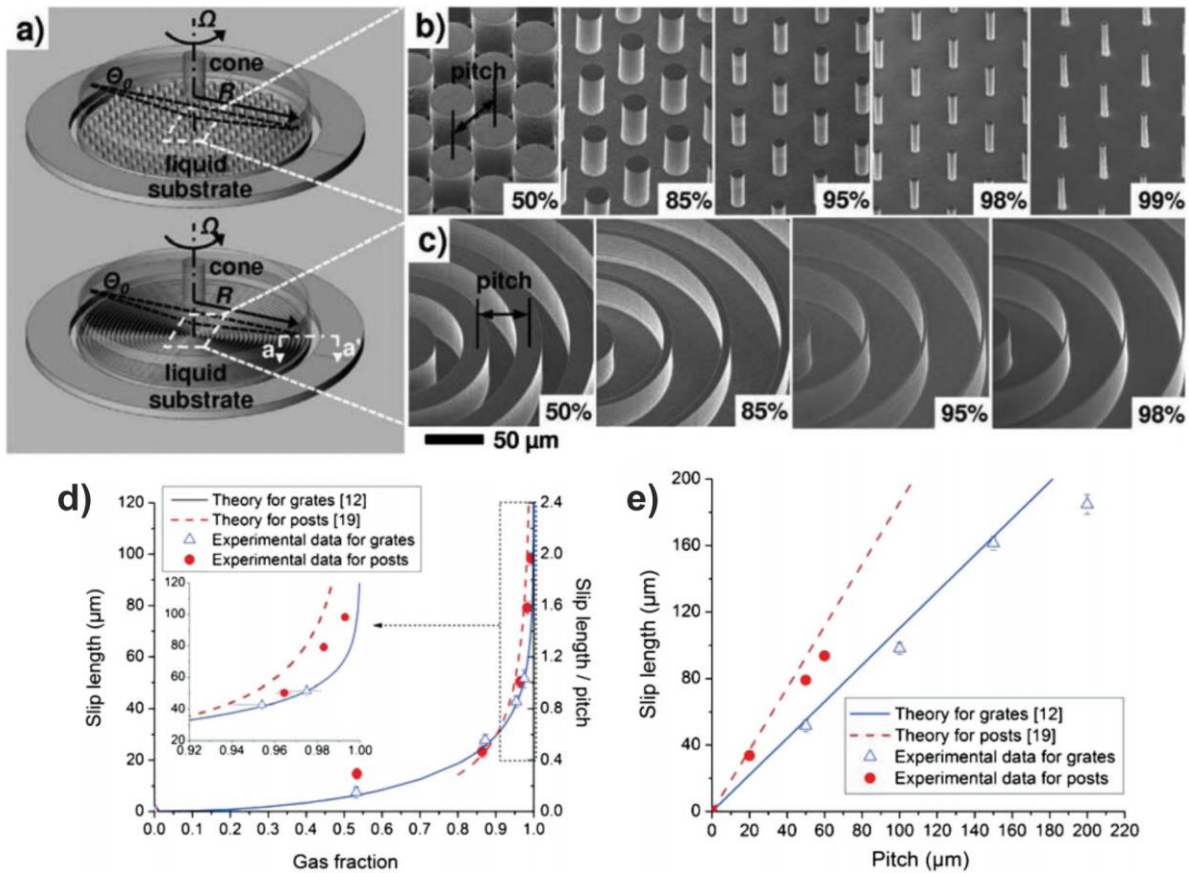


Figure 2.16 From Lee *et al.*¹⁶ a) Cone and Plate rheometry experimental set-up. b) Post structures with increasing gas fraction but constant pitch c) The same for the grating structure. d) Slip length as a function of gas fraction and e) slip length as a function of pitch for posts and gratings experimental and theoretical results. Tests were carried out at room temperature using water as the liquid.

Recently, Park *et al.* showed a massive 70 % drag reduction in a turbulent flow with Reynolds number $\sim 2 \times 10^5$, using a custom built shear sensing set-up in a microchannel⁸². The Grating structures were used oriented parallel to the flow direction with 95% gas fraction and 50 μm pitch.

To optimise a superhydrophobic surface for maximum slip length (and therefore drag reduction) the features for either post or grating structures must have the largest gas fraction and pitch possible. However; increasing both of these parameters acts to reduce the required force to transition the wetting state from the Cassie to the Wenzel state as shown in Section 1 equation 2.3.

Aljallis *et al.* used a 2 ft by 4 ft aluminium plate in a towing tank, measuring the drag coefficient with two different superhydrophobic surface coatings²⁸. The surface structures had random morphologies, so gas fraction and pitch varied considerably throughout. One of the tested surfaces

showed a drag reduction of up to 30 % at lower Reynolds numbers, however the gas was seen to start leaving the surface at higher speeds (Figure 2.17). When the gas is removed from a superhydrophobic surface, the drag increases, as by their nature a high roughness is present which leads to more drag than on a smooth surface. If the wetting state of the surface is unknown interpretation of the drag data is severely limited.

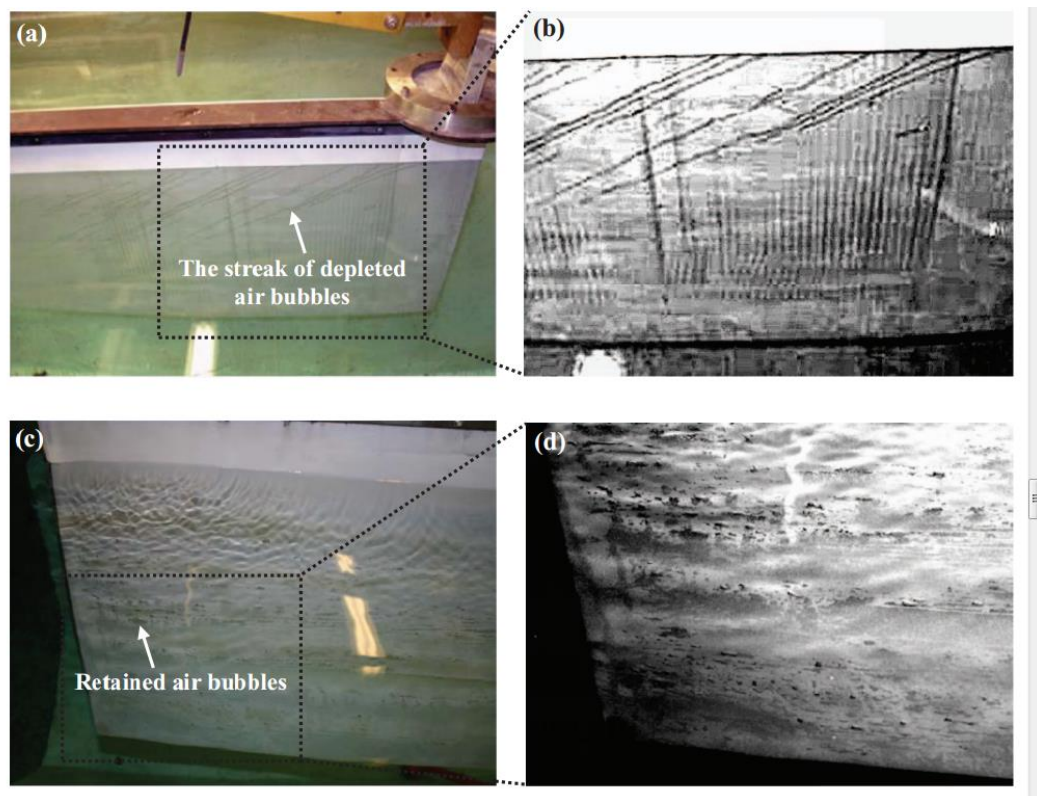


Figure 2.17 Photograph of 2 x 4 ft plate in towing tank after towing at ~ 1 knot (photos a and b) and ~ 18 knots (c and d). At 1 knot some areas have lost the gas, at 18 knots, most of the gas has been removed (from Aljallis *et al.*²⁸)

2.3.7 Slip in tribology

The low profile of nanobubbles and their long lifetime could make them suitable for environments such as in a hydrodynamic bearing. The small spacing between the load bearing surfaces in

hydrodynamic conditions means that only a modest slip length is required to generate a significant drag reduction as shown previously in figure 2.15. They could be better suited to this situation than superhydrophobic surfaces where the gas film is short lived and a prominent surface structure is required which would be ill suited to the shear forces in a bearing. Even if the nanobubbles were removed in some instances one of the nucleation methods could be used such as electrochemically generated hydrogen or heating of the lubricant to generate a full coverage again.

Bearings facilitate low friction motion between components. Generally a lubricant is introduced between the two surfaces in relative motion to decrease wear and friction. Distinct lubrication regimes are found as the lubricant film increases in height, these regimes will be discussed in terms of the Lambda ratio – the ratio of the minimum lubricant film height, to the route mean squared roughness of the two faces (figure 2.18). Boundary lubrication occurs when the solid surfaces are in contact with one another and the load is supported by contact between surface asperities. Mixed lubrication occurs when a thin lubricant film forms which carries some load however asperity contact between the surfaces still persists. In hydrodynamic lubrication the solid surfaces are fully separated by a fluid film analogous to the Couette flow discussed earlier.

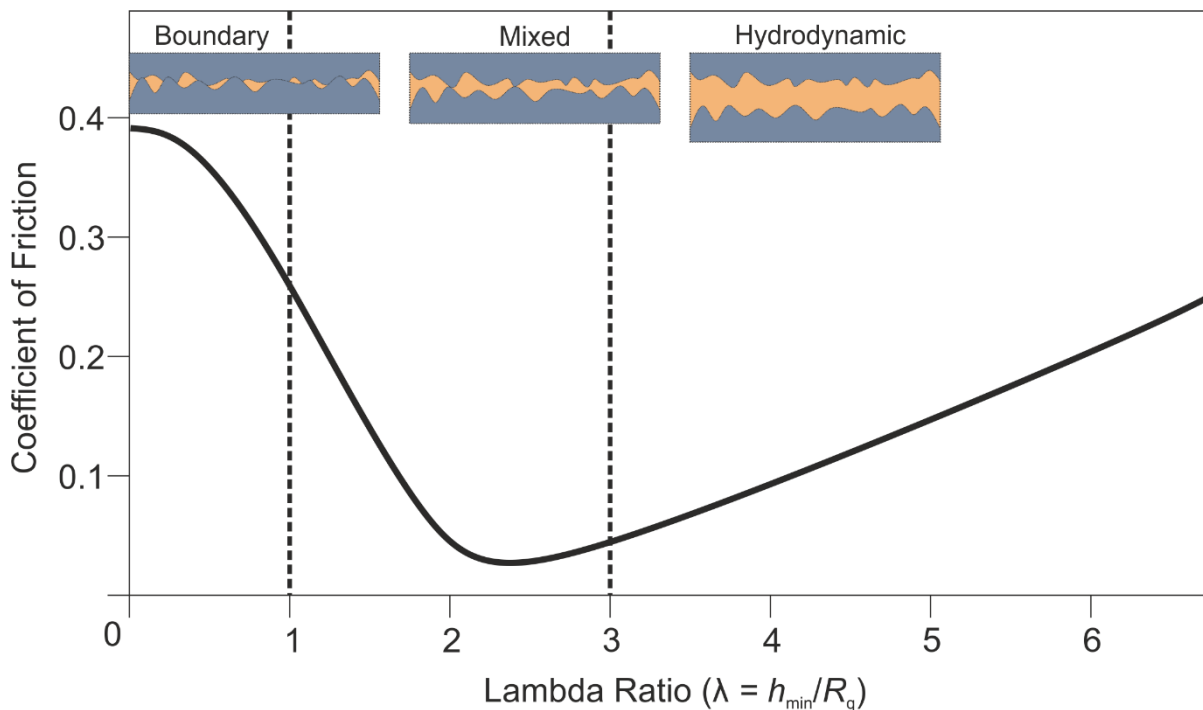


Figure 2.18 Graph showing the general relationship between coefficient of friction and the lambda ratio where h_{\min} is the minimum film lubricant film thickness and R_q is the route mean squared roughness averaged between the two faces.

The effect of slip of the lubricant against the wall in a hydrodynamic bearing was considered by Spikes who developed the idea of the ‘half-wetted’ bearing⁸³. The concept involves a ‘non-wetting’ surface which allows fluid to slip and another ‘wetted’ surface which has a no-slip boundary condition which is hydrophilic to aid entrainment of the lubricant. This work incorporated slip into the Reynolds equation which highlighted the potential for very low friction under hydrodynamic conditions where one surface permitted slip. The predicted reduction in friction was most pronounced in situations of low convergence and low load – as some load support is sacrificed by the addition on the slip surface. Spikes showed this type of lubrication would be well suited to micron sized components where load support is much in excess of what is required and surfaces generally have very low surface roughness which is necessary for the slip to occur⁸⁴. Informed by Spikes’ work experimental investigations into friction reduction through a slip mechanism in the hydrodynamic regime has mostly concentrated on small scale bearings found in micro electromechanical systems (MEMS)^{85, 86}.

The concept of the half wetted bearing has been tested experimentally by Choo *et al.* using mica, modified with a self assembled monolayer of hydrolyzed octadecyltriethoxysilane (OTE) to make it hydrophobic as the slip surface of the bearing^{85, 87}. The experimental setup was a custom made rotating round edged cylinder on flat configuration where an uncoated hydrophilic glass cylinder was used as the rotor.

The authors’ first choice of lubricant was water noting the evidence of slip of water against a hydrophobic surface. However, the predicted hydrodynamic film thickness was deemed to be too low at the desired operational speed and load. To give unambiguous fluid film lubrication the viscosity was increased by using a 72% aqueous glycerol solution. The contact angle on the unmodified mica surface using the 72% aqueous glycerol solution was 5° and on the OTE modified mica it was 86°.

The loads used in the experiments were 0.05 N, 0.1 N and 0.2 N and the sliding speed was in the range of 1 and 2 m s⁻¹. The maximum and minimum pressures in the contact were 108 MPa (0.2 N, 1 m s⁻¹) and 68 MPa (0.05 N, 2 m s⁻¹) respectively. The conditions are comparable to those found in MEMS gas turbines⁸⁸ and MEMS thrust bearings⁸⁹.

Figure 2.19 a) shows the friction coefficient plotted against sliding speed for un-modified mica (solid black symbols) and OTE modified mica (black outlines) at the three normal loads. As expected friction increases with higher sliding speed and lower load due to a thicker lubricant film. There is a clear reduction in friction for the OTE modified mica surface when compared to the corresponding un-modified case. The effect is more pronounced at lower load with an average reduction in friction of 23% at 0.05 N, 22% at 0.1 N and 18% at 0.2 N.

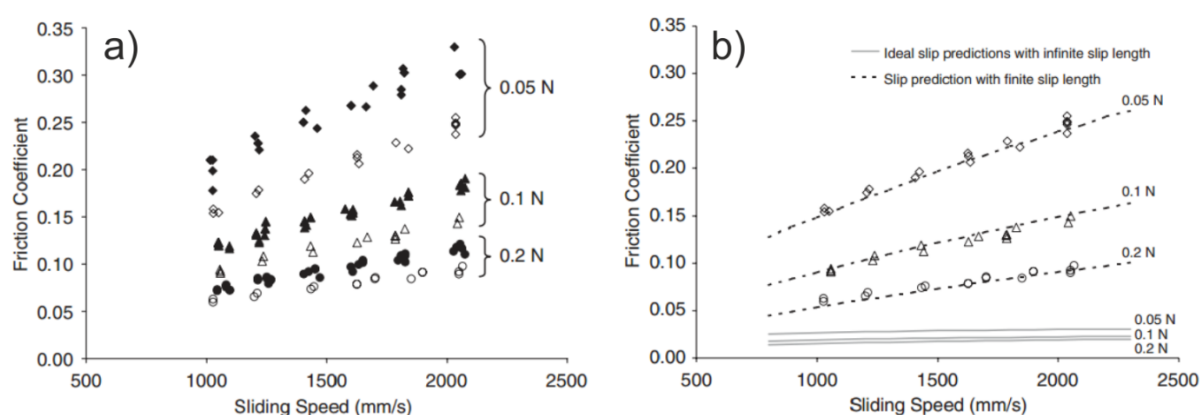


Figure 2.19 Friction coefficients plotted against sliding speed at 0.05 N, 0.1 N and 0.2 N a) Black solid points are the unmodified mica surface, black outlines are the OTE modified mica surfaces. b) OTE modified surfaces with slip prediction with 20 μm slip length (dotted lines) and infinite slip (solid lines). From Choo *et al.*⁸⁷.

A slip length of 20 μm fitted the data best the predicted trend for infinite slip is also plotted (Figure 2.19) b). It is unknown if nanobubbles are present on the surface in the 72% aqueous glycerol solution. Slip of 200 nm has been seen on hydrophobic surfaces when glycerol is used as the fluid⁹⁰, however shear rates were much slower, 30 s^{-1} as opposed to a maximum of $235\,000\text{ s}^{-1}$ in the study by Choo *et al.*⁸⁷.

A blend of Multiply-alkylated cyclopentane (MAC) and hexadecane has shown slip like behaviour in a MEMS tribometer at low load (0.05 N) and high speed (up to 3.14 m s^{-1}).⁸⁶ A tentative explanation proposed that MAC formed a thin film on the silicon surfaces of the bearing which allowed the lubricant to slip at the interface.

2.3.8 Summary of Section 3

On solid surfaces the origin of the slip is not well understood and is typically less than 1 μm . To maximise slip surfaces should generally be smooth and hydrophobic and is usually quantified as a slip length.

Superhydrophobic surfaces trap a lubricating layer of gas between water and the solid surface. Slip lengths of $\sim 200 \mu\text{m}$ have been measured on a superhydrophobic post structure in laminar flow⁹¹. Drag reduction has also been shown to be possible in turbulent conditions. Slip lengths of this size could reduce skin friction drag around ships.

Larger spacing between surface structures and higher gas fraction lead to improved slip lengths, however this is ultimately limited by the wetting transition which is also proportional to spacing and gas fraction. Dissolution of the lubricating gas into the surrounding water is also a problem, therefore an active system to retain the gas is required.

Slip of the lubricant can reduce friction in hydrodynamic lubrication conditions in small sized bearings when a hydrophobic surface is used for one of the contacting surfaces but not when a hydrophilic surface is used. The origin of the slip in tribological contacts is still relatively unknown although some work has suggested a weak attractive force between lubricant and surface can aid slip.

It is important to match the slip length of the surface to the size of the fluidic system. The slip length generated using superhydrophobic surfaces in the range of 100 μm means systems like pipes and ships, whereas the slip over a nanobubble laden surface of 100 nm means smaller systems such as microfluidics.

2.4 General Conclusion of Literature Review

This chapter has covered the topics of wetting, superhydrophobicity, nanobubbles, slip and drag reduction. To conclude this chapter the key points of the literature review are summarised and linked to the aims of this Thesis.

Superhydrophobic surfaces trap a layer of gas between themselves and water using a rough hydrophobic surface texture. The increased observed contact angle of water drops on superhydrophobic surfaces is predicted by the Cassie-Baxter equation when the gas layer is intact. The gas can be displaced by the pressure of the water overcoming the capillary pressure generated by the presence of the hydrophobic surface structures or by dissolution of the gas into the surrounding water. Reversing this transition is energetically unfavourable however Kim et al. have developed a surface which is capable of doing this as long as the nanostructured base of the surface does not become wetted¹¹. Superhydrophobic surfaces can generate an apparent slip over the gas layer due to difference in viscosity. This slip can be maximised by increasing the gas fraction and increasing the distance between surface features, however this makes the surface more susceptible to becoming wetted. To have a significant impact on drag the slip length must be on the same scale as the channel height or boundary layer. Superhydrophobic surfaces have demonstrated slip lengths up to 200 μm in laminar flow conditions and drag reduction of 70% in turbulent flow conditions, and have the potential to reduce drag in large scale fluidic systems such as pipes and ships. However the dissolution of the gas film into the surrounding water means that these low drag properties are short lived.

The work in the first part of this Thesis starts by considering the fundamental aspects of the wetting in Chapter 4. The work then moves to develop surfaces capable of topping up the gas film as it dissolves in Chapter 5 and to reintroduce gas to the surface once it has become completely wetted in Chapter 6. This could allow superhydrophobic surfaces to be used for long periods of time without fear of them becoming wetted and losing their low drag properties. Methods by which to measure the amount of gas present in the surface are also investigated, this has been a major challenge in larger scale testing.

Nanobubbles are gaseous domains generally $< 100\text{ nm}$ in height and $< 1\text{ }\mu\text{m}$ wide found on hydrophobic surfaces when submerged in water. They have several unexplained properties such as their long lifetime and high contact angle. They are generally nucleated by the solvent exchange method where an alcohol is displaced by water; the mixing process is exothermic leading to super saturation of the dissolved gases. The question as to whether water will slip over a coverage of nanobubbles has not been answered, several theoretical papers have been written on the subject with some saying an increased slip should be observed and others that the nanobubbles should have no discernible effect. Experimental investigations into the phenomena are lacking. If covering a surface with nanobubbles does lead to slip they could be used to reduce drag in small scale fluidic

devices. The fact that they are resilient to dissolution, are easily nucleated and do not protrude into the flow could make them particularly effective at drag reduction where superhydrophobic surfaces are not appropriate. The second part of this Thesis aims to control nanobubble properties and surface coverage using structured surfaces in Chapter 7. The drag and frictional properties of the surfaces will be tested in Chapter 8, using a tribometer which replicates conditions found in microelectromechanical devices where slip could lead to significant drag reduction.

2.5 References

1. Young, T. An essay on the cohesion of fluids. *Philos. Trans. R. Soc. London* **1805**, 95, 65-87.
2. Laplace, P. S. *Traité de mécanique céleste*; l'Imprimerie de Crapelet 1805; Vol. 4.
3. Wenzel, R. N. Resistance of solid surfaces to wetting by water. *Industrial & Engineering Chemistry* **1936**, 28 (8), 988-994.
4. Cassie, A.; Baxter, S. Wettability of porous surfaces. *Trans. Faraday Society* **1944**, 40, 546-551.
5. Barthlott, W.; Neinhuis, C. Purity of the sacred lotus, or escape from contamination in biological surfaces. *Planta* **1997**, 202 (1), 1-8.
6. Extrand, C. Criteria for ultralyophobic surfaces. *Langmuir* **2004**, 20 (12), 5013-5018.
7. Lv, P.; Xue, Y.; Shi, Y.; Lin, H.; Duan, H. Metastable states and wetting transition of submerged superhydrophobic structures. *Phys. Rev. Lett.* **2014**, 112 (19), 196101.
8. Xu, M.; Sun, G.; Kim, C.-J. Infinite Lifetime of Underwater Superhydrophobic States. *Phys. Rev. Lett.* **2014**, 113 (13), 136103.
9. Boreyko, J. B.; Chen, C.-H. Restoring superhydrophobicity of lotus leaves with vibration-induced dewetting. *Phys. Rev. Lett.* **2009**, 103 (17), 174502.
10. Krupenkin, T. N.; Taylor, J. A.; Wang, E. N.; Kolodner, P.; Hodes, M.; Salamon, T. R. Reversible wetting-dewetting transitions on electrically tunable superhydrophobic nanostructured surfaces. *Langmuir* **2007**, 23 (18), 9128-9133.
11. Lee, C.; Kim, C.-J. Underwater restoration and retention of gases on superhydrophobic surfaces for drag reduction. *Phys. Rev. Lett.* **2011**, 106 (1), 014502.
12. Lee, C.; Kim, C.-J. Wetting and Active Dewetting Processes of Hierarchically Constructed Superhydrophobic Surfaces Fully Immersed in Water. *Journal of Microelectromechanical Systems* **2012**, 21 (3), 712-720.
13. Erbil, H. Y.; Demirel, A. L.; Avci, Y.; Mert, O. Transformation of a simple plastic into a superhydrophobic surface. *Science* **2003**, 299 (5611), 1377-1380.
14. Bico, J.; Marzolin, C.; Quéré, D. Pearl drops. *EPL* **1999**, 47 (2), 220.
15. Qu, M.; Zhang, B.; Song, S.; Chen, L.; Zhang, J.; Cao, X. Fabrication of Superhydrophobic Surfaces on Engineering Materials by a Solution - Immersion Process. *Adv. Funct. Mater.* **2007**, 17 (4), 593-596.
16. Lee, C.; Choi, C.-H.; Kim, C.-J. C. Structured surfaces for a giant liquid slip. *Phys. Rev. Lett.* **2008**, 101 (6), 064501.

17. Zhang, J.; Li, J.; Han, Y. Superhydrophobic PTFE surfaces by extension. *Macromol. Rapid Commun.* **2004**, 25 (11), 1105-1108.
18. Choi, C.-H.; Kim, C.-J. Large slip of aqueous liquid flow over a nanoengineered superhydrophobic surface. *Phys. Rev. Lett.* **2006**, 96 (6), 066001.
19. Lau, K. K.; Bico, J.; Teo, K. B.; Chhowalla, M.; Amaratunga, G. A.; Milne, W. I.; McKinley, G. H.; Gleason, K. K. Superhydrophobic carbon nanotube forests. *Nano Lett.* **2003**, 3 (12), 1701-1705.
20. Bhushan, B.; Chae Jung, Y. Wetting study of patterned surfaces for superhydrophobicity. *Ultramicroscopy* **2007**, 107 (10), 1033-1041.
21. Cao, L.; Hu, H.-H.; Gao, D. Design and fabrication of micro-textures for inducing a superhydrophobic behavior on hydrophilic materials. *Langmuir* **2007**, 23 (8), 4310-4314.
22. Bhushan, B.; Her, E. K. Fabrication of superhydrophobic surfaces with high and low adhesion inspired from rose petal. *Langmuir* **2010**, 26 (11), 8207-8217.
23. Cao, L.; Jones, A. K.; Sikka, V. K.; Wu, J.; Gao, D. Anti-icing superhydrophobic coatings. *Langmuir* **2009**, 25 (21), 12444-12448.
24. Zhang, F.; Zhao, L.; Chen, H.; Xu, S.; Evans, D. G.; Duan, X. Corrosion resistance of superhydrophobic layered double hydroxide films on aluminum. *Angew. Chem. Int. Ed.* **2008**, 47 (13), 2466-2469.
25. Shateri Khalil-Abad, M.; Yazdanshenas, M. E. Superhydrophobic antibacterial cotton textiles. *J. Colloid Interface Sci.* **2010**, 351 (1), 293-298.
26. Vincent, J. Superhydrophobic spray NeverWet enters US market in a \$20 can. *The Independant*, 21/06/2013, 2013.
27. Rothstein, J. P. Slip on superhydrophobic surfaces. *Annu. Rev. Fluid. Mech.* **2010**, 42, 89-109.
28. Aljallis, E.; Sarshar, M. A.; Datla, R.; Sikka, V.; Jones, A.; Choi, C.-H. Experimental study of skin friction drag reduction on superhydrophobic flat plates in high Reynolds number boundary layer flow. *Phys. Fluids* **2013**, 25, 025103.
29. Borkent, B. M.; de Beer, S.; Mugele, F.; Lohse, D. On the shape of surface nanobubbles. *Langmuir* **2009**, 26 (1), 260-268.
30. Parker, J. L.; Claesson, P. M.; Attard, P. Bubbles, cavities, and the long-ranged attraction between hydrophobic surfaces. *The Journal of Physical Chemistry* **1994**, 98 (34), 8468-8480.
31. Ishida, N.; Inoue, T.; Miyahara, M.; Higashitani, K. Nano bubbles on a hydrophobic surface in water observed by tapping-mode atomic force microscopy. *Langmuir* **2000**, 16 (16), 6377-6380.
32. Lou, S.-T.; Ouyang, Z.-Q.; Zhang, Y.; Li, X.-J.; Hu, J.; Li, M.-Q.; Yang, F.-J. Nanobubbles on solid surface imaged by atomic force microscopy. *Journal of Vacuum Science & Technology B: Microelectronics and Nanometer Structures* **2000**, 18 (5), 2573-2575.
33. Zhang, X. H.; Khan, A.; Ducker, W. A. A nanoscale gas state. *Phys. Rev. Lett.* **2007**, 98 (13), 136101.
34. Epstein, P.; Plesset, M. On the Stability of Gas Bubbles in Liquid - Gas Solutions. *The Journal of Chemical Physics* **1950**, 18, 1505.
35. Ljunggren, S.; Eriksson, J. C. The lifetime of a colloid-sized gas bubble in water and the cause of the hydrophobic attraction. *Colloids and Surfaces A: Physicochemical and Engineering Aspects* **1997**, 129, 151-155.
36. Zhang, X. H.; Quinn, A.; Ducker, W. A. Nanobubbles at the interface between water and a hydrophobic solid. *Langmuir* **2008**, 24 (9), 4756-4764.
37. Lou, S. T.; Ouyang, Z. Q.; Zhang, Y.; Li, X. J.; Hu, J.; Li, M. Q.; Yang, F. J. Nanobubbles on solid surface imaged by atomic force microscopy. *Journal of Vacuum Science & Technology B* **2000**, 18 (5), 2573-2575.
38. van Limbeek, M. A.; Seddon, J. R. Surface nanobubbles as a function of gas type. *Langmuir* **2011**, 27 (14), 8694-8699.
39. Zhang, X. H.; Li, G.; Maeda, N.; Hu, J. Removal of induced nanobubbles from water/graphite interfaces by partial degassing. *Langmuir* **2006**, 22 (22), 9238-9243.

40. Seddon, J. R.; Kooij, E. S.; Poelsema, B.; Zandvliet, H. J.; Lohse, D. Surface bubble nucleation stability. *Phys. Rev. Lett.* **2011**, *106* (5), 056101.
41. Yang, S.; Dammer, S. M.; Bremond, N.; Zandvliet, H. J.; Kooij, E. S.; Lohse, D. Characterization of nanobubbles on hydrophobic surfaces in water. *Langmuir* **2007**, *23* (13), 7072-7077.
42. Xue-Hua, Z.; Gang, L.; Zhi-Hua, W.; Xiao-Dong, Z.; Jun, H. Effect of temperature on the morphology of nanobubbles at mica/water interface. *Chinese Physics* **2005**, *14* (9), 1774.
43. Zhang, X. H.; Maeda, N.; Craig, V. S. Physical properties of nanobubbles on hydrophobic surfaces in water and aqueous solutions. *Langmuir* **2006**, *22* (11), 5025-5035.
44. Zhang, L.; Zhang, Y.; Zhang, X.; Li, Z.; Shen, G.; Ye, M.; Fan, C.; Fang, H.; Hu, J. Electrochemically controlled formation and growth of hydrogen nanobubbles. *Langmuir* **2006**, *22* (19), 8109-8113.
45. Yang, S.; Tsai, P.; Kooij, E. S.; Prosperetti, A.; Zandvliet, H. J.; Lohse, D. Electrolytically generated nanobubbles on highly orientated pyrolytic graphite surfaces. *Langmuir* **2009**, *25* (3), 1466-1474.
46. Tyrrell, J. W. G.; Attard, P. Images of nanobubbles on hydrophobic surfaces and their interactions. *Phys. Rev. Lett.* **2001**, *87* (17).
47. Agrawal, A.; Park, J.; Ryu, D. Y.; Hammond, P. T.; Russell, T. P.; McKinley, G. H. Controlling the location and spatial extent of nanobubbles using hydrophobically nanopatterned surfaces. *Nano Lett.* **2005**, *5* (9), 1751-1756.
48. Holmberg, M.; Kühle, A.; Garnæs, J.; Mørch, K. A.; Boisen, A. Nanobubble trouble on gold surfaces. *Langmuir* **2003**, *19* (25), 10510-10513.
49. Switkes, M.; Ruberti, J. Rapid cryofixation/freeze fracture for the study of nanobubbles at solid-liquid interfaces. *Appl. Phys. Lett.* **2004**, *84* (23), 4759-4761.
50. Seo, H.; Yoo, M.; Jeon, S. Influence of nanobubbles on the adsorption of nanoparticles. *Langmuir* **2007**, *23* (4), 1623-1625.
51. Zhang, X. H. Quartz crystal microbalance study of the interfacial nanobubbles. *PCCP* **2008**, *10* (45), 6842-6848.
52. Ducker, W. A. Contact angle and stability of interfacial nanobubbles. *Langmuir* **2009**, *25* (16), 8907-8910.
53. Attard, P. Nanobubbles and the hydrophobic attraction. *Adv. Colloid Interface Sci.* **2003**, *104* (1), 75-91.
54. Brenner, M. P.; Lohse, D. Dynamic equilibrium mechanism for surface nanobubble stabilization. *Phys. Rev. Lett.* **2008**, *101* (21), 214505.
55. Seddon, J. R.; Zandvliet, H. J.; Lohse, D. Knudsen gas provides nanobubble stability. *Phys. Rev. Lett.* **2011**, *107* (11), 116101.
56. Weijs, J. H.; Lohse, D. Why surface nanobubbles live for hours. *Phys. Rev. Lett.* **2013**, *110* (5), 054501.
57. Borkent, B. M.; Dammer, S. M.; Schönherr, H.; Vancso, G. J.; Lohse, D. Superstability of surface nanobubbles. *Phys. Rev. Lett.* **2007**, *98* (20), 204502.
58. Hampton, M.; Nguyen, A. Nanobubbles and the nanobubble bridging capillary force. *Adv. Colloid Interface Sci.* **2010**, *154* (1), 30-55.
59. Hampton, M. A.; Donose, B. C.; Taran, E.; Nguyen, A. V. Effect of nanobubbles on friction forces between hydrophobic surfaces in water. *J. Colloid Interface Sci.* **2009**, *329* (1), 202-207.
60. Craig, V. S. J. Very small bubbles at surfaces—the nanobubble puzzle. *Soft Matter* **2011**, *7* (1), 40-48.
61. de Gennes, P.-G. On fluid/wall slippage. *Langmuir* **2002**, *18* (9), 3413-3414.

62. Zhu, Y.; Granick, S. Rate-dependent slip of Newtonian liquid at smooth surfaces. *Phys. Rev. Lett.* **2001**, *87* (9), 096105.
63. Wang, Y.; Bhushan, B. Boundary slip and nanobubble study in micro/nanofluidics using atomic force microscopy. *Soft Matter* **2010**, *6* (1), 29-66.
64. Tretheway, D.; Stone, S.; Meinhart, C. Effects of Absolute Pressure and Dissolved Gases on Apparent Fluid Slip in Hydrophobic Microchannels. In *APS Division of Fluid Dynamics Meeting Abstracts*, 2004; Vol. 1, pp 561-564.
65. Goldstein, S. Fluid mechanics in the first half of this century. *Annu. Rev. Fluid. Mech.* **1969**, *1* (1), 1-29.
66. Day, M. A. The no-slip condition of fluid dynamics. *Erkenntnis* **1990**, *33* (3), 285-296.
67. Baudry, J.; Charlaix, E.; Tonck, A.; Mazuyer, D. Experimental evidence for a large slip effect at a nonwetting fluid-solid interface. *Langmuir* **2001**, *17* (17), 5232-5236.
68. Choi, C.-H.; Westin, K. J. A.; Breuer, K. S. Apparent slip flows in hydrophilic and hydrophobic microchannels. *Phys. Fluids* **2003**, *15*, 2897.
69. Pit, R.; Hervet, H.; Leger, L. Direct experimental evidence of slip in hexadecane: solid interfaces. *Phys. Rev. Lett.* **2000**, *85* (5), 980.
70. Bonaccorso, E.; Butt, H.-J.; Craig, V. S. Surface roughness and hydrodynamic boundary slip of a Newtonian fluid in a completely wetting system. *Phys. Rev. Lett.* **2003**, *90* (14), 144501.
71. Thompson, P. A.; Troian, S. M. A general boundary condition for liquid flow at solid surfaces. *Nature* **1997**, *389* (6649), 360-362.
72. Maali, A.; Bhushan, B. Nanobubbles and their role in slip and drag. *J. Phys.: Condens. Matter* **2013**, *25* (18), 1-12.
73. Tretheway, D. C.; Meinhart, C. D. Apparent fluid slip at hydrophobic microchannel walls. *Phys. Fluids* **2002**, *14* (3), L9-L12.
74. Tretheway, D. C.; Meinhart, C. D. A generating mechanism for apparent fluid slip in hydrophobic microchannels. *Phys. Fluids* **2004**, *16*, 1509.
75. Finger, A.; Johannsmann, D. Hemispherical nanobubbles reduce interfacial slippage in simple liquids. *PCCP* **2011**, *13* (40), 18015-18022.
76. Dammer, S. M.; Lohse, D. Gas enrichment at liquid-wall interfaces. *Phys. Rev. Lett.* **2006**, *96* (20), 206101.
77. Hendy, S.; Lund, N. Effective slip lengths for flows over surfaces with nanobubbles: The effects of finite slip. *J. Phys.: Condens. Matter* **2009**, *21* (14), 144202.
78. Steinberger, A.; Cottin-Bizonne, C.; Kleimann, P.; Charlaix, E. High friction on a bubble mattress. *Nature Materials* **2007**, *6* (9), 665-668.
79. Ybert, C.; Barentin, C.; Cottin-Bizonne, C.; Joseph, P.; Bocquet, L. Achieving large slip with superhydrophobic surfaces: Scaling laws for generic geometries. *Phys. Fluids* **2007**, *19*, 123601.
80. Lauga, E.; Stone, H. A. Effective slip in pressure-driven Stokes flow. *J. Fluid Mech.* **2003**, *489* (8), 55-77.
81. Cottin-Bizonne, C.; Barentin, C.; Charlaix, É.; Bocquet, L.; Barrat, J.-L. Dynamics of simple liquids at heterogeneous surfaces: Molecular-dynamics simulations and hydrodynamic description. *The European Physical Journal E* **2004**, *15* (4), 427-438.
82. Park, H.; Sun, G.; Kim, C.-J. C. In *Turbulent drag reduction on superhydrophobic surfaces confirmed by built-in shear sensing*, Micro Electro Mechanical Systems (MEMS), 2013 IEEE 26th International Conference on, 2013; IEEE, pp 1183-1186.
83. Spikes, H. A. The half-wetted bearing. Part 1: extended Reynolds equation. *Proceedings of the Institution of Mechanical Engineers, Part J: Journal of Engineering Tribology* **2003**, *217* (1), 1-14.
84. Spikes, H. A. The half-wetted bearing. Part 2: potential application in low load contacts. *Proceedings of the Institution of Mechanical Engineers, Part J: Journal of Engineering Tribology* **2003**, *217* (1), 15-26.

85. Choo, J.; Glovnea, R.; Forrest, A.; Spikes, H. A low friction bearing based on liquid slip at the wall. *Journal of Tribology* **2007**, *129* (3), 611-620.
86. Leong, J.; Reddyhoff, T.; Sinha, S.; Holmes, A.; Spikes, H. Hydrodynamic Friction Reduction in a MAC–Hexadecane Lubricated MEMS Contact. *Tribology Letters* **2013**, *49* (1), 217-225.
87. Choo, J.; Spikes, H.; Ratoi, M.; Glovnea, R.; Forrest, A. Friction reduction in low-load hydrodynamic lubrication with a hydrophobic surface. *Tribology International* **2007**, *40* (2), 154-159.
88. Epstein, A. H. Millimeter-scale, MEMS gas turbine engines. In *Proceedings of ASME Turbo Expo*, 2003, pp 1-28.
89. Dhariwal, R.; Flockhart, S. Finite element investigation into proposed bearing mechanism for a fluid driven micro actuator. *Microsystem technologies* **1999**, *5* (4), 200-204.
90. Cottin-Bizonne, C.; Jurine, S.; Baudry, J.; Crassous, J.; Restagno, F.; Charlaix, E. Nanorheology: An investigation of the boundary condition at hydrophobic and hydrophilic interfaces. *The European Physical Journal E* **2002**, *9* (1), 47-53.
91. Lee, C.; Kim, C.-J. C. Maximizing the giant liquid slip on superhydrophobic microstructures by nanostructuring their sidewalls. *Langmuir* **2009**, *25* (21), 12812-12818.

Chapter 3: Materials and Methods

This Chapter gives a general description of the experimental details, materials and methods used throughout the Thesis. However further discussion is presented in each results chapter where appropriate.

3.1 Electrochemical

Throughout this work an Autolab PGSTAT302N potentiostat with electrochemical impedance spectroscopy unit (EIS) was used to make electrochemical measurements and depositions.

3.1.1 Reference Electrode

A home-made saturated calomel electrode (SCE) which is based on the $\text{Hg} \leftrightarrow \text{Hg(I)Cl}$ couple was used throughout the work. When not in use the electrode was stored in a saturated KCl solution.

3.1.2 Electrochemical Deposition

The gold was plated under potentiostatic conditions at -0.72 V against the saturated calomel reference electrode at room temperature. A commercial gold plating solution was used (ECF 60, Metalor) with a brightener additive (E3, Metalor) 100 μl per 20 ml of plating solution.

The nickel plating bath is a Watts bath modified with saccharin to brighten the deposit (composition shown in figure 3.1). The nickel was plated potentiostatically at - 0.9 V vs SCE at room temperature.

Compound	Concentration (g/L)
Nickel (II) chloride hexahydrate	240
Nickel (II) sulphate hexahydrate	45
Boric acid	30
Saccharin	2

Figure 3.1 Contents of Watts bath for electroplating

3.2 Templated Electrodeposition

Templated electrodeposition is a surface texturing technique used throughout much of this Thesis. The general method starts by creating a 3 dimensional template on a conducting surface, the desired material is then electrodeposited around the template. The template is then often removed leaving a cast of the template, figure 3.2.¹

In this work the template is always made of a close packed monolayer of polystyrene colloidal particles. These colloids are commercially available in a range of sizes from 20 nm to > 10 μm and the standard deviation in diameter is generally less than 1 %.

Areas of 1 cm^2 can be easily created though a self assembly process as a solution containing monodisperse polystyrene particles is allowed to evaporate in a controlled environment. A microcell is made on the metal surface by using a parafilm wax spacer and a glass coverslip. The assembly is placed on to a hot plate at $\sim 70^\circ\text{C}$ which softens the parafilm, bonding the construction together. The colloid containing solution is injected into the space between the metal surface and glass coverslip. As the solution evaporates the colloids are drawn towards the meniscus where capillary immersion forces pull them together into a close packed arrangement (the most efficient packing density for spheres). The temperature at which the evaporation occurs significantly effects the quality of the resulting template. Using 600 nm diameter spheres the best temperature is 12°C and 3 μm diameter spheres is 40°C .

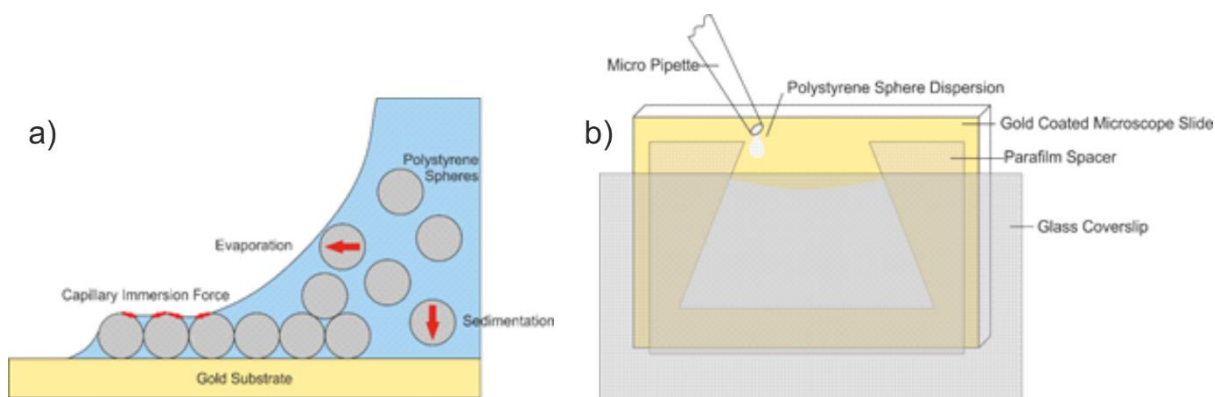


Figure 3.2 a) Mechanism of evaporation driven self organisation b) Sketch of microcell

These colloidal crystals show striking visual properties known as opalescence where the colour observed changes with the angle it's observed because of Bragg diffraction. This property is passed on to the inverse cast made of the electrodeposited material.

The desired material is electrodeposited around the colloidal crystal template, in this work gold and nickel are used however other metals and conducting polymers can also be used. A major advantage of using electrodeposition is that the charge can be carefully monitored allowing fine control over the film thickness. In some Chapters the deposition height is characterised by the ratio d of the film height to the diameter of the spheres.

After the material of choice has been electrodeposited the polystyrene spheres are dissolved in an organic solvent revealing the inverse structure of the template.

3.3 Contact Angle Measurement

A Kruss DSA100 contact angle apparatus was used to measure all contact angles. The circle drop fitting parameter was used to calculate the angle from the image. The average of three measurements was taken for each reported contact angle unless stated otherwise.

3.4 Spin Coating

The tert-butyl alcohol measured into a vial which was held in a water bath at 60°C. The 10:1 PDMS bulk and curing agent were mixed into the vial.

The substrate was held onto the spin coater chuck with a vacuum and was liberally coated with the solution after which the spinning cycle was started. The coated film was cured at 60°C in an oven overnight.

3.5 Scanning Electron Microscopy

A Philips XL30 environmental scanning electron microscope was used to image surfaces. The imaging parameters are detailed in each image. This imaging technique rasters a beam of electrons over the surface which are reflected towards a detector. The secondary electron detector was used during imaging.

3.6 Atomic Force Microscopy

MFP-3D atomic force microscope (Asylum Research, UK) was used in both tapping and contact mode with PNP-TR AFM probes (with 0.32 N/m spring constant).

3.7 References

1. Bartlett, P. N. Electrodeposition of Nanostructured Films Using Self-Organizing Templates. *Interface-Electrochemical Society* **2004**, 13 (4), 28-33.

Chapter 4: Wetting of Surfaces made of Hydrophobic Cavities

*This chapter explores the fundamental wetting properties of hydrophobic surfaces composed of hexagonally close packed cavities. A good understanding of the wetting properties is vital before trying to modify the surface for drag reducing applications. This work has been published as Lloyd, B. P.; Bartlett, P. N.; Wood, R. J. Wetting of Surfaces made of Hydrophobic Cavities. Langmuir **2015**, 31 (34), 9325-9330.*

4.1 Introduction

Superhydrophobic surfaces are often defined as having a static water contact angle of greater than 150° . However there are many other interesting wetting phenomena which can arise within the superhydrophobic state. Wang and Jiang¹ discussed five different modes of surface wetting of rough surfaces with static water contact angles above 150° ; the Wenzel state, the Cassie state, the “lotus” state, a transitional superhydrophobic state between the Wenzel and Cassie states, and the “gecko” state. In the Wenzel state, the water penetrates the surface roughness and the droplet is pinned at the surface, exhibiting a large contact angle hysteresis. In the Cassie state, the water droplet does not penetrate the surface roughness but sits on the tops of the asperities leading to low contact angle hysteresis^{2, 3} and a droplet that slides readily off the surface. The “lotus” state, named after the lotus leaf renowned for its self-cleaning properties², is a special case of the Cassie state in which the hierarchical surface roughness leads to exceptionally low contact angle hysteresis. In the transitional state there is some penetration of the water into the surface roughness so that the drop is no longer totally mobile on the surface and there is moderate contact angle hysteresis. Finally the “gecko” state, named for its high adhesive properties, is a variant of the Cassie state in which there are sealed pockets of trapped air which leads to an adhesive caused by the negative pressure in the sealed air pocket upon movement of the water droplet⁴. Subsequently Jiang’s group⁵ and Bhushan and Nosonovsky⁶ identified an additional “petal” state, named after the wetting behavior of the petals of different flowers and, in particular, the *Rosea* species. The “petal” state is a Cassie impregnating wetting state in which the water infiltrates the larger surface roughness but not the very smallest features of the hierarchical surface

roughness, Figure 4.1. This produces a surface, like the rose petal, that has a high contact angle but also large contact angle hysteresis and strong adhesion of the water droplet at the surface. The rose petal effect can be useful in drop transport in micro fluidics.^{4, 6}

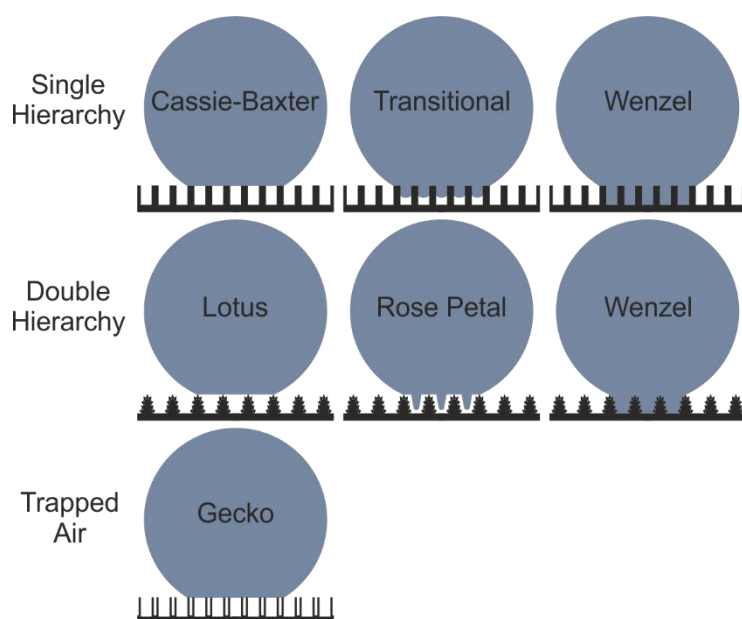


Figure 4.1: The possible superhydrophobic states for surfaces of single hierarchy (eg. posts)¹, double hierarchy (eg. the lotus leaf)⁶ and where air is trapped in sealed pockets and not connected to the atmosphere (eg. hollow polystyrene fibers)⁴.

Broadly, the types of structured surfaces investigated in the literature can be divided into two categories: roughened quasi random surfaces (e.g. roughened plastics)⁷ or designed surfaces with a repeating unit cell (e.g. a square array of posts).⁸ The latter group is much better suited to experiments hoping to understand the role of surface structure on the interaction with water and the use of square arrays of posts on a flat substrate has been the favored choice due to the simplicity of the structure and the ease of fabrication using lithographic methods. The roughened quasi-random surfaces are more relevant in many practical applications where properties such as cost and ease of fabrication of large areas are a priority.

In this chapter results are presented from a study of the wetting properties of hydrophobic surfaces made of close packed arrays of cavities and phenomena distinct to this particularly interesting geometry are highlighted. The electrodeposition around the template spheres produces a sculpted structure with a very smooth interior surface⁹ so that there is minimal hierarchical roughness over and above that of the geometric structure. Using this type of surface it is possible to make hydrophobic surfaces using unmodified, locally hydrophilic gold surfaces due to the curvature of the cavity sidewalls.^{10, 11}

4.2 Experimental

The surfaces were made using the templated electrodeposition method discussed in Chapter 3.

The template was formed by the self-assembly of monodisperse 3 μm polystyrene latex spheres (Duke Scientific) driven by evaporation into a close-packed arrangement. The substrate was a glass slide on to which a ~ 300 nm layer of gold had been evaporated, with a ~ 50 nm layer of chromium to aid adhesion. Gold from a commercial plating solution (Metalor and brightener) was plated to different heights around the spheres at a potential of -0.72 vs. a saturated calomel reference electrode. The spheres were dissolved in tetrahydrofuran. To decrease the surface energy of the gold a self-assembled monolayer of alkylthiol was attached.¹² The substrate was left in a solution of 10 mM 1-dodecanethiol in ethanol for 1 day; this led to a contact angle of $\sim 110^\circ$ on flat gold.

Advancing and receding angles were taken by pumping in to and out of the drop at a rate of $0.5 \mu\text{l min}^{-1}$.

4.3 Results and Discussion

Fine control of the gold film height is achieved in the fabrication process by carefully monitoring the charge passed during electrodeposition. It is important to note that electrodeposition of gold through the template under these conditions leads to the formation of a very smooth gold surface (smoother than that formed by evaporation of gold) around the polystyrene spheres⁹ so that there is very little hierarchical roughness for these structure over and above the geometric roughness defined by the template. Measuring between the cavities on the top of the surface using an atomic force microscope (MFP-3D, Asylum Research, U.K.) the R_a is found to be 5 ± 1.5 nm.

The range of surface structures are described in terms of their normalized thickness d , defined as the film height divided by the sphere diameter. In the following the d value is used as a simple way to denote the different fabricated surface structures (Figure 4.2a). Thus at $0.5 d$ the deposited film height is $1.5 \mu\text{m}$, half of the sphere diameter of $3 \mu\text{m}$. In this study 0.1 , 0.2 , 0.3 , 0.4 and $0.5 d$ surfaces are considered. Scanning electron microscopy was used to obtain high resolution images of the surfaces, Figure 4.2b. These show that the surfaces are well formed and geometrically regular as expected for templating of this type. This regularity extends of distances of 1 mm. As d increases from 0 to 0.5 the surface geometry of the film evolves with the area fraction covered by cavities and the side wall angle at the rim of the cavity systematically changing in a predictable

manner with d . This affects the wetting properties of the surface as discussed below. This template electrodeposition method used gives excellent control over the surface geometry and can be used with a range of sphere sizes and for a range of metals¹³ and alloys as well as some conducting polymers¹⁴. For gold the surface properties can be altered, as here, by using self assembled thiol monolayers giving rise to a broad range of surfaces not easily accessible with traditional lithographic methods.

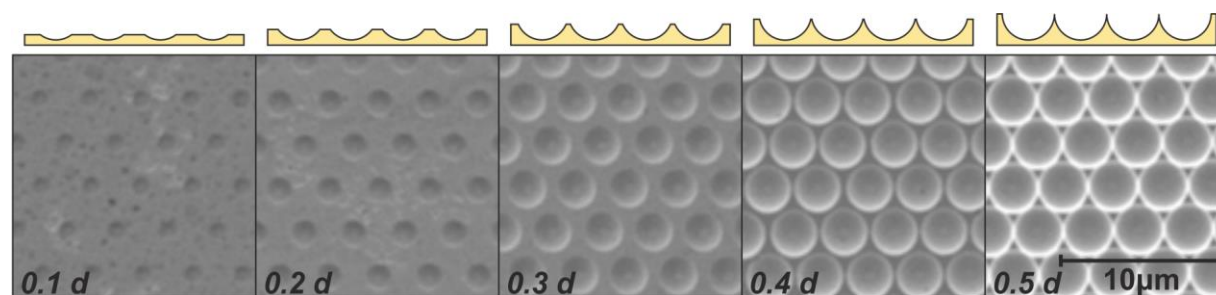


Figure 4.2 Schematic cross sections of the voids and scanning electron micrographs of the surfaces prepared by templated electrodeposition of gold around close packed polystyrene spheres. The height of the gold deposition has been varied from 0.1 to 0.5 d .

The gold surfaces were modified by the adsorption of a self assembled monolayer of 1-dodecanethiol and then the advancing and receding contact angles were recorded as a function of d . On the flat gold surface the 1-dodecanethiol monolayer renders the originally hydrophilic surface of the clean gold hydrophobic with an advancing contact angle of 110° . The results for contact angle measurements as a function of d are shown in Figure 4.3. It is clear that there is significant hysteresis and that the advancing and receding contact angles behave in different ways as d increases.

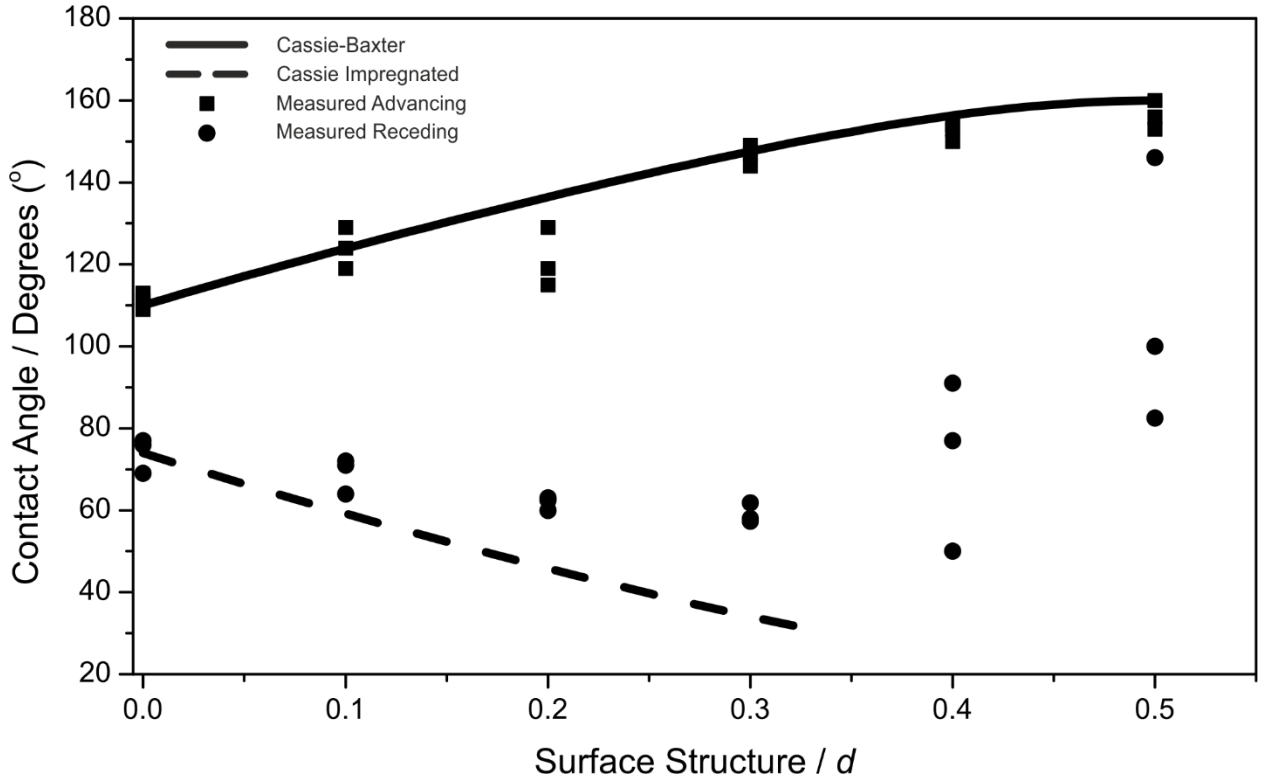


Figure 4.3 Plot showing the experimental advancing (squares) and receding contact (circles) angles as a function of the dimensionless film height, d . The Cassie-Baxter equation is also plotted (solid line) assuming that the cavities are air-filled. The equation for the Cassie impregnated state is shown in the dashed line assuming the cavities are water filled.

We begin by considering the advancing contact angles. As d increases these increase steadily reaching around 150° , a superhydrophobic surface, at $0.5 d$. For the Cassie state, where the droplet is supported on the asperities and does not infiltrate the surface roughness, the apparent advancing contact angle, θ_{adv}^* , is given by

$$\cos\theta_{adv}^* = \Phi_s \cos\theta_{adv} - (1 - \Phi_s) \quad (4.1)$$

where Φ_s is the solid fraction of the surface and θ_{adv} is the advancing contact angle on the corresponding flat surface ($\Phi_s = 1$).¹⁵ In this simple model the non-solid fraction of the surface (here the mouths of the spherical cavities) are assumed to be non-wetting with a contact angle 180° . From the surface geometry for a hexagonally close packed array of sphere segment voids the solid fraction Φ_s (corresponding to the flat area between the cavities) is related to d by

$$\Phi_s = 1 - \left(\frac{\pi}{2\sqrt{3}}\right) (1 - (1 - 2d)^2) \quad (4.2)$$

Combining equations (4.1) and (4.2) the predicted apparent advancing contact angle for the simple Cassie Baxter model can be calculated as a function of film thickness, d , for any given value of θ_{adv} , the advancing contact angle on the flat surface. In this case θ_{adv} was found experimentally to be 110° . Taking this value and equations (4.1) and (4.2) the calculated curve plotted in Figure 4.3 is obtained. It is striking that there is excellent agreement between the calculate values and our experimental results for the apparent advancing contact angle. Based on this we conclude that as the contact line advances the sphere segment cavities remain filled with air and in the advancing condition the system adopts the Cassie-Baxter state.

Turning now to the receding contact angles, it is clear that the receding angle is controlled by a different mechanism – it does not follow the Cassie Baxter prediction and there is significant contact angle hysteresis. This leads to strong pinning of the water droplet to the surface as discussed below. Since the Cassie-Baxter model clearly does not work we assume that the cavities under the drop must become, at least in part, infiltrated by the water. Assuming the cavities to be completely wetted (contact angle 0°), the so-called Cassie impregnated state, the apparent receding contact angle θ_{rec}^* can be estimated using the expression^{6, 16}

$$\cos\theta_{rec}^* = \Phi_s \cos\theta_{rec} + (1 - \Phi_s) \quad (4.5)$$

where θ_{rec} is the receding contact angle on the flat surface and Φ_s is defined by the geometry and given by equation (4.2). Using Equation (4.4) we can calculate θ_{rec}^* as a function of d taking the measured values for θ_{rec} at the flat surface (in this case 74°). The result is plotted as in Figure 5 as the dashed line. Equation (4.5) predicts a decreasing value for the apparent receding contact angle but that up to a d value of 0.3 it rather over estimates the effect. For $d > 0.3$ the situation changes and the apparent receding contact no longer decrease with increasing d and that there is now a large scatter in the values (Figure 4.3). This suggests partial filling of cavities – somewhere between the two wetting states. It may be significant that a d value of 0.33 corresponds to a contact angle for a flat, horizontal surface on the sphere segment cavity wall of 110° .

Throughout the range of surfaces tested there is a large contact angle hysteresis. For d of 0.5 large hysteresis is coupled with a high (advancing) contact angle – these are characteristics of the “petal effect”. Bhushan obtained “petal effect” by using a two tier hierarchy in which the larger features were wetted but the smaller ones were not.⁶ Here we see same effect for surfaces that do not have hierarchical roughness, that is the surfaces of these geometric sphere segment void surfaces are smooth. The hysteresis on these hydrophobic SSV surfaces is large enough for the substrate to be completely inverted at all values of d and for the drop to remain stationary, although the contact angle is reduced in the process (Figure 4.4). As the drop is removed from the needle the contact angle is decreased as it recoils from the needle detaching (Figure 4.4b)– a similar effect, referred to

as the water hammer effect, was reported by Patankar *et al.*¹⁷ for water on an array of square posts. The contact angle further decreases on complete inversion (Figure 5c) and also as it is returned to original horizontal position (Figure 4.4d). Note that the apparent contact angles at the start (140°) and the end (119°) of this procedure are not the same indicating some movement of the contact line during the inversion process.

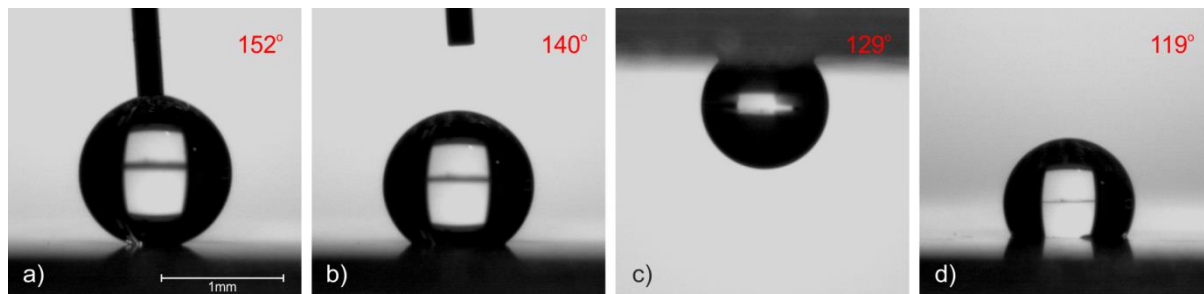


Figure 4.4 A sequence of images of the same 0.5 μl water drop on surface with d of 0.5. The corresponding values of apparent contact angle are also shown. a) The drop is extruded and the needle lowered so the drop contacts the surface, b) the needle is removed from the drop, the contact angle is decreased as the drop recoils back onto the surface, c) the surface is fully inverted, d) the surface rotated back to its original position.

The three phase contact line can also be strongly pinned at the edge of the cavities when drops evaporate on such a surface which causes large contact angle hysteresis.¹⁸ Birembaut *et al.* demonstrated this effect on a substrate with square-pyramidal pits arranged in a square lattice.¹⁹ As a drop evaporated on the surface the three phase contact line became strongly pinned on the edges of the square sided pits leading to a corrugated droplet edge. Pinning of a droplet on the surface in this way is consistent with high contact angle hysteresis.

Optical microscopy was used to view the receding three phase contact line on our hydrophobic SSV surface. In these experiments a 1 μl drop was deposited on to the surface and allowed to slowly evaporate, driving the receding motion of the interface. Under these conditions pinning of the contact line on the edges of the cavities is observed (Figure 4.5). This is consistent with the work of Zhu *et al.* who used a similar surface of ‘microbowl arrays’¹⁸ and also Birembaut *et al.* with square pyramidal pits.¹⁹

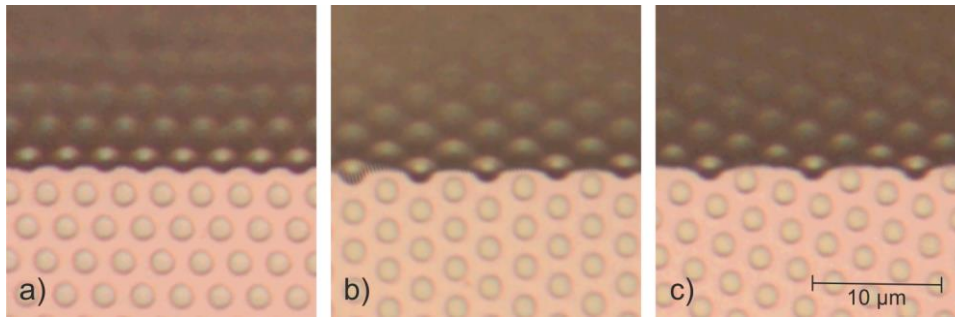


Figure 4.5 Optical microscope images of the three phase contact line receding over a hydrophobic SSV surface with d of 0.3. The regular array of sphere segment cavities is clearly seen with the darker (water covered) surface at the top of the image in each case. Pinning is seen along the: a) (10), b) (11), and c) (12) lines of cavities of the hexagonal array.

As Zhu *et al.* noted, each individual cavity pins the contact line in a quasi-static state which occurs due to a local energy minima.¹⁸ Further to this we add that when the cavities are hexagonally close packed, different direction on the surface give different numbers of cavities per unit length of three phase contact line. Therefore directions with a high density of cavities per unit length of contact line pin the interface more effectively. The highest density of cavities per unit length is along the $\{10\}$ lines and decreases through the $\{11\}$ and $\{12\}$ and so on. An interesting consequence of this is that when left to evaporate the perimeter of a drop will tend to form a dodecagonal shape as the three phase contact line is pinned more strongly on the $\{10\}$ lines joined by shorter lengths of the $\{11\}$ lines as shown in the top down image of a complete drop in Figure 4.6.

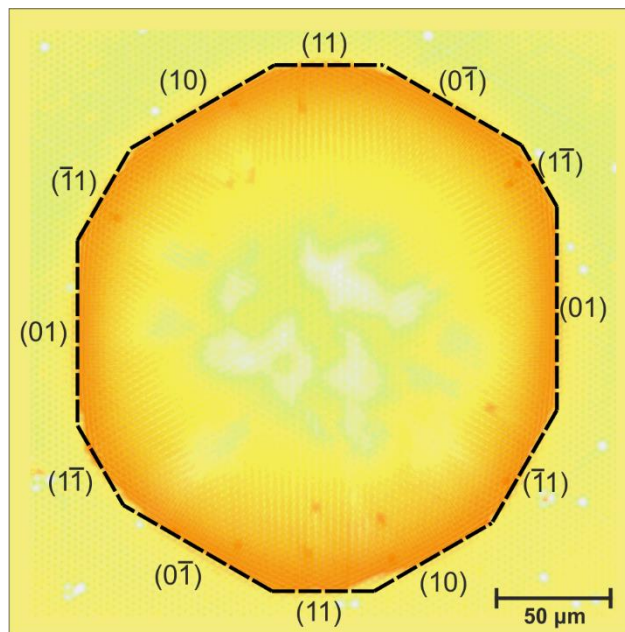


Figure 4.6 A dodecagonal drop formed by the evaporation of water drop on a hydrophobic SSV surface with d of 0.5. The sides are pinned on the $\{10\}$ and $\{11\}$ lines.

4.4 Conclusions

Templated electrodeposition through close packed monolayer arrays of polystyrene spheres followed by removal of the template by dissolution in an organic solvent has been used to fabricate sphere segment void (SSV) surfaces in gold containing 3 μm diameter sphere segment cavities with heights up to 1.5 μm . The surfaces of these structures were made hydrophobic by treating with 1-dodecanethiol to form a self assembled monolayer at the gold surface. Contact angle measurements on these surfaces show that the wetting behavior of these surfaces changes significantly with film thickness. The apparent advancing contact angle increases as the thickness of the film, and therefore the depth of the sphere segment cavities, increases going from a value of 110° on the 1-dodecanethiol coated flat surface to around 150° for the thickest film where the cavities in the film are hemispherical. For the apparent advancing contact angle good agreement is found between the measured values and those calculated using the known geometry and the Cassie Baxter equation. In contrast receding angle measurements show a significant hysteresis in all cases so that the water droplets are strongly pinned at the surface. Indicating some level of infiltration of the hydrophobic surface by the water. Thus these surfaces show the “petal effect”^{5,6} in which a large apparent advancing contact angle, typical of a superhydrophobic surface, is accompanied by significant contact angle hysteresis. In contrast to the “petal” surfaces reported so far and in contrast to the structure of the rose petal itself, our hydrophobic SSV gold only has a single level of structuring with a smooth geometric surface defined by the template in contrast to the hierarchical structure of the rose petal itself and other “petal” surfaces.

This hysteresis is so large that the water drops remained stationary on the SSV surface even when it was inverted. Observation of the shapes of drops on the surface during evaporation driven recession shows that regular surface structure, with features on the 3 μm scale, influences the macroscale shape of the water drop. Under evaporation driven recession the drops adopt a dodecagonal shape in which the drop perimeter is selectively pinned along the $\langle 10 \rangle$ and $\langle 11 \rangle$ directions on the hexagonally close packed surface. This is consistent with the strongest pinning of the triple line occurring along the directions with the highest density of cavities in the surface.

Templated electrodeposition and surface modification with a hydrophobic self assembled monolayer is clearly a viable method to prepare “petal” surfaces with one layer of structural hierarchy. These surfaces may find use as substrates for droplet transport.⁴

With regard to the aim of the thesis the large contact angle hysteresis shows that there is some degree of penetration of water into the cavities; which is undesirable for drag reducing applications. This indicates that means to actively replenish the gas in the cavities is required to keep the surface in the low drag Cassie state.

4.5 References

1. Wang, S.; Jiang, L. Definition of superhydrophobic states. *Adv. Mater.* **2007**, *19* (21), 3423-3424.
2. Barthlott, W.; Neinhuis, C. Purity of the sacred lotus, or escape from contamination in biological surfaces. *Planta* **1997**, *202* (1), 1-8.
3. Patankar, N. A. Mimicking the lotus effect: influence of double roughness structures and slender pillars. *Langmuir* **2004**, *20* (19), 8209-8213.
4. Jin, M.; Feng, X.; Feng, L.; Sun, T.; Zhai, J.; Li, T.; Jiang, L. Superhydrophobic aligned polystyrene nanotube films with high adhesive force. *Adv. Mater.* **2005**, *17* (16), 1977-1981.
5. Feng, L.; Zhang, Y.; Xi, J.; Zhu, Y.; Wang, N.; Xia, F.; Jiang, L. Petal effect: a superhydrophobic state with high adhesive force. *Langmuir* **2008**, *24* (8), 4114-4119.
6. Bhushan, B.; Nosonovsky, M. The rose petal effect and the modes of superhydrophobicity. *Phil. Trans. R. Soc. A* **2010**, *368* (1929), 4713-4728.
7. Erbil, H. Y.; Demirel, A. L.; Avci, Y.; Mert, O. Transformation of a simple plastic into a superhydrophobic surface. *Science* **2003**, *299* (5611), 1377-1380.
8. Bico, J.; Marzolin, C.; Quéré, D. Pearl drops. *EPL* **1999**, *47*, 220.
9. Ben-Ali, S.; Cook, D. A.; Evans, S. A.; Thienpont, A.; Bartlett, P. N.; Kuhn, A. Electrocatalysis with monolayer modified highly organized macroporous electrodes. *Electrochem. Commun.* **2003**, *5* (9), 747-751.
10. Abdelsalam, M. E.; Bartlett, P. N.; Kelf, T.; Baumberg, J. Wetting of regularly structured gold surfaces. *Langmuir* **2005**, *21* (5), 1753-1757.
11. Patankar, N. A. Hydrophobicity of Surfaces with Cavities: Making Hydrophobic Substrates from Hydrophilic Materials? *J. Adhesion Sci. Technol.* **2009**, *23* (3), 413-433.
12. Bain, C. D.; Whitesides, G. M. Formation of monolayers by the coadsorption of thiols on gold: variation in the length of the alkyl chain. *J. Am. Chem. Soc.* **1989**, *111* (18), 7164-7175.
13. Bartlett, P. N.; Birkin, P. R.; Ghanem, M. A. Electrochemical deposition of macroporous platinum, palladium and cobalt films using polystyrene latex sphere templates. *Chem. Commun.* **2000**, (17), 1671-1672.
14. Bartlett, P. N.; Birkin, P. R.; Ghanem, M. A.; Toh, C.-S. Electrochemical syntheses of highly ordered macroporous conducting polymers grown around self-assembled colloidal templates. *J. Mater. Chem.* **2001**, *11* (3), 849-853.
15. Cassie, A.; Baxter, S. Wettability of porous surfaces. *Trans. Faraday Soc.* **1944**, *40*, 546-551.
16. Nosonovskii, M.; Bhushan, B. *Multiscale dissipative mechanisms and hierarchical surfaces: friction, superhydrophobicity, and biomimetics*; Springer 2008.
17. Kwon, H.-M.; Paxson, A. T.; Varanasi, K. K.; Patankar, N. A. Rapid deceleration-driven wetting transition during pendant drop deposition on superhydrophobic surfaces. *Phys. Rev. Lett.* **2011**, *106* (3), 036102.
18. Zhu, X.; Zhang, C.; Liu, X.; Hansen, O.; Xiao, S.; Mortensen, N. A.; Zi, J. Evaporation of Water Droplets on "Lock-and-Key" Structures with Nanoscale Features. *Langmuir* **2012**, *28* (25), 9201-9205.
19. Birembaut, F.; Perney, N.; Pechstedt, K.; Bartlett, P. N.; Russell, A. E.; Baumberg, J. J. Sharp - Cornered Liquid Drops by Wetting of Nanoscale Features. *small* **2008**, *4* (12), 2140-2142.

Chapter 5: Active Gas Replenishment and Sensing of the Wetting State in a Submerged Superhydrophobic Surface

This chapter builds on the work of the previous chapter by modifying the surface design and using electrochemical methods to allow measurement of the wetting state of the surface and top up of the gas within the cavities.

5.1 Introduction

Superhydrophobic surfaces have shown great promise reducing skin friction drag in laminar ¹ and turbulent flows² by supporting a layer of gas on the solid surface.³ However recently experiments have shown the dissolution of the gas film into the surrounding water means the low drag properties are short lived.^{4,5,6} Without a full coverage of gas on the surface in the Cassie state, low drag cannot be realised. Methods to quantify the gas volume and to replenish gas as it dissolves are required to progress the use of superhydrophobic surfaces from the laboratory into a more applied areas.

When drops of water are deposited onto superhydrophobic surfaces in the majority of cases the gas beneath the drop is still connected to the atmosphere so dissolution does not lead to a change in the wetting state. However some surfaces trap gas beneath drops where the wetting properties could be altered by the dissolution of the gas.⁷ When fully submerged all superhydrophobic surfaces are susceptible to dissolution induced wetting transitions. Some experiments looking at the drag reducing properties of gas laden surfaces have neglected to carefully measure the wetting state, indeed, adding means to gain *in situ* information on the gas film is certainly a challenging problem in larger scale towing tank tests. The unknown wetting state of surfaces in such tests is the likely cause of the large discrepancy between published results in this area. If such surfaces are to be introduced into real world situations nonvisual information about the wetting state will be vital to their operation.

The sensing of the wetting state of superhydrophobic surfaces in laboratory conditions is often achieved by visual inspection using an optical microscope, the presence of gas is observed as silver coloured reflection in the light from the microscope.^{6, 8, 9} This method is simple and quick, however it only gives qualitative rather than quantitative information of the presence of a gas layer. In some cases the raw image is processed to give a binary black and white image to which wetted and non wetted areas are assigned. This is likely to overly simplify the system as it does not consider the transition between the two states.

Surfaces with relatively large (on a scale of hundreds of micrometres) and regular patterns, such as posts and gratings, seem to lend themselves to easy visual determination of the wetting state with the use of a microscope. However when the features are smaller or irregular it becomes impossible to use optical methods to identify a wetted surface from one with a full gas coverage.¹⁰ Specialised systems such as laser scanning confocal microscopy and fluorescence labelled water can show exactly the position of the three phase contact line within the surface structures but are much slower and difficult carry out *in situ*.⁴

At a superhydrophobic surface the solid area exposed to the liquid increases as the gas is displaced; electrochemical methods are well suited to measuring this change in wetted area. A considerable benefit of electrochemical area determination is that it does not rely on a line of sight with the surface, as is the case with optical methods. Two groups have shown this type of measurement to be effective. Tuberquia *et al.* measured the impedance of their superhydrophobic rough polymethylene surface as it was immersed in water.¹⁰ Ethanol was added to the water in a stepwise fashion which reduced the liquid surface tension progressively wetting the surface. The impedance was measured throughout the process and decreased as more of the surface was wetted. Dhindsa *et al.* measured the capacitance of a superhydrophobic surface as the gas film was displaced by electrowetting; as the surface was wetted the capacitance increased.¹¹

Even when the water is saturated with dissolved air the gas held within a superhydrophobic surface with a geometry capable of significant drag reduction in large scale fluidic systems will start to dissolve when submersed more than a few centimetres.⁵ This means that if superhydrophobic surfaces are to be successful at reducing drag for prolonged periods a method by which gas is actively replaced is a necessity. Kim and Lee designed and made a surface to reverse the wetting transition caused by dissolution of the gas or water pressure.¹² Hydrogen gas was generated electrochemically by the splitting of the water when it contacted regions of the surface. They showed that for the spread of the gas film between pillars or along a grating the bottom of the surface must itself be superhydrophobic – which they achieved using a nanostructured texture

covered in a layer of Teflon. However once this layer became wetted reversal of the wetting transition was not possible.

Here a novel surface design used in conjunction with electrochemical methods which allow the easy measurement of the wetted area of the surface and which tops up gas once it has dissolved is demonstrated. The surface for this work is based on the templated electrodeposition method developed by Bartlett *et al.*^{7,13} The surface consists of a hexagonally close packed array of metallic cavities topped with a thin polymer layer which is electrically insulating and hydrophobic.

Functionality is brought to the surface by using it as the working electrode in a three electrode system, in this sense the surface is active rather than the majority of superhydrophobic surfaces which are passive. The surface design means that in the desired Cassie state the electrochemical circuit is open; the water rests on the polymer film on top of the cavities and does not touch the metal side walls of the cavities. However in the undesirable wetted state the electrochemical circuit is closed as the water contacts the metal. This self actuation afforded by the novel surface geometry allows both quantification of the wetting state and replenishment of the gas through the electrolysis of water to produce hydrogen in the cavities.

5.2 Experimental

To fabricate the superhydrophobic surface templated electrodeposition was employed,¹³ the process is shown in figure 5.1. The template consists of a close packed array of 3 μm diameter polystyrene spheres (Polysciences) formed by an evaporation driven self assembly process. Nickel was deposited around the spheres to half the sphere height. A film of poly(dimethylsiloxane) (PDMS) was spin coated on the nickel deposit and template; using 10% PDMS (Dow Corning Sylgard 184) in tert-butanol at 8000 RPM for 5 minutes using a (WS-650 by Laurell Technologies) which gave a film thickness of ~ 80 nm. The spheres were dissolved using tetrahydrofuran. The resulting surface had a projected area of 0.1 cm^2 and was composed of exposed metal cavities topped with a thin PDMS layer, figure 2. Images of the surface were obtained using a scanning electron microscope (Philips XL 30 ESEM).

A three electrode system was used and was controlled with a potentiostat (Autolab PGSTAT302N) where the potential was measured against a saturated calomel reference electrode. The sample was used for the working electrode and a platinum wire mesh was used for the counter electrode

they were arranged facing one another 1 cm apart. An aqueous 0.1 molar phosphate buffered solution at pH 7 and 20 C° was used for the electrolyte.

The dissolved gas concentration was controlled by vacuum degassing when required and was measured using a dissolved oxygen probe (DS300 by Eutech). Parafilm was used to cover the solution surface once the desired dissolved gas concentration had been achieved to reduce gas exchange to and from the atmosphere.

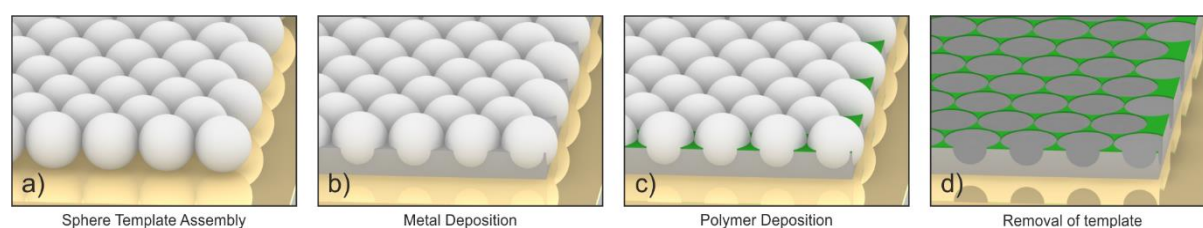


Figure 5.1 Schematic showing the steps involved to fabricate the desired surface. a) Assembly of 3 μm polystyrene latex spheres in to a close packed monolayer. b) Electrodeposition of nickel to half the sphere height. c) Spin-coating deposition of poly(dimethylsiloxane). d) Removal of polystyrene spheres by dissolving in tetrahydrofuran.

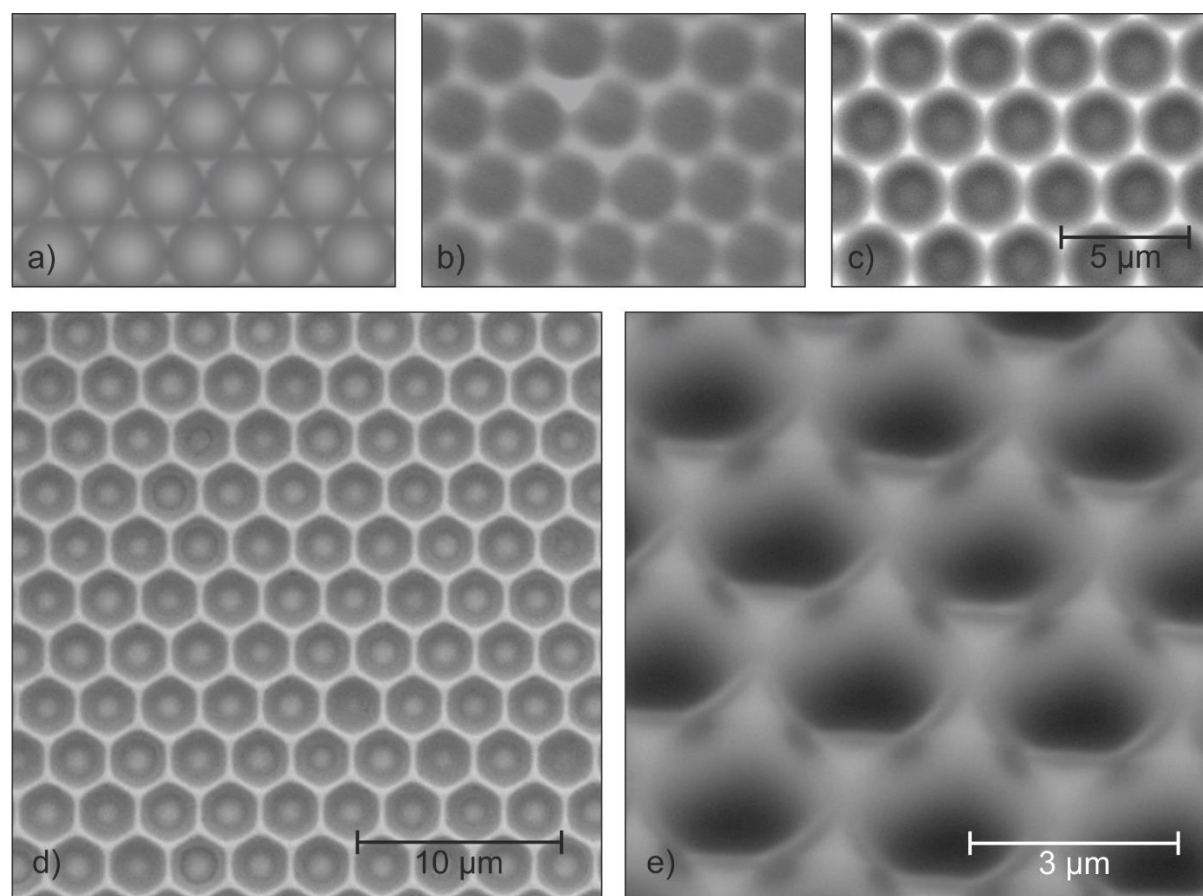


Figure 5.2 Scanning electron microscope images of the surface a) Polystyrene spheres with nickel electrodeposited to half the sphere diameter b) PDMS spin coated over polystyrene sphere

template and nickel c) PDMS and nickel after the sphere template has been dissolved away d) The surface showing long range order in finished surface. The PDMS is seen as the lighter coloured area between cavities. e) The surface shown at higher magnification and at an angle.

5.3 Results and Discussion

The superhydrophobic surface was made based on the templated electrodeposition method described in chapter 3 but modified for the purposes of this work. The template was formed using 3 μm diameter polystyrene spheres around which nickel was electrodeposited to half the sphere height. A thin film ($\sim 80\text{ nm}$) of poly(dimethylsiloxane) was then spin coated onto the surface which selectively covers the top of the surface. The spheres were then removed by dissolution in tetrahydrofuran. The resulting surface consists of exposed metallic cavities and a thin layer of PDMS covering the metal on the top of the structures; SEM images of the surface are shown in figure 5.2.

The superhydrophobic surface is submerged to a depth of 1 cm in 0.1 M pH 7 phosphate buffered electrolyte and used as the working electrode in a three electrode system. Using this system two functionalities are explored. 1. The measurement of the wetted area of the cavities as the trapped gas within the cavities dissolves into the surrounding liquid and 2. The top up of the gas to maintain the Cassie state as the gas dissolves.

There are many ways to measure the area of an electrode by electrochemical means.¹⁴ However several methods require the introduction of probe chemicals to the solution or oxidise and reduce the metal surface, which would lead to material loss. Measurement of the capacitance using electrochemical impedance spectroscopy (EIS) avoids both of these issues and is also fast to measure ($< 30\text{ s}$).

Impedance measurements were taken at 15 frequencies between 1000 and 10000 Hz using a potential modulation of $\pm 5\text{ mV}$ (rms) about a potential of -0.1 V vs. SCE reference electrode. No significant Faradaic processes were found at this potential.

A Nyquist plot of a flat nickel electrode is shown in figure 5.3 a), the circuit is assumed to be a resistor and capacitor in series (RC), where the resistance is dominated by the resistance of the solution and the capacitance by the electrical double layer capacitance. The graph shows a deviation from the response of an RC circuit, which should be a vertical line, however the observed

non-vertical line is typical of electrochemical systems and are treated as a constant phase element¹⁵ where the impedance, Z , is given as:

$$Z = R + \frac{1}{(j\omega)^\alpha C} \quad (5.1)$$

Where R is the resistance, j is the imaginary number $\sqrt{-1}$, ω is the frequency in rad s^{-1} , α is an exponent describing the deviation from ideal capacitive behaviour and C is the capacitance. Equation 5.1 is fitted to the measured data to obtain the resistance and capacitance. The value of α is measured to be 0.99 for this system. All following capacitance measurements were obtained in this manner.

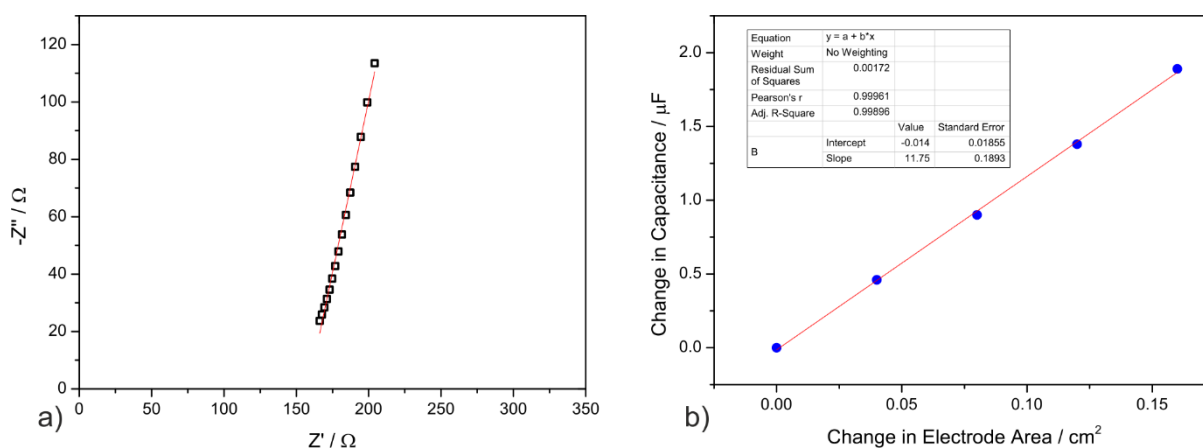


Figure 5.3 a) Nyquist plot for a nickel electrode in 0.1 M phosphate buffer at - 0.1 V vs SCE reference b) Change in capacitance plotted against change in electrode area. The blue circles show the capacitance measurements and the red line is a linear fit of the data.

A micro adjuster was used to submerge a 4 mm wide rectangular nickel electrode in 1 mm intervals to increase its wetted area and capacitance measurements were taken after each step. The relationship between electrode area and capacitance is displayed in Figure 5.3 b) and shows they are directly proportional to one another. The red line shows a linear fit (R-squared of >0.99) with a gradient of $11.8 \mu\text{F cm}^{-2}$ which agrees well with values in the literature for the double layer capacitance.¹⁴ This demonstrates that measurement of the capacitance using EIS under these conditions is suitable for the reliable determination of electrode area.

Previous work by Tuberquia *et al.*¹⁰ and Dhindsa *et al.*¹¹ detected changes in electrochemical response between the Cassie and fully wetted states. The transition between the states was promoted by reduction of the liquid surface energy by addition of methanol and electrowetting respectively. In this work the gas is allowed to dissolve into the surrounding solution. This allows us

to demonstrate a functional method to measure wetted area and understand the lifetime of the trapped gas at the surface with respect to dissolution.

The cavity surface was submersed in the solution and the wetted area was measured as the gas within the cavities dissolved, exposing a greater solid/liquid interface. Capacitance measurements were started immediately after submersion. The term specific surface capacitance is used for this measured value. The change in specific surface capacitance and wetted fraction against time is shown for two conditions; where the solution had be pre-treated to 80 % air saturation and 100% air saturation.

The 80 % saturation condition is shown in figure 5.4 a). As expected initially the specific surface capacitance is low as the cavities are gas filled, but increases quickly as the gas dissolves readily into the under-saturated solution, wetting the cavities. A stable specific surface capacitance reading is reached when the surface is completely wetted. This shows the fully wetted sample has a specific surface capacitance of $20 \mu\text{F cm}^{-2}$. The same reading was gained after full degasing under vacuum which confirms this is indeed the fully wetted state. The wetted fraction of the sample is calculated by dividing a given capacitance density by this fully wetted specific surface capacitance of $20 \mu\text{F cm}^{-2}$, so the wetted fraction = 1 for the fully wetted state and 0 for the Cassie state. The wetted fraction is shown in the right y-axis for both conditions in figure 5.4. The fully wetted specific surface capacitance is slightly less than would be predicted from the value of $11.8 \mu\text{F cm}^{-2}$ multiplied by the ~ 3.6 times increase in area due to the surface geometry (the exposed metal area of the cavity divided by the projected area of the unit cell).

Under 100 % saturated conditions, figure 5.4 b), the initial capacitance is near zero and then increases with time. The rate of change in capacitance is much slower than the ~ 80 % saturation condition, which is to be expected. In this case the experiment was terminated at ~ 6.5 hrs before the surface was completely wetted.

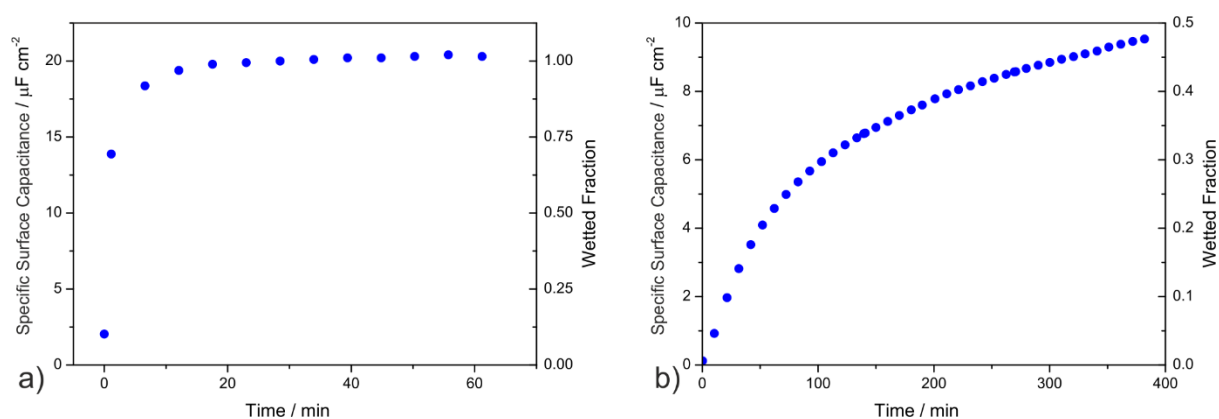


Figure 5.4 graphs showing the specific surface capacitance and wetted fraction over time as the gas trapped in the cavities dissolves in a) 80 % gas saturation conditions and b) 100 % gas saturation conditions in 0.1 M phosphate buffer.

The PDMS coated areas also contribute to the double layer capacitance despite being insulating. However their contribution to the capacitance is dwarfed by the nickel response – the initial reading in 100 % saturated conditions where the nickel area is at a minimum is $0.1 \mu\text{F cm}^{-2}$ which is 0.5% of the fully wetted state where the nickel area is its largest.

These experiments demonstrate the susceptibility of the gas layer to dissolution even in 100% saturated conditions and show the need for an active method to replace gas once it is lost.

To replace gas which is lost through dissolution hydrogen was evolved directly from the surrounding water which means the total volume of gas the surface can produce is unlimited. Hydrogen evolution occurs at the negatively charged cathode, meaning oxidation of the surface is also prevented. A cyclic voltammogram of a flat nickel electrode is shown in figure 5.5, where hydrogen evolution onsets from around -0.75 V vs. SCE .

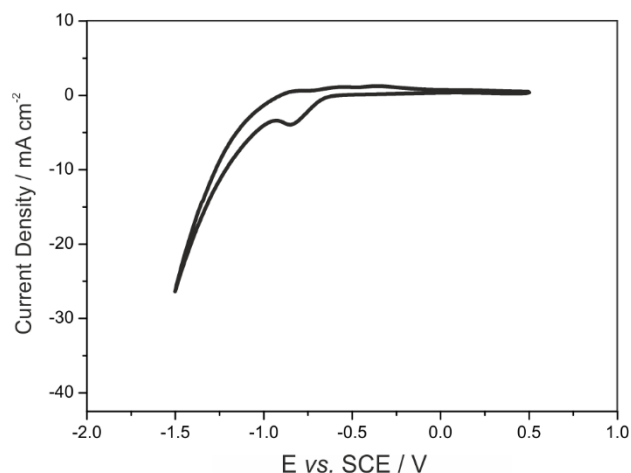


Figure 5.5 Cyclic voltammetry of nickel in 0.1 M pH 7 phosphate solution at 50 mV s^{-1} . Hydrogen evolution starts at -0.75 V and rate of production increases as the potential scans more negative.

The sample was submersed into saturated water and the surface was set to -1.5 V vs. SCE. Measurements of the capacitance were taken every 5 mins to measure the wetted area of the surface during which time hydrogen evolution was temporarily ceased, figure 5.6.

Throughout the experiment the current density remains fairly constant between -100 and -200 $\mu\text{A cm}^{-2}$ as hydrogen is evolved when required. The specific surface capacitance also remains constant at around 40 nF cm^{-2} indicating the cavities are kept dry by the production of hydrogen throughout the experiment. A sketch of the topping up process is shown in figure 5.7.

The novel geometry of the surface regulates the gas production, self actuating when needed and self limiting when not. In the desired Cassie state the water only touches the insulating PDMS layer and the electrochemical circuit is open, but in the undesirable situation where water intrudes into the metal cavity the circuit is closed. Fig 5.8 b) shows the current transients at higher resolution. There is an initial larger current due to charging of the double layer and a larger metal area exposed after the 30 s EIS measurement when hydrogen production ceased. The current density then reaches a plateau after ~ 30 s.

From the current density the rate of hydrogen production is approximated to be $\sim 1.9 \times 10^{-11} \text{ m}^3 \text{ s}^{-1} \text{ cm}^{-2}$. This assumes 100 % faradaic efficiency and that all hydrogen is in the gas state, however much of the hydrogen will be dissolved in the solution. From the graph in figure 6 b) showing dissolution of air into the 100% saturated solution the initial rate of dissolution is approximated to be $\sim 1.2 \times 10^{-14} \text{ m}^3 \text{ s}^{-1} \text{ cm}^{-2}$. This ~ 1000 fold difference is likely due to the fact that the water is completely desaturated with respect to hydrogen and therefore it dissolves at a very high rate compared to when the cavities are filled with just air. The surface consumes a power of $\sim 2.5 \mu\text{W}$ per centimetre squared to maintain the Cassie state. This experiment demonstrates that by holding the surface potentiostatically at -1.5 V a full gas coverage can be successfully maintained when it would have otherwise been lost through dissolution.

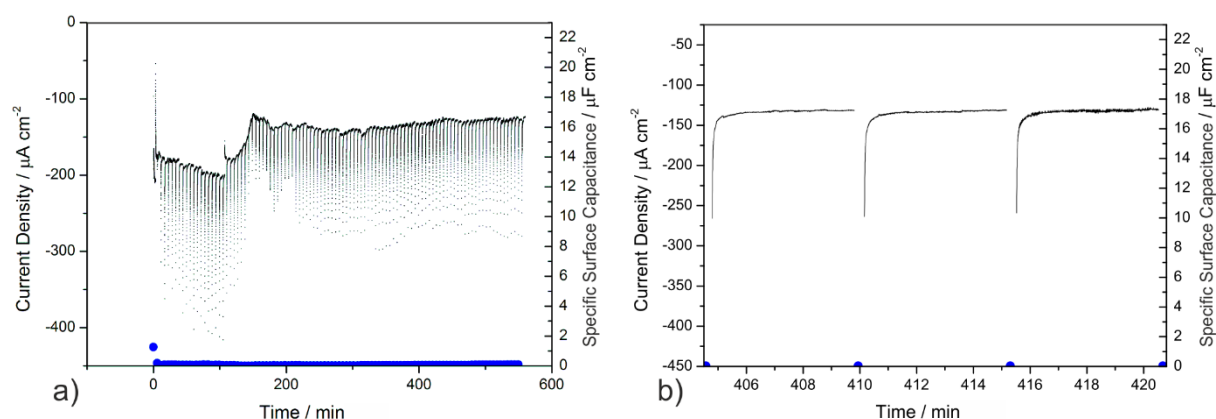


Figure 5.6 a) Graph displaying the current density (black line) and capacitance density (blue circles) for gas retention in the surface at -1.5 V vs SCE. b) The topping up process at higher resolution. Measurements of the capacitance density were taken every 5 minutes during which time hydrogen evolution stopped.

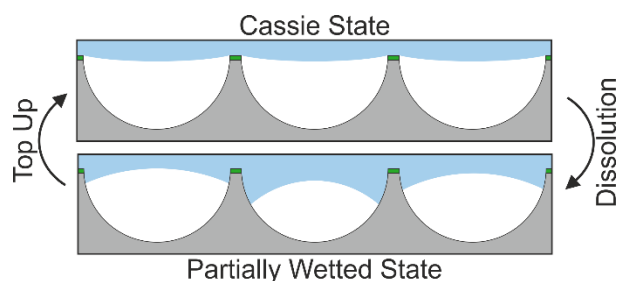


Figure 5.7 The topping up process. The surface is submerged into the water and takes the Cassie wetting state. Some of the gas dissolves and the cavities become partially wetted. As the water contacts the metal inside the cavities the electrochemical circuit closes leading the evolution of hydrogen gas which tops up the cavities until the Cassie state is regained.

To attempt to recover the Cassie state from completely wetted conditions the surface and bath were held under vacuum to remove all gas from the surface. The same potential of -1.5 V vs. SCE was then applied with capacitance measurements taken every 30 s.

Figure 5.8 a) shows the current and capacitance densities from the experiment. The specific surface capacitance starts the experiment at $\sim 20 \mu\text{F cm}^{-2}$ which shows the surface is completely wetted. After the first 30 s of hydrogen evolution there is a small decrease in capacitance density indicating that a fraction of ~ 0.1 of the surface was covered by gas however after this the specific surface capacitance does not decrease further in fact it shows a modest increase throughout the rest of the experiment. This indicates that the surface remains fully wetted despite the hydrogen evolution taking place in the metal cavities. The current density is much larger than in the previous experiment around 65 times greater due to the increased metal area exposed.

As the potential was applied bubbles of hydrogen could be observed streaming from the surface. Microscope imaging of this process was not possible as the viewing window was quickly obscured by the cloud of bubbles however figure 5.8 b) shows the surface after the process showing a large bubble (around 350 μm) in diameter present.

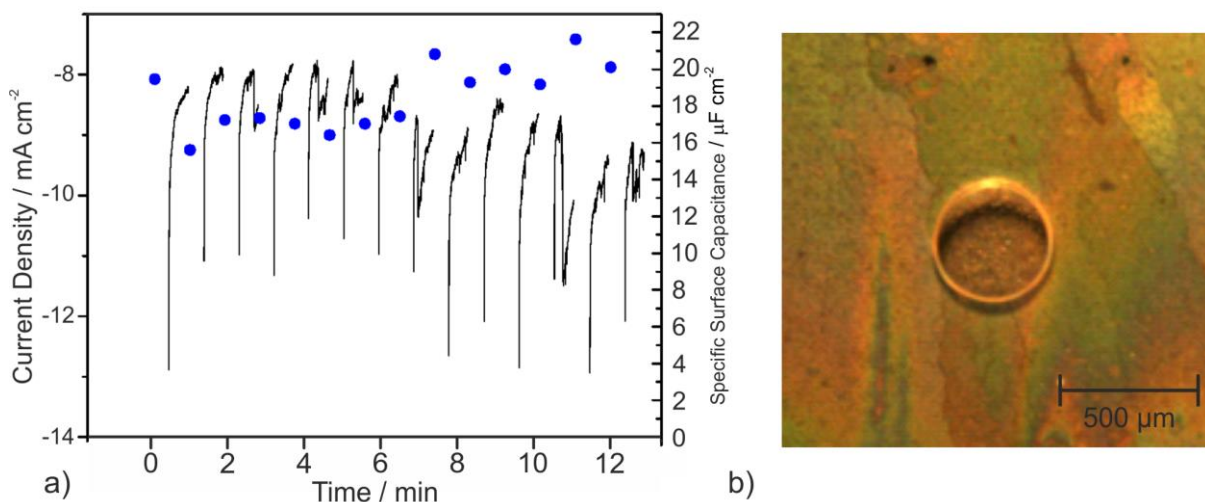


Figure 8 a) Graph showing current density and specific surface capacitance when hydrogen was evolved at -1.5 V vs. SCE in 0.1 M phosphate buffer solution after the surface had been fully wetted. b) An optical microscope image of the surface after the experiment showing the presence of large bubbles.

There seems to be a consistent theme in the response of the surface presented here and the surface of Lee and Kim.¹² When a pre-existing gas domain is present on the surface addition of more gas to this domain allows the Cassie state to be gained again successfully. However if the surface is completely wetted the nucleation of new gas does not seem to occur at the correct location for full dewetting of the surface.

The selective nucleation of electrochemically generated bubbles onto hydrophobic fluoropolymer islands on an electrode surface has been demonstrated by Brussieux *et al.*¹⁶ This was most likely due the reduced energy cost associated with displacing the liquid/solid interface with solid/gas and smaller liquid gas area of a bubble on a hydrophobic rather than a hydrophilic surface. Good control of the nucleation in active dewetting superhydrophobic surfaces will be vital to their success.

5.4 Conclusions

The work in this chapter used a surface made by templated electrodeposition of nickel around a close packed template of 3 μm spheres to a film height of 1.5 μm , a thin film of PDMS was spin coated over the surface before removal of the spheres. The resulting surface was used as the working electrode which allowed measurement of the wetted fraction of the surface and also top-up gas as it dissolved.

Dissolution of the gas within the cavities was monitored by measuring the wetted area using EIS to gain the capacitance. This demonstrated the short lifetime of the gas trapped within the cavities even when the solution was at 100% saturation. To maintain the gas filled state hydrogen was created through electrolysis of the surrounding water to replenish gas as it was lost through dissolution. Measurement of the capacitance revealed the surface was not wetted whilst hydrogen was evolved. However the inability to dewet from a completely wetted state means more work is required to enable the surface can always regain the Cassie state; this is addressed in the following Chapter.

Both measurement of the wetted area and active gas replenishment could make this surface highly effective at reducing drag for long periods where performance does not deteriorate due to loss of gas. The current size of the features, is not expected to be large enough to produce a slip length significant enough to reduce drag in large scale systems. However microfluidic and other microelectromechanical devices could experience meaningful drag reduction which would allow devices to achieve faster flow rates.

5.5 References

1. Choi, C.-H.; Kim, C.-J. Large slip of aqueous liquid flow over a nanoengineered superhydrophobic surface. *Phys. Rev. Lett.* **2006**, *96* (6), 066001.
2. Park, H.; Sun, G.; Kim, C.-J. C. In *Turbulent drag reduction on superhydrophobic surfaces confirmed by built-in shear sensing*, Micro Electro Mechanical Systems (MEMS), 2013 IEEE 26th International Conference on, 2013; IEEE, pp 1183-1186.
3. Rothstein, J. P. Slip on superhydrophobic surfaces. *Annu. Rev. Fluid. Mech.* **2010**, *42*, 89-109.
4. Lv, P.; Xue, Y.; Shi, Y.; Lin, H.; Duan, H. Metastable states and wetting transition of submerged superhydrophobic structures. *Phys. Rev. Lett.* **2014**, *112* (19), 196101.
5. Xu, M.; Sun, G.; Kim, C.-J. Infinite Lifetime of Underwater Superhydrophobic States. *Phys. Rev. Lett.* **2014**, *113* (13), 136103.
6. Govardhan, R.; Srinivas, G.; Asthana, A.; Bobji, M. Time dependence of effective slip on textured hydrophobic surfaces. *Phys. Fluids.* **2009**, *21* (5), 052001.
7. Lloyd, B. P.; Bartlett, P. N.; Wood, R. J. Wetting of Surfaces made of Hydrophobic Cavities. *Langmuir* **2015**, *31* (34), 9325-9330.
8. Bobji, M. S.; Kumar, S. V.; Asthana, A.; Govardhan, R. N. Underwater sustainability of the "Cassie" state of wetting. *Langmuir* **2009**, *25* (20), 12120-12126.

9. Poetes, R.; Holtzmann, K.; Franze, K.; Steiner, U. Metastable underwater superhydrophobicity. *Phys. Rev. Lett.* **2010**, *105* (16), 166104.
10. Tuberquia, J. C.; Song, W. S.; Jennings, G. K. Investigating the Superhydrophobic Behavior for Underwater Surfaces Using Impedance-Based Methods. *Anal. Chem.* **2011**, *83* (16), 6184-6190.
11. Dhindsa, M. S.; Smith, N. R.; Heikenfeld, J.; Rack, P. D.; Fowlkes, J. D.; Doktycz, M. J.; Melechko, A. V.; Simpson, M. L. Reversible electrowetting of vertically aligned superhydrophobic carbon nanofibers. *Langmuir* **2006**, *22* (21), 9030-9034.
12. Lee, C.; Kim, C.-J. Underwater restoration and retention of gases on superhydrophobic surfaces for drag reduction. *Phys. Rev. Lett.* **2011**, *106* (1), 014502.
13. Bartlett, P.; Baumberg, J.; Birkin, P. R.; Ghanem, M.; Netti, M. Highly ordered macroporous gold and platinum films formed by electrochemical deposition through templates assembled from submicron diameter monodisperse polystyrene spheres. *Chem. Mater.* **2002**, *14* (5), 2199-2208.
14. Trasatti, S.; Petrii, O. Real surface area measurements in electrochemistry. *Pure Appl. Chem.* **1991**, *63* (5), 711-734.
15. Orazem, M. E.; Tribollet, B. *Electrochemical impedance spectroscopy*; John Wiley & Sons, 2011.
16. Brussieux, C.; Viers, P.; Roustan, H.; Rakib, M. Controlled electrochemical gas bubble release from electrodes entirely and partially covered with hydrophobic materials. *Electrochim. Acta* **2011**, *56* (20), 7194-7201.

Chapter 6: Full Dewetting of a Cavity

The work in this chapter builds on the work in the previous chapter to allow dewetting of cavities from the fully wetted state.

6.1 Introduction

The work in chapter 5 showed that gas which has been lost through dissolution can be topped up by holding the surface at a potential which leads to the hydrogen evolution reaction and the wetted fraction can be approximated using electrochemical impedance spectroscopy (EIS). However skin friction drag reduction in real world conditions presents many difficulties; most importantly the surface must be able to deal with being submerged for long periods of time with large changes in pressure which could lead to the total loss of the gas film. The work in this chapter builds on the work in chapter 5 and the work of Lee and Kim^{1,2} to move toward making a surface capable of full dewetting. These previous efforts have found methods of topping up the gas when its volume is decreased, however regaining the low drag state after the surface has been completely wetted has not yet been achieved. Areas where improvements can be made in previous work are discussed and inform a new surface design which is modelled using a computer simulation and then fabricated and tested.

The surface described in Chapter 5 had the capability of topping up the gas within the cavities when it dissolved. However once all gas had been removed the desirable dewetted state could not be recovered and the newly generated gas left the surface as bubbles, figure 6.1. Likewise the surface of Lee and Kim was capable of topping up the gas film when the nanostructured base was kept dry however if it was wetted or the base was not nanostructured the surface would not dewet.

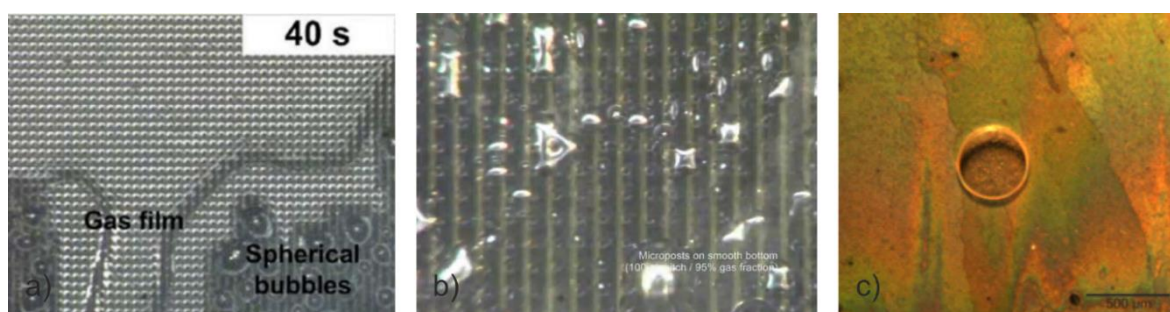


Figure 6.1 Failure to dewet after complete wetting. a) Lee and Kims post surface with nanostructured base b) Lee and Kims post surface without nanostructured base c) The surface described in chapter 5. In all cases bubbles form and leave the surface and the Cassie state cannot be recovered.

The reason for the failure of these previous surfaces to dewet themselves are because of nucleation of the gas in the wrong location or for Lee and Kim if the gas does nucleate in the correct location it cannot spread laterally through the features.

An interesting point to note about Lee and Kim's work is that their dewetting criteria predicted that a broad range of post grating type structures would allow full dewetting without the need for the nanostructured base. However results for these conditions were not presented or discussed so it seems possible that this tactic did not work. A tentative explanation is that their nanostructured base, as well as allowing lateral spreading as per their criteria, is useful for directing gas nucleation to the base of the surface.

Although both of these surfaces are much superior to passive ones with no gas replacement mechanism, they may still enter a state in which the low drag, dewetted state cannot be recovered. In realistic conditions this could occur from high transient or static water pressure, high flow rates or dissolution. In an event where the surface became fully wetted for any reason the low drag properties would be permanently effected until it was removed from the water and let to dry. Clearly this is not a feasible working model for the surface to operate under. For low drag surfaces to be a real possibility it must be demonstrated that they can fully dewet when still submerged.

The work in this chapter also considers how the slip length could be increased. As discussed in the literature review the magnitude of the slip length defines how much reduction in drag can be expected. For the surface to have a significant effect on the skin friction drag its slip length should be on the same order of length as the channel height in a Couette flow or the boundary layer. In the literature slip lengths up to $\sim 185 \mu\text{m}$ for gratings and $\sim 100 \mu\text{m}$ for posts have been presented³. These experimentally found values of slip length agree very well with the theoretical ones for the given geometry according to Ybert *et al.*⁴ For a surface constructed of gratings or holes the approximated slip length b is:

$$b \sim L \log(1 - \varphi_g) \quad (6.1)$$

Where L is the centre to centre spacing between the features and φ_g is the gas fraction of the surface.

Using eq. 6.1 the approximated slip length of the surface shown in the previous chapter is $\sim 3 \mu\text{m}$. To increase this figure the size of the hole must be increased significantly to have a meaningful impact on skin friction drag. Lee and Kim's surface for both gratings and posts had a slip length of $\sim 30 \mu\text{m}$. Maximising the slip length must be a priority for drag reducing surfaces.

Based on the previous work by Lee and Kim and my own in the previous chapter, this work aims to dewet a cavity from a fully wetted condition and also have a geometry capable of achieving a large slip length. A method by which nucleation of new gas can be directed to the desired location is discussed. The growth of a bubble within a cavity is modelled using a finite element analysis software .

6.2 Results and Discussion

The work of CJ Kim and Chapter 5 of this Thesis have concentrated on how to replenish an existing gas domain but have failed to establish an initial gas seed in the correct location from which full dewetting can be gained. With this in mind it seems appropriate that to progress further work should consider how to control nucleation to occur at the desired location in the surface. The initial gas can then be grown in much the same way as the replenishment mechanisms of the previously discussed surfaces.

Brussieux *et al.* have demonstrated that electrochemically formed hydrogen bubbles nucleate preferentially on hydrophobic surfaces⁵. In their experiment a (hydrophilic) copper electrode was patterned with hydrophobic PTFE islands. When hydrogen was evolved bubbles nucleated on the PTFE islands with such selectivity that the name of the authors' institution could be spelt out with bubbles and easily read, figure 6.2.

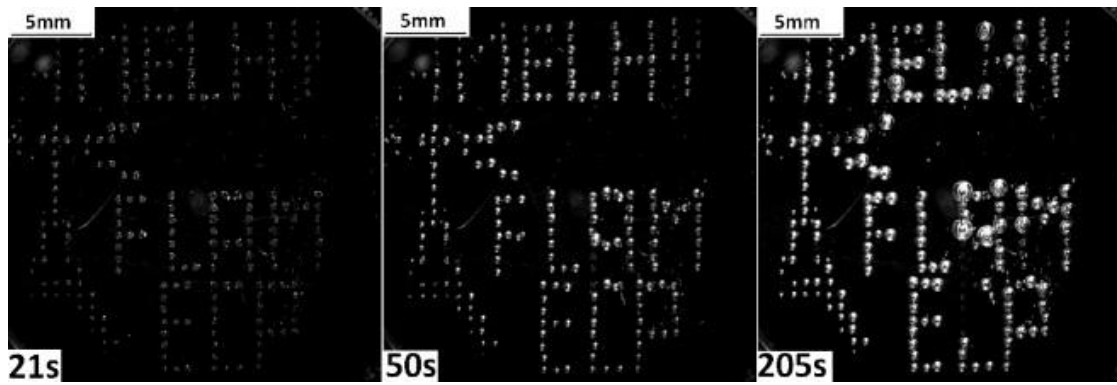


Figure 6.2 Demonstration of the preferential nucleation effect on hydrophobic surfaces by Brussieux *et al.* ⁵ Bubbles of hydrogen form on the PTFE islands which have been arranged to spell the name of the authors institution.

When the PTFE islands were < 2 mm in diameter only one large bubble nucleated on each island and detached when it approached the same diameter as the island. The reason for this preferential nucleation on the hydrophobic islands (although not discussed by Brussieux *et al.*) is probably due to the reduction in surface energy associated with the nucleation on a hydrophobic surface according to heterogeneous nucleation theory⁶.

Nucleation events are also often triggered by surface crevices or contaminants⁶. Large surface roughness is often used to promote nucleation in boiling applications however the detachment size of the bubbles using this method is normally limited to the size of the surface roughness⁷. In the surface of Lee and Kim the very rough nanostructured base was not effective at directing nucleation and is therefore discounted as a means of directing nucleation. The effect demonstrated by Brussieux *et al.*'s hydrophobic islands seems to be the strongest preferential nucleation effect with large bubble detachment size described in the literature and will be employed in this work to direct nucleation to the desired location.

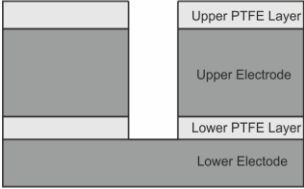
As shown in equation 6.1 both pitch and gas fraction must be maximised for the largest effective slip length, for a hole geometry this means the hole diameters must be as large with a small spacing between them. The most efficient packing of circles on a surface is hexagonal close packing which leads to a maximum gas fraction of ~ 0.9 .

Using a hole diameter of $500\text{ }\mu\text{m}$ and spacing between holes of $50\text{ }\mu\text{m}$ (pitch of $550\text{ }\mu\text{m}$) leads to a gas fraction of 75 % and using eq. 6.1 an effective slip length of $\sim 300\text{ }\mu\text{m}$, which could significantly reduce drag in large scale fluidic systems such as large pipe flows and ship boundary layers which are on the order of millimeters.

Based on the above reasoning the following general design is proposed for the surface, shown in figure 6.3. The proposed surface consists of 4 layers a lower electrode, a lower hydrophobic/insulating layer, an upper electrode and an upper hydrophobic/insulating layer.

The lower electrodes function is to evolve hydrogen gas for the initial dewetting of the bottom of the cavity. The lower hydrophobic layer acts as a nucleation site for gas generated by the lower electrode and also insulates the two electrodes from one another. The upper electrodes role is to grow the gas once it is nucleated on the lower hydrophobic layer and also to top up the cavity if gas is lost through dissolution or compressed by high water pressure. The upper hydrophobic layer insulates the top of upper electrode so gas generation ceases when the cavity is full in the same manner as the surface in the previous chapter. This layer should also be thin to minimise the distance and time for the contact line to transition to the upper electrode where the gas will be topped up. As discussed the diameter of the cavity should be around 500 μm to maximise the slip length.

It is thought that the full dewetting process will be carried out in two steps. Firstly the Lower electrode evolves hydrogen gas, dewetting the lower electrode and lower ptfe layer. This acts as a seed from which the upper electrode will continue to grow in the second step until the cavity is fully dewetted.

Feature	Function	
Lower electrode	To evolve hydrogen at the bottom of the cavity	
Lower PTFE layer	To act as a bubble nucleation site for the lower electrode and to insulate the upper and lower electrodes from one another	
Upper electrode	To generate hydrogen to fully dewet the cavity from fully wetted conditions and top it up when gas volume is lost.	
Upper PTFE layer	To insulate the top of the upper electrode	
Cavity diameter	Large to maximise slip length	

a)

b)

Figure 6.3 a) Table detailing the features included in the proposed surface and their function b) a ketch of the proposed surface design.

To investigate the feasibility of this proposed structure a computer simulation of the process was made using Comsol Multiphysics 4.4, a finite element software package, to observe the behaviour of a bubble growing in a cavity. To minimize the computational load the system was modelled in a 2d geometry.

The in-built laminar two-phase flow, phase field module of Comsol was used which solves the Cahn-Hilliard fluid model⁸. Inertial and viscous effects were neglected and the fluids were assumed to be incompressible. The model geometry is as shown in fig 6.6 c). Where the metal areas have contact angle 70° , hydrophobic areas 110° . The adhesion layer between metal and hydrophobic layer are assumed to be $10\ \mu\text{m}$ and have contact angle 40° . At this size range; less than the capillary length (which is $\sim 2\text{mm}$ for water) and low growth rates, surface tension effects dominate the behaviour.

To simulate the behaviour when dewetting the lower electrode we start with a nucleated bubble on the lower PTFE layer as the simulation of nucleation in itself is a challenging problem. Brussieux *et al.* have shown experimentally that nucleation on the PTFE layer should be expected.

The bubble is grown at a rate of $1.6 \times 10^{-9}\ \text{m}^2\text{s}^{-1}$ and stops when the lower electrode is no longer in contact with the water. Images of cross sections of the base of the cavity are shown at 10 second intervals in figure 4 where blue represents gas and red represents water.

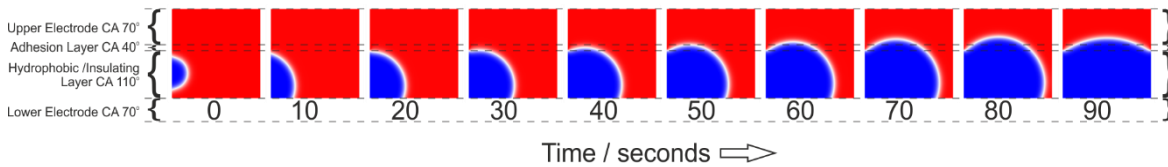


Figure 6.4 sequence of bubble growth in the bottom of the cavity. Gas is shown in blue and liquid in red. The layers are divided by the dashed lines and labelled on the left. The time is shown in seconds underneath each image.

The simulation shows a full dewetting of the lower electrode for the given geometry. Initially the bubble expands to touch the lower electrode (10 s). The contact line moves upwards and is pinned on the junction between the hydrophobic and adhesion layer which prevents further vertical movement (20 s). The contact line continues to move across the lower electrode (30 – 80 s) until it reaches the other side of the cavity and quickly moves up the hydrophobic layer to fully insulate the lower electrode.

The upper electrode dewetting continues from the final point of the lower electrode dewetting at the same rate of gas growth, figure 6.5. The gas continues to rise up the cavity until it reaches the upper PTFE layer where the electrode is no longer contacting the water and the contact line is at the top of the cavity.

This short computer simulation of the system shows that the proposed mechanism of dewetting should work once a bubble has nucleated on the lower hydrophobic layer and gas should not be lost as discrete bubbles.

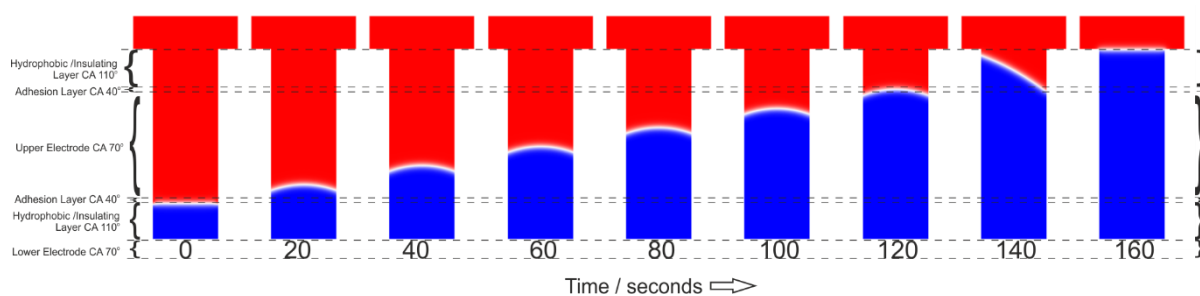


Figure 6.5 Dewetting the upper portion of the cavity

The Cahn-Hilliard fluid model is commonly used and accepted model. The contact angles on the walls are as defined and the interface has constant curvature, as should be the case at scales less than the capillary length (~ 2 mm for water). The behaviour of the system can also be explained using the Young equation. There are limitations of this model. Most importantly the model only considers a 2d geometry and only one bubble is nucleated whereas in reality there could be several growing at the same time.

To study the behaviour of the surface design experimentally individual cavities are considered. This has the benefit of being able to directly correlate visual and electrochemical data throughout the dewetting process.

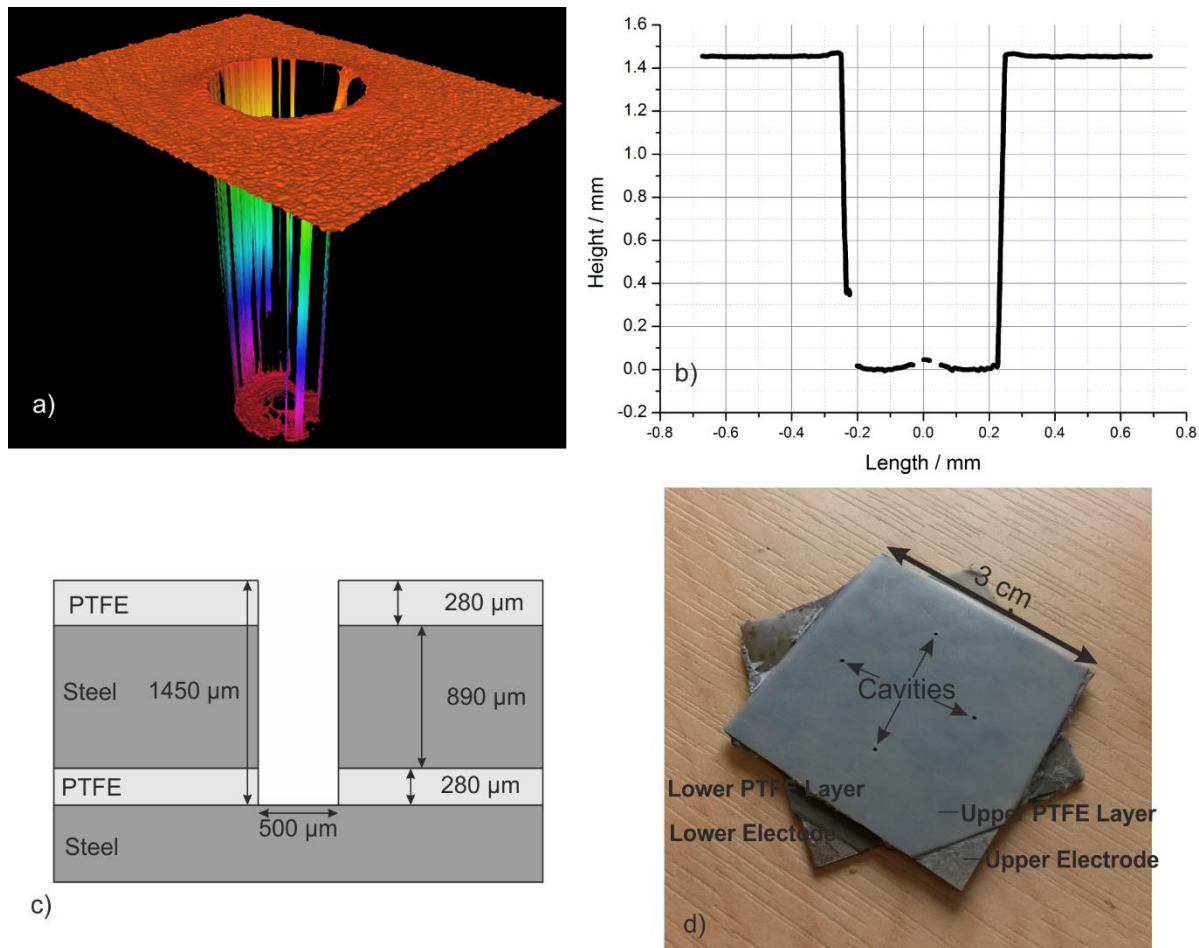


Figure 6.6 a) Image of the cavity using a 3d optical microscope b) Cross section measured through the centre of the cavity c) Dimensions of layers within the cavity d) Photograph of the sample used in the experiments.

To observe the behaviour within single cavities a sample was fabricated to the dimensions shown in figure 6.6, c). 316 stainless steel sheet from RS Components was used for the electrode surfaces; it was chosen for its corrosion resistance, relatively low cost and minimal burring when machined. PTFE film was used for the hydrophobic / electrically insulating layers from Fluorocarbon Company Ltd. which has a contact angle of 115° and is easily machinable (PDMS was used initially but had poor machining characteristics)

The steel and PTFE were cut to squares of 3 x 3 cm. One corner of each of the PDMS layers was removed so to expose the stainless steel so it could later be attached by a crocodile clip figure 6 d). The PTFE and steel were glued using epoxy resin (Hysol 9461 by Loctite). To promote strong adhesion between the layers the steel surface was roughened by grinding with 25 μm diamond solution on a Kermet 15 lapping machine. The PTFE was etched on sides which required gluing (so the top of the upper layer remained unetched). The layers were rinsed with acetone, dried then assembled and clamped together to push out excess epoxy resin and hold the construction

together. The epoxy was left to cure in an oven at $\sim 80^{\circ}\text{C}$ for a day. The adhesion between the layers was very strong when assembled in this way and could not be delaminated by hand.

The cavity was made by using a $500\ \mu\text{m}$ diameter square ended router bit at 8000 RPM spindle speed. The vertical displacement of the routing machine was zeroed to the lower electrode, so the depth of the hole just exposes the lower electrode.

Figure 6.7 shows the experimental setup. A small Teflon disk with a glass cover slip on top allowed a microscope to image the cavity directly throughout the experiment whilst the dewetting process was happening.

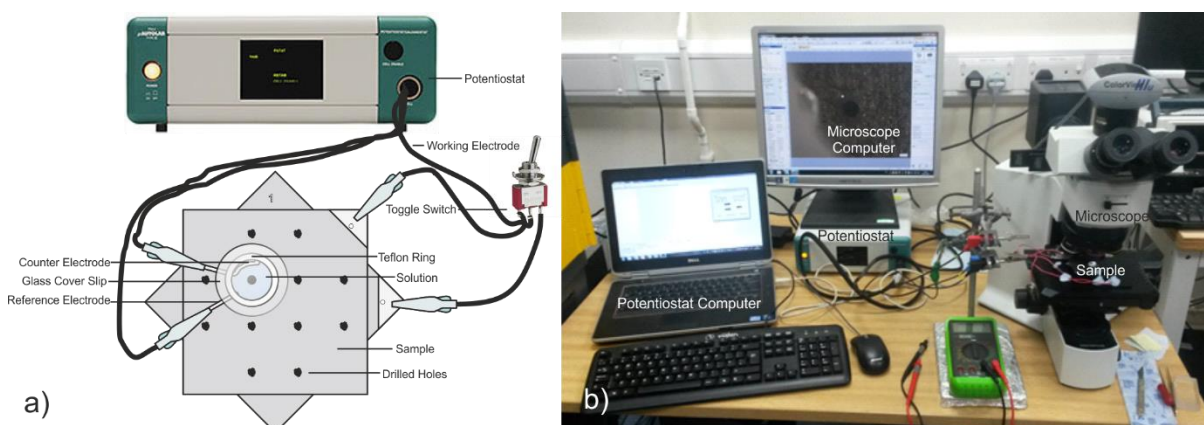


Figure 6.7 a) Schematic of the electrochemical set up b) Full experimental set up

The electrochemical cell was a Teflon ring (8 mm internal diameter by 2.5 mm tall, total volume 0.126 mL) Holes were drilled through the side through which the reference and counter electrodes could pass. The counter electrode was a platinum wire with area $1 \times 10^{-4}\ \text{cm}^2$, which is always > 10 times the working electrode area. Due to the small size of the cell a platinum wire was used as a pseudo-reference electrode against which the potential could be measured. The working electrode was connected to a 3-way switch so the upper or lower electrode could be selected independently of one another. The solution was an aqueous 0.1 M Phosphate buffer at pH 7.

The cell was placed over the desired cavity on the sample and held in place with blu-tack. The solution was pipetted into the cell and a cover slip placed on top of the cell to increase the quality of the microscope image by reducing distortion from the meniscus curvature. As both cell and surface are hydrophobic the solution did not leak out. To fully wet the cavity the sample and cell were placed inside a desiccator which was then subjected to a modest vacuum for a period of

Chapter 6

roughly 3 minutes. EIS measurements were used in the same manner as presented in chapter 5 to determine the wetted area throughout the dewetting process.

Experimental procedure was as follows:

1. Fill bath with solution and put on cover slip
2. Image and take capacitance measurement
3. Remove coverslip and place sample and bath into vacuum desiccator for ~3 minutes to remove bubble from cavity
4. Top up solution if necessary and reapply cover slip
5. View under microscope to confirm bubble is fully dissolved if not repeat steps 3. and 4.
6. Image and capacitance measurement
7. Turn on lower electrode, measure current, take video with microscope
8. When finished capacitance measurement
9. Turn on upper electrode, measure current, take video with microscope
10. When finished capacitance measurement

6.2.1 Dewetting

The full dewetting of the cavity was undertaken in two steps; firstly the lower dewetting using the lower electrode to nucleate a bubble to fill to bottom of the cavity and secondly the upper dewetting to grow the gas volume to dewet the rest of the cavity. To evolve hydrogen gas the potential was held at -1.5 V against the platinum wire pseudo-reference electrode. A typical example of the full dewetting process is shown, and the process is highly repeatable.

6.2.2 Lower Dewetting

Dewetting of the lower electrode follows the following mechanism after the potential is set to -1.5 V : Figure 6.8 shows chronoamperometry and microscope images of the dewetting of the lower electrode. The microscope is focused on the bottom of the cavity.

0 - 50 seconds

Initially bubbles nucleate on both the PTFE and metal surfaces up to ~50 seconds. Note the current increase and decrease at ~ 40 seconds is the detachment of the bubble in the centre of the cavity on the metal surface.

50 – 125 seconds

Bubbles nucleated on the metal surface either detach and rise out of the cavity or coalesce with a bubble on PTFE sidewall. Any bubbles nucleated on the PTFE side wall did not detach and grew until they coalesced into one bubble.

125 – 250 seconds

The single bubble continues to grow as gas diffuses into it and seems to behave similarly to the computer simulation from this point.

250 seconds

The bubble grows to a size where it fully insulates the lower electrode and the current goes to zero.

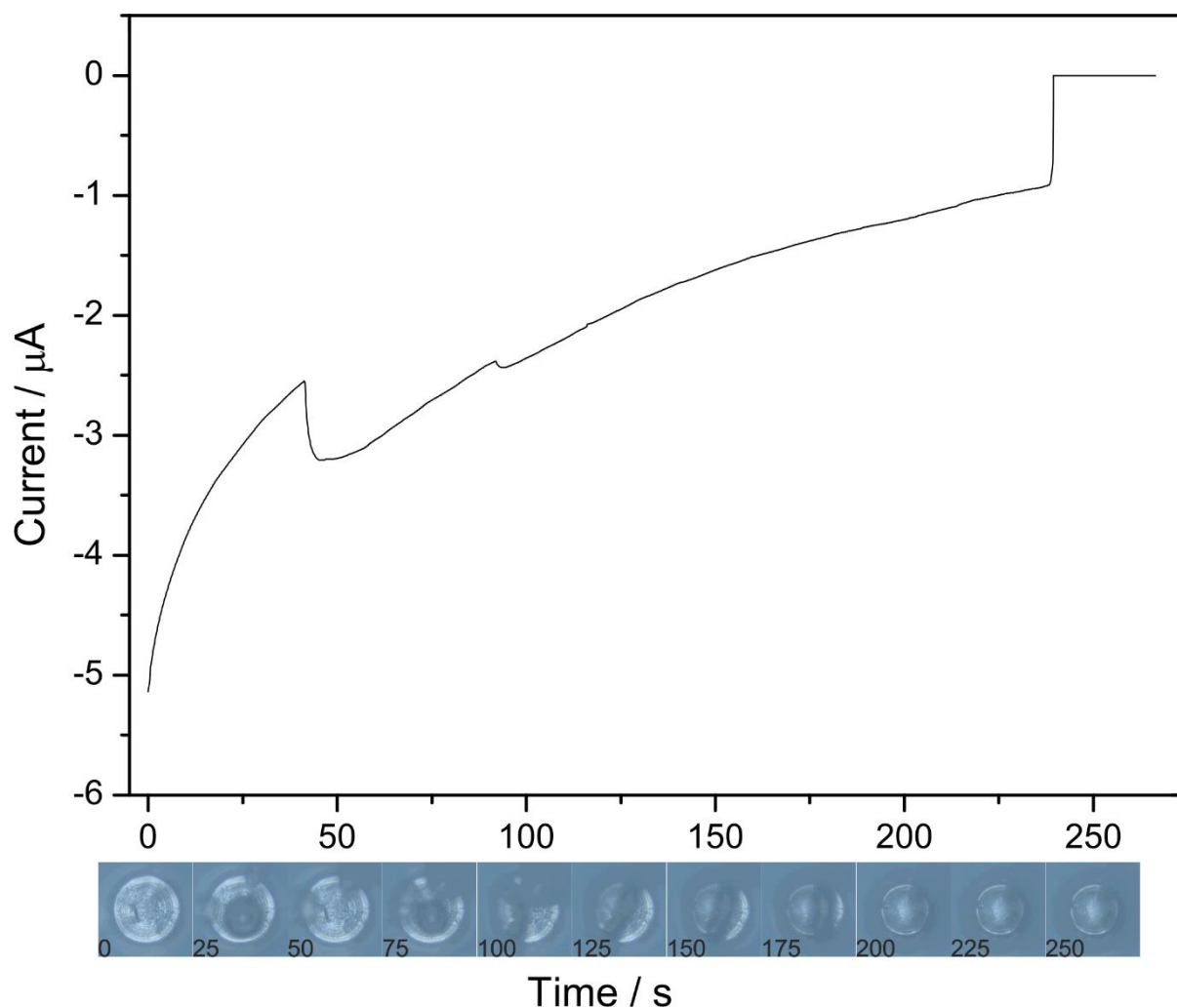


Figure 6.8 Graph showing the chronoamperometry for the lower dewetting with microscope images below.

6.2.3 Upper Dewetting

The depth of field is not great enough to capture the full length of the upper electrode and upper PTFE layer so the microscope is focused on the top of the PTFE layer. It is not possible to see the bubble nucleated from the lower dewetting process so visual information of this process is more limited than the lower dewetting.

When the upper electrode potential is set to -1.5 V nucleation of bubbles occurs in the rim of the upper PTFE layer, figure 6.9. Some of these bubbles detach and some remain attached and coalesce to form larger bubbles. Due to the poor depth of field and bubbles on the PTFE rim the view into the cavity is obscured. However from the current data it can be seen that hydrogen gas continues to be produced until the bubble grows to a size which insulates the upper electrode and the current goes to zero again.

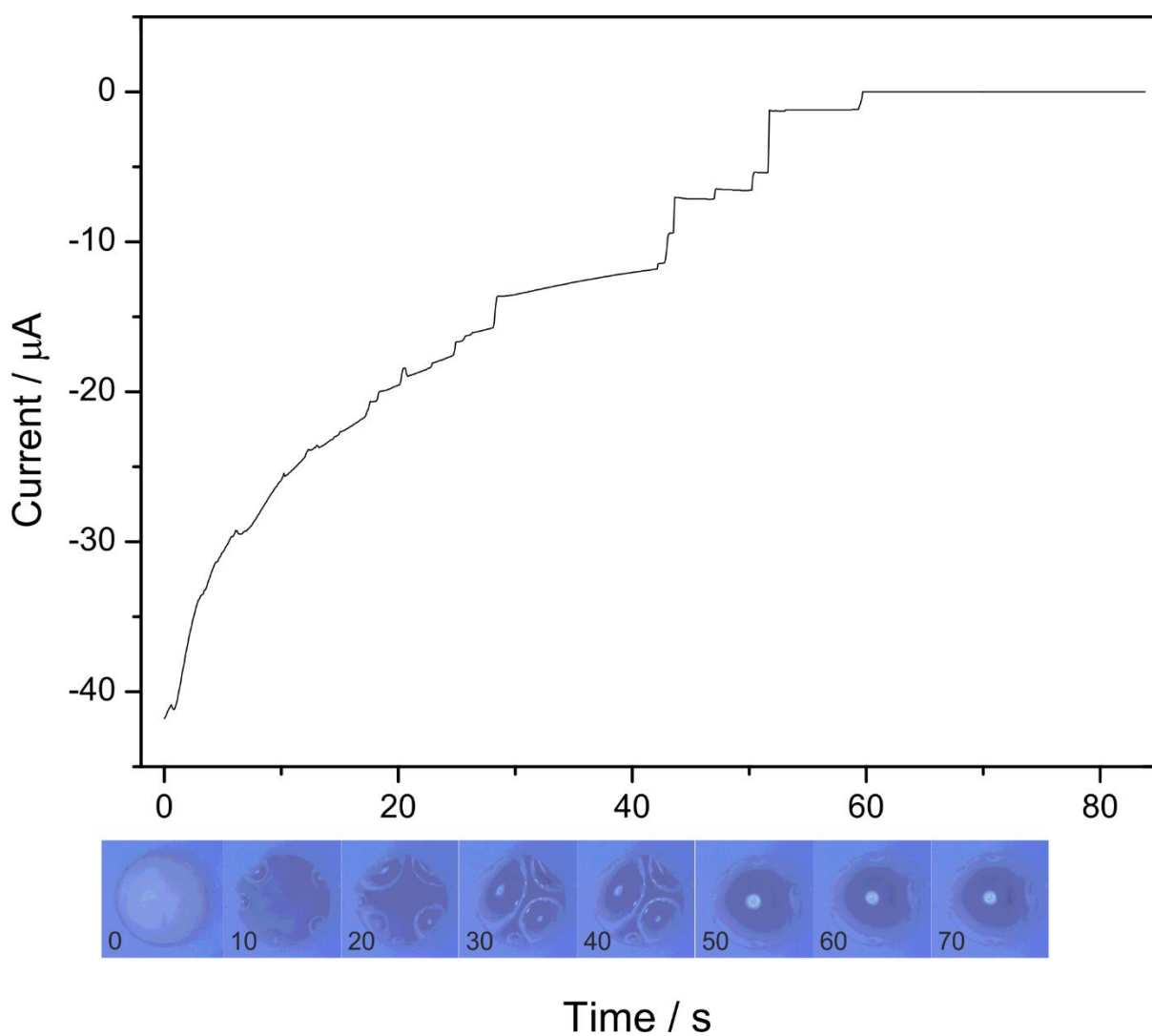


Figure 6.9 Graph showing the chronoamperometry for the upper dewetting with microscope images below.

In tests where only the top electrode was allowed to evolve hydrogen it was seen that bubbles nucleating and coalescing on the rim sometimes led to the insulation of the cavity, however was not as reliable as the lower then upper dewetting method, which did not fail in any test.

6.2.4 Measurement of Wetted Area

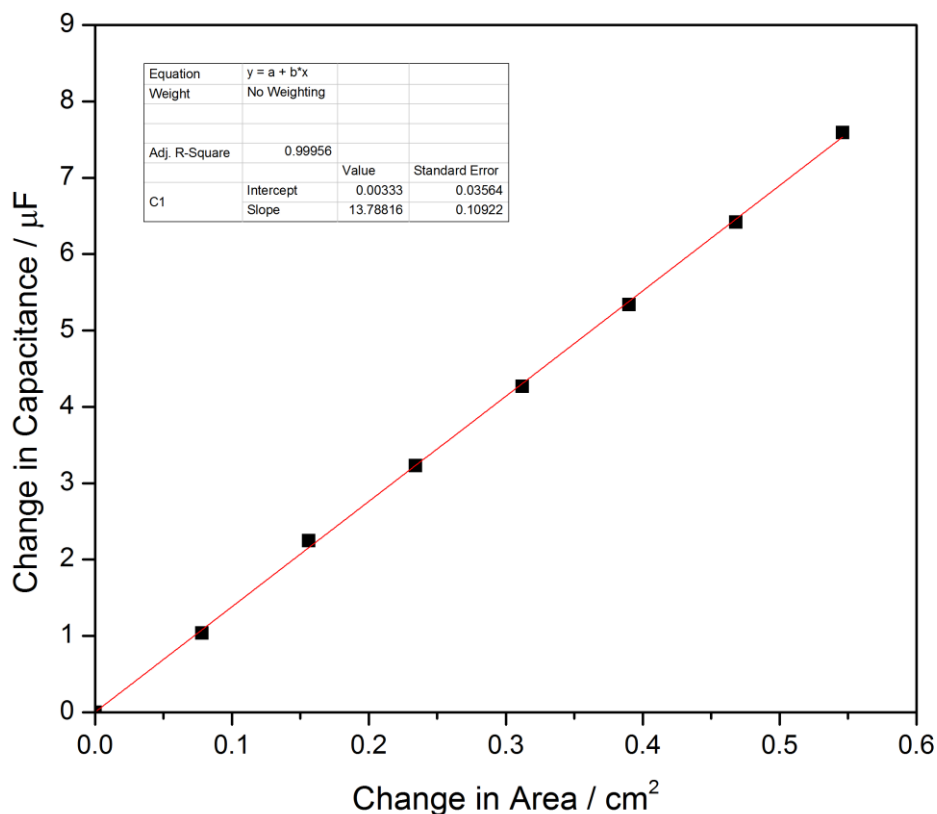


Figure 6.10 Graph showing a linear relationship between capacitance and area. The gradient give a specific capacitance of $13.8 \mu\text{F cm}^{-2}$.

The same EIS based measurement of the double layer capacitance as presented in chapter 5. As before using a flat electrode, a linear relationship is shown between the change in capacitance with electrode area figure 6.10, where the gradient shows the specific capacitance is $13.8 \mu\text{F cm}^{-2}$. This shows that this is a reliable measure of wetted electrode area.

Figure 6.11 shows the capacitance for both the upper and lower electrodes throughout the dewetting experiment. When the sample is dry in air and submerged in water but the bubble is present the capacitance = 0 nF for both electrodes. When fully wetted the lower electrode has a capacitance of 38 nF and the upper 197 nF. After the lower electrode has been dewetted its capacitance returned to 0 nF. The upper electrode's capacitance increases to 217 nF due to the local changes in solution composition due to the hydrogen production from the lower electrode. After the upper electrode has been dewetted its' capacitance returns to 0 nF.

Measuring the capacitance with EIS also has great potential to quantify the dissolution of the gas as shown in the previous chapter.

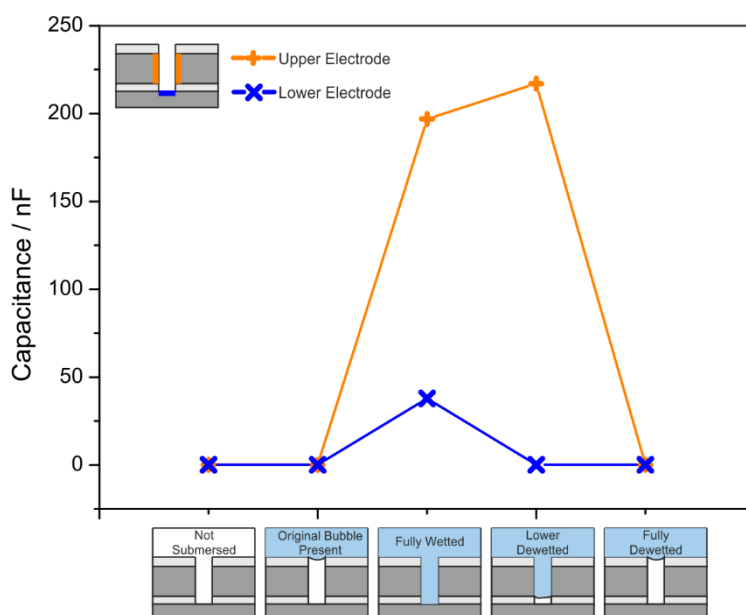


Figure 6.11 Graph showing the capacitance for the different states encountered throughout the dewetting experiment in chronological order.

6.2.5 Loss of Gas Volume

The capability of the system to top itself up after the loss of gas is also demonstrated. In real world scenarios this could be due to dissolution or an increase in pressure both leading to a loss in gas volume.

To simulate loss of gas volume without the need for specialist equipment (ie. high pressure cell) the gas was displaced mechanically by inserting a probe into the cavity to reduce the volume of gas. The probe was a 400 μm diameter plastic cylinder with a 'stopper' at a length of 1 mm along the needle. When inserted into the cavity a volume of $\sim 1 \times 10^{-10} \text{ m}^3$ was displaced from the cavity roughly a quarter of the cavity volume which left as a bubble. The imaging of this process was hindered by the need for access of the probe to the cavity which also meant the cover slip could not be applied to the cell to reduce image distortion.

Before gas was removed the upper electrode was held at a potential of either -1.5 or -5 vs Pt reference. Figure 6.12 shows plots of current against time from before the probe was inserted until when the gas had been recovered.

Chapter 6

When the upper electrode is held at -1.5 V the process is fairly slow, taking around 5 minutes to fully recover. To speed this process up the voltage was increased to -5 V, here the process completes in only 15 seconds.

In both cases there is a small leakage current, which implies that there is small bit of metal still exposed to the water, this was verified with capacitance measurements which were on the order of 1 nF.

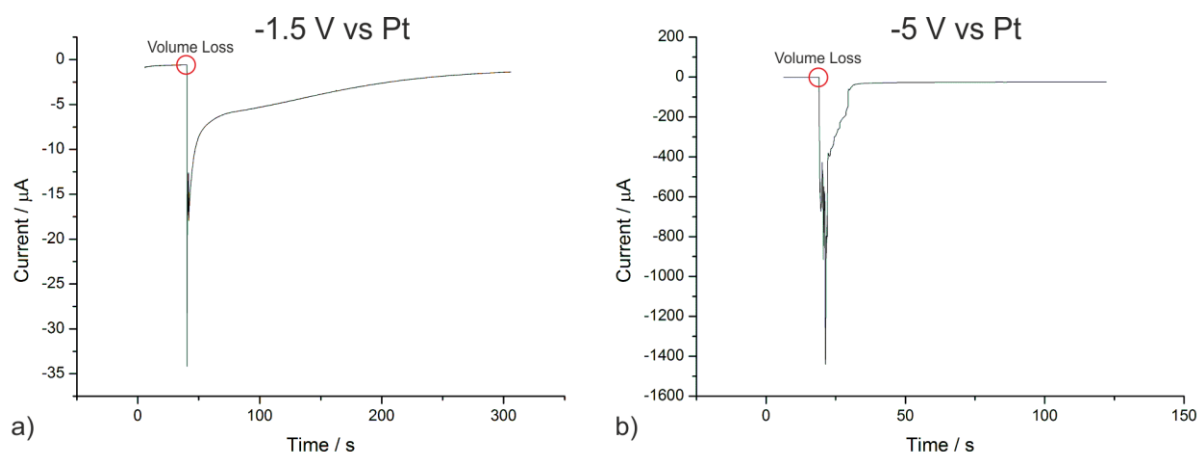


Figure 6.12 Graphs showing top up of the cavity whilst the upper electrode is held at a) -1.5 and b) -5 V vs a platinum wire reference.

6.3 Conclusion

This chapter has presented a design of a cavity which can regain the Cassie state from fully wetted conditions. The use of a hydrophobic surface to direct nucleation of gas bubbles to the desired location from which the gas could grow and dewet the cavity has been shown to be a successful tactic. This has improved on previous surfaces where some gas must remain if dewetting is to be successful.

The measurement of wetted area using capacitance measurement developed in chapter 5 has proven to be useful in this work and should be used to measure the rate of dissolution of the gas from these cavities to repeat the work of Lv *et al.*⁹. When gas was lost from the cavity it was topped up again in a short space of time.

This development has great potential to reduce drag in real world scenarios. However first the cavities must be tested in a close packed array with small spacing between cavities. If the 500 μm cavities were arranged in a close packed array with 50 μm gap between cavities the slip length would be approximately 300 μm , large enough to make substantial drag reductions in large scale fluidic systems such as ships and water pipes.

6.4 References

1. Lee, C.; Kim, C.-J. Underwater restoration and retention of gases on superhydrophobic surfaces for drag reduction. *Phys. Rev. Lett.* **2011**, *106* (1), 014502.
2. Lee, C.; Kim, C.-J. Wetting and Active Dewetting Processes of Hierarchically Constructed Superhydrophobic Surfaces Fully Immersed in Water. *Journal of Microelectromechanical Systems* **2012**, *21* (3), 712-720.
3. Lee, C.; Choi, C.-H.; Kim, C.-J. C. Structured surfaces for a giant liquid slip. *Phys. Rev. Lett.* **2008**, *101* (6), 064501.
4. Ybert, C.; Barentin, C.; Cottin-Bizonne, C.; Joseph, P.; Bocquet, L. Achieving large slip with superhydrophobic surfaces: Scaling laws for generic geometries. *Phys. Fluids* **2007**, *19*, 123601.
5. Brussieux, C.; Viers, P.; Roustan, H.; Rakib, M. Controlled electrochemical gas bubble release from electrodes entirely and partially covered with hydrophobic materials. *Electrochim. Acta* **2011**, *56* (20), 7194-7201.
6. Debenedetti, P. G. *Metastable liquids: concepts and principles*; Princeton University Press 1996.
7. McHale, J. P.; Garimella, S. V. Nucleate boiling from smooth and rough surfaces—Part 1: Fabrication and characterization of an optically transparent heater–sensor substrate with controlled surface roughness. *Exp. Therm Fluid Sci.* **2013**, *44*, 456-467.
8. Cahn, J. W.; Hilliard, J. E. Free energy of a nonuniform system. I. Interfacial free energy. *The Journal of chemical physics* **1958**, *28* (2), 258-267.
9. Lv, P.; Xue, Y.; Shi, Y.; Lin, H.; Duan, H. Metastable states and wetting transition of submerged superhydrophobic structures. *Phys. Rev. Lett.* **2014**, *112* (19), 196101.

Chapter 7: Control of Nanobubble Size, Shape and Location by Sub-Micron Cavity Structures

The work in this chapter uses atomic force microscopy to investigate the nano-scale wetting of surfaces prepared by templated electrodeposition of gold around 600 nm spheres which is modified with a hydrophobic self assembled monolayer. Images of the surfaces submerged in water reveal the presence of nanobubbles within the cavities. which in some cases have surprisingly strong negative curvature. Increased ease of nucleation and resistance to coalescence are also observed.

7.1 Introduction

Recently, surface nanobubbles less than 100 nm in height and up to 1 μm in diameter have been observed on flat solid surfaces by a variety of techniques.^{1,2} The long life-time of these nanobubbles does not agree with classical thermodynamic theory.³ The mechanism by which nanobubbles are stabilised has been considered by several authors; however the situation still remains unclear. It is evident that there are significant differences between nano and macro scale wetting phenomena present here. The contact angle of nanobubbles is much larger than in the macroscopic case, and is dependent on the nanobubble size rather than the surface chemistry of the substrate they sit on. Nanobubbles can alter macroscopic behaviour and have been shown to affect adhesion of wetted hydrophobic surfaces⁴, cleaning processes⁵, emulsion stability⁶, and interfacial friction⁷.

Several studies have implied that nanoscale gaseous domains have been trapped within surface structures, however they were not considered within the scope of 'nanobubbles' at the time^{8,9}. More recently the behaviour of nanobubbles restrained in hydrophobic surface structures has been examined^{10,11,12}. Two general substrate types have been used: a hydrophilic surface patterned with a hydrophobic substance to direct nucleation to these points and a patterned hydrophobic surface with a desired topography, within which the nanobubbles lie. Wang *et al.*¹² and Agrawal *et al.*¹⁰ demonstrated that the location of nanobubbles on a surface could be controlled by partially coating a hydrophilic surface with submicron hydrophobic islands. Nanobubbles only formed on the hydrophobic regions, although often more than one bubble could be found on each island. Wang *et al.* used the formation of nanobubbles on a thin spin-coated polystyrene film to structure the

surface¹³. A slight rising of the polystyrene film around the three phase contact line occurred due to the interfacial force balance perpendicular to the solid phase.

Nanobubbles have been detected inside parabolic cavity structures, made by a block copolymer self-assembly process, using small-angle X-ray scattering to measure the amount of trapped gas by Checco *et al.*¹¹. However, Agrawal *et al.* were unsuccessful in using tapping-mode atomic force microscopy (AFM) to detect nanobubbles in a very similar surface made in the same way¹⁰. Difficulties in obtaining AFM images of nanobubbles here are to be expected. The calculations of gas volume of Checco *et al.* implied the nanobubbles had receded some distance into the cavities; at this point the size of the tip may limit nanobubble detection and may be the reason Agrawal *et al.* did not observe nanobubbles.

The parabolic cavity structures made by Agrawal *et al.* had widths between 14 and 16 nm and were 30 nm deep. Checco *et al.* had a fixed width of 28 nm and the depth varied by the etch time from 20 to 160 nm. Both surfaces had narrow, high-aspect ratio cavities which are quite different to the dimensions of nanobubbles native to planar hydrophobic surfaces which have very low aspect ratios – typically 5 – 100 nm high and 100 – 800 nm in diameter.

The formation of bubbles within sub-micron surface structures has potential to control several important parameters for maximising slip. Height and diameter are the obvious parameters that define the bubble, from which radius of curvature, contact angle and pressure can be evaluated. In the case of reducing drag in micro / nano fluidics, maintaining a high coverage of bubbles is desirable; nanostructured surfaces have the capacity to reduce bubble mobility for this application since a larger force is required to initiate bubble movement as the effective contact angle hysteresis becomes amplified by the structure¹². An important issue regarding slip on nanobubble covered surfaces is the degree to which the bubbles protrude into the fluid. Maximum effective slips are expected to occur when the gas – liquid interface is flush to the surface and can be severely decreased when the interface has large curvature¹⁴. Nanobubbles on flat surfaces have been shown to be very mobile and to coalesce easily – reducing fractional area coverage, which again reduces effective slip. Bhushan *et al.* showed that by using a featured surface the nanobubbles resisted movement better, which prevented coalescence¹³. If the nanobubbles recede a small amount into the cavities or the interface has a negative curvature it is conceivable that another surface (such as in a bearing) could touch the surface without disturbing the bubbles.

In the work in this Chapter hexagonally close-packed spherical cavities with a 300 nm radius of curvature are used to systematically explore nanoscopic wetting phenomena of a range of structures by using tapping-mode AFM. The use of AFM allows much needed topological information about the way the nanobubbles occupy the cavities. Increased stability to coalescence and

increased nucleation phase space are also observed. Other potential benefits of confining nanobubbles to cavities are also discussed.

7.2 Experimental

Structured surfaces were fabricated by templated electrodeposition following the technique used by Bartlett *et al.*¹⁵ as discussed in Chapter 3. 600 nm polystyrene latex spheres were used as the template on a gold coated slide. Gold was electroplated at five heights: 0.1, 0.2, 0.3, 0.4, and 0.5 d (figure 7.1) where d is the dimensionless film height; the electroplated film height divided by sphere diameter (ie. 0.5 d = 300 nm film height). The polystyrene-latex template was removed by dissolving in tetrahydrofuran, leaving the inverse gold cavity structure. To reduce the surface energy of the gold a self-assembled monolayer of 1-dodecanethiol was formed by soaking in a 10 mM solution in ethanol for 12 hours. The contact angle of an unstructured gold surface treated in this way is 112°. Areas of around 1 cm² can easily be prepared in this way. Figure 1 a) shows the five deposition heights about the sphere and b) shows scanning electron microscopy images of these surfaces.

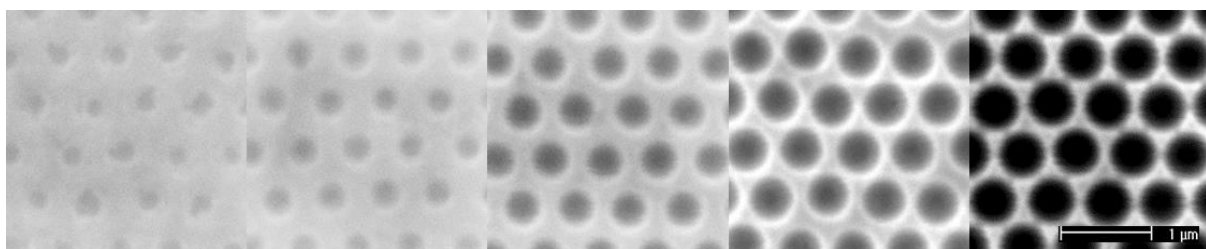


Figure 7.1 Scanning electron microscope images of close packed gold cavity structures from 0.1 to 0.5 d prepared by templated electrodeposition around polystyrene spheres.

The method used gives excellent control over the surface where the sphere size, d value and thiol modification can be adjusted as required, giving rise to a broad range of surfaces not accessible with lithographic methods. By changing the d value, a few key parameters are adjusted which are of importance to the wetting properties of the surface: the area coverage, aspect ratio, side wall angle, and resulting cavity mouth radius.

Advancing contact angle measurements were taken on the fabricated surfaces using a Krüss DSA 100 with 1 μ l drops of water. The observed advancing contact angles, θ_{adv}^* , agree with the Cassie-Baxter model of wetting¹⁶ (equation 7.1) where θ_{adv} is the contact angle on a flat surface. The solid fraction, Φ_s , of the surface is related to d by equation 7.2 assuming the fractional area of the surface

covered with cavities is gas filled. This agrees with the more in depth study using a larger 3 μm sphere template in Chapter 4.

$$\cos\theta_{\text{adv}}^* = \Phi_s \cos\theta_{\text{adv}} - (1 - \Phi_s) \quad (7.1)$$

$$\Phi_s = 1 - \left(\frac{\pi}{2\sqrt{3}}\right) (1 - (1 - 2d)^2) \quad (7.2)$$

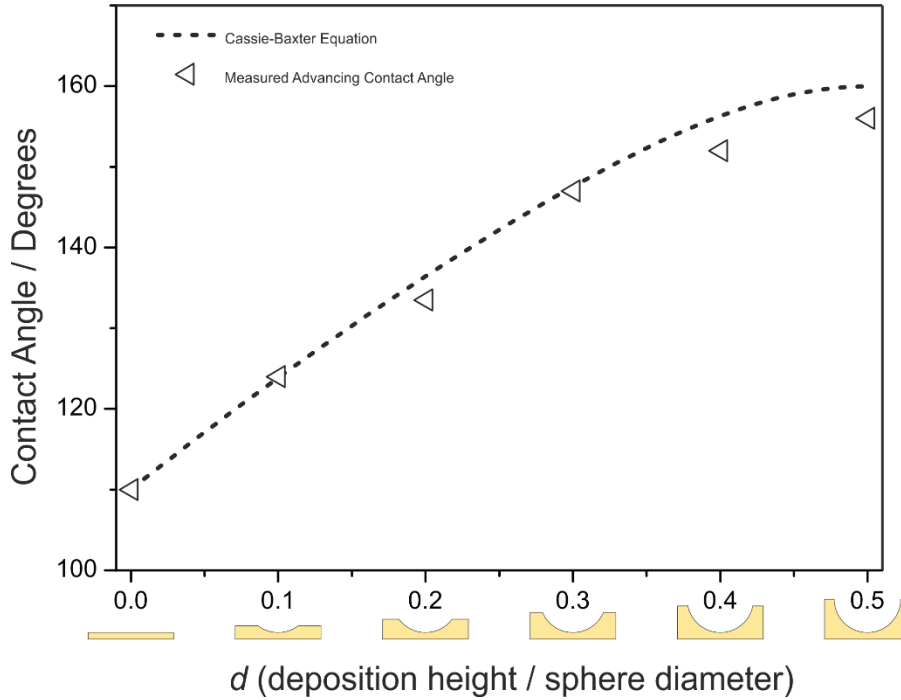


Figure 7.2 The experimentally found contact angle (blue triangles) of 1 μl drops of water as a function of the dimensionless film height d . The Cassie-Baxter equation (green line) is also plotted as a function of d assuming the cavities are gas filled and the solid contact angle to be 110° .

Atomic force microscopy was used which allowed for a detailed insight into the nature of the wetting of the surface structures. The MFP-3D atomic force microscope (Asylum Research, UK) was used in both tapping and contact mode with pyrex nitride 'PNP-TR' AFM probes (Nanoworld, Cz) with pyramidal tips, radius of curvature $< 10\text{ nm}$ and half-cone angle of 35° . The spring constant of the cantilever was 0.32 N/m . In tapping mode the cantilever was driven at a free amplitude (A_o) of 11.16 nm and the set point amplitude (A_s) during imaging was 5.76 nm which gives a setpoint ratio (A_o / A_s) of 0.5 .

Images of dry surfaces were taken with tapping mode. Images of all the wetted surfaces were made by using ultra-pure Millipore ($18\text{ M}\Omega\text{ cm}$) water which had been allowed to equilibrate with the air giving a 100% gas saturation in an AFM wet cell also in attractive tapping mode. The water was injected into the cell, covering the surface with $\sim 2\text{ mm}$ of water and no solvent exchange was performed (Figure 7.3). The choice of attractive mode imaging was informed by approach curves showing the interaction between the tip and substrate was indeed attractive (supplementary info).

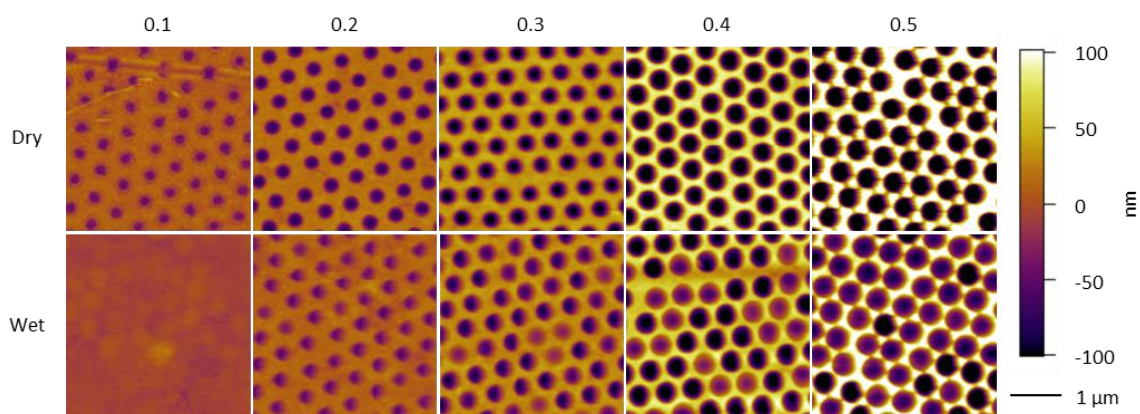


Figure 7.3 Tapping-mode atomic force microscopy (using pyrex nitride tip and setpoint ratio of 0.5) height images of 0.1 – 0.5 d substrates made by templated electrodeposition of gold around 600 nm polystyrene spheres. The top row is in dry conditions, the bottom in wetted, showing the presence of nanobubbles within the cavities. *nb. The scale bar shows a height of 200 nm which is less than the height of the 0.4 and 0.5 d structures but is used to allow resolution of the total d value range with one scale bar.*

Figure 7.3 shows the tapping mode images obtained for the range of d substrates in both dry and water submerged conditions. A change in colour (and hence z axis height) is noticeable within the cavities between the wetted and dry conditions showing that bubbles have formed preferentially within the cavities when submerged in water. For example in the 0.5 d black cavities from the dry image look purple when a bubble is present when the surface is wetted. The height images show a full coverage of bubbles in the 0.1 to 0.3 d and a partial coverage in the 0.4 and 0.5 d . The surface structure leads to the formation of bubbles of uniform diameter and the bubbles fill the cavities however the 0.3 d shows some small variation in size. The colour, indicating height in the images shows that the 0.1 d leads to flat or slightly protruding bubbles when wetted. However the 0.2 – 0.5 d lead to nanobubbles which are recessed, lower than the tops of the cavities. From figure 3 it is clear that it is possible to get a good coverage of bubbles using a structured surface without the need of an ethanol/water solvent exchange to super-saturate the solution as used by other groups.

To further understand the interaction between bubble and cavity, 2 dimensional profiles of the cavity and cavity containing nanobubble were aligned and overlaid onto one another. It is clear that an imaging artefact is present in the images on the right side of the bubbles and cavities due to the edge of the tip touching the rim of the cavity which becomes more pronounced with the deeper cavities. Spherical caps were fitted to align with the data points on the left side of the measured

cavity and bubble profiles. The nanobubble profiles from each cavity size are representative of the population.

From these plots several bubble parameters were measured: nanobubble height (h_b), nanobubble radius (w_b), nanobubble contact angle (ϑ_b), nanobubble radius of curvature (r_b) and height of the three phase contact line inside the cavity side wall (d_b) - expressed as a d -value (Figure 7.5). These values are taken from the fitted profiles rather than the measured data points as the fitted profiles rely on all of the measured data points and so are likely to have a lower associated error but assume a spherical shape for the interface.

The axes of the graphs below are adjusted to be 1:1 to show the true cross section, going through the centre of the nanobubble and cavity. The yellow fitted curve for the cavity is always part of a 300 nm radius circle which was adjusted to overlap the data points. The blue coloured curve is part of a circle whose radius has been adjusted to fit the bubble curvature as closely as possible (Figure 7.4).

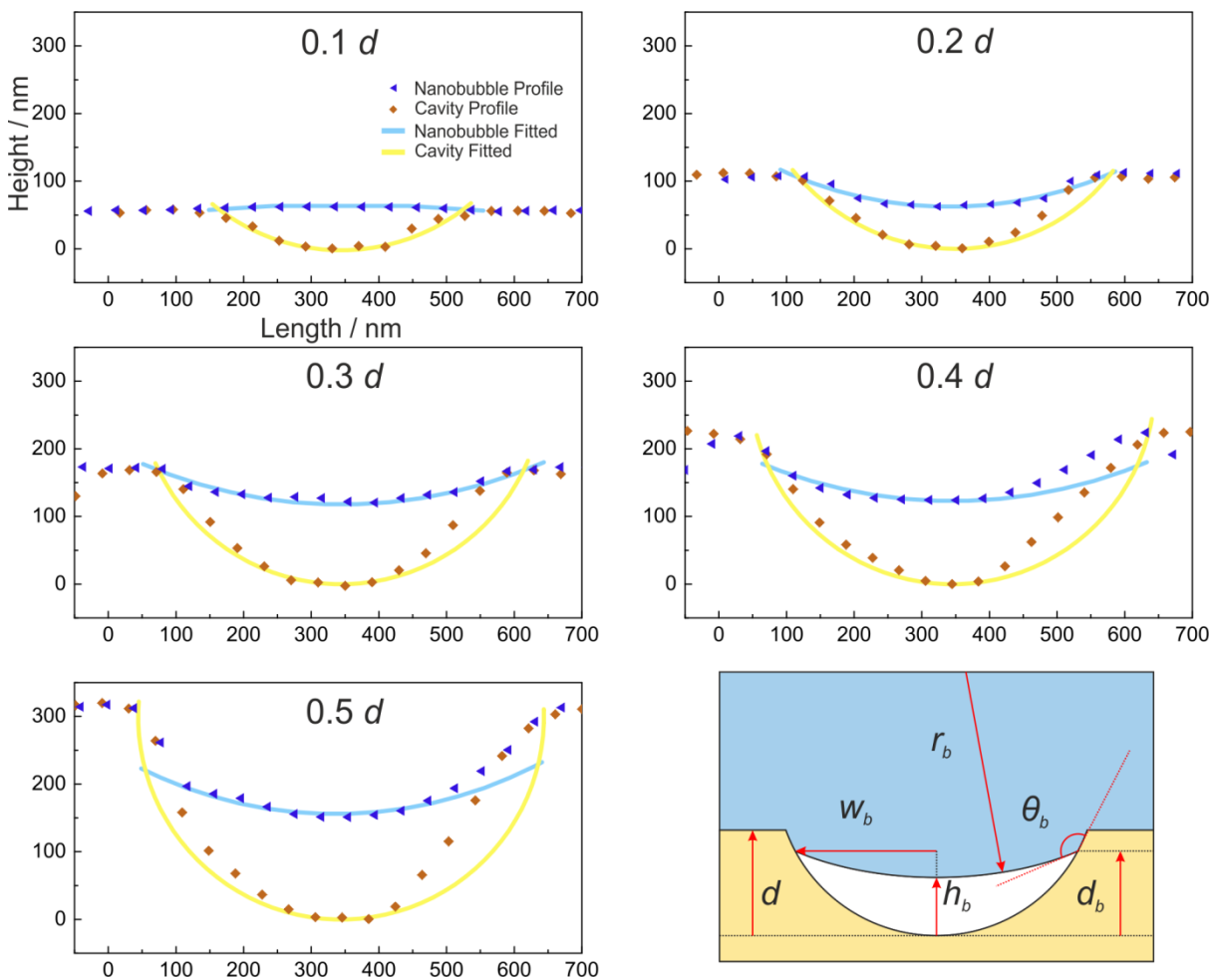


Figure 7.4 Profiles of nanobubbles (blue squares) overlaid onto cavity profiles (yellow triangles). Spherical caps have been fitted to the data points. The right sides of the cavities and bubbles have

been distorted due to an imaging artefact (more obvious in the 0.4 and 0.5 d). The cavity and nanobubble parameters are labelled.

Nominal d -value	Actual d - value	d_b	r_b (nm)	w_b (nm)	ϑ_b (°)	h_b (nm)	dP (Nm ⁻²)
0.1	0.10	0.10	+6,350	177	35	64	+23,000
0.2	0.18	0.18	-1,200	231	39	63	-120,000
0.3	0.29	0.29	-1,500	271	54	118	-96,000
0.4	0.38	0.30	-1,500	274	55	124	-96,000
0.5	0.53	0.35	-1,300	286	60	155	-111,000

Figure 7.5 Nominal dimensionless film height, Actual dimensionless film height, dimensionless three phase contact line location, d_b , nanobubble radius of curvature, r_b , nanobubble radius, w_b , nanobubble contact angle, ϑ_b , nanobubble height, h_b and the Laplace pressure ($dP = 2\gamma / r_b$) where γ is the surface tension of water (0.072 Nm⁻¹) All are measured from the images in figure 7.4.

Interesting changes are observed as the d value is increased. In the 0.1 d structure, nanobubbles are either flat or have a slight positive curvature to the interface. Between 0.2 and 0.5 d a *negative* curvature is present, which implies that there is a sub-atmospheric pressure generated within the nanobubble, as opposed to the positive pressure in nanobubbles on a flat surface.

An increasing penetration of the nanobubble into the cavity is observed with increasing d value. In the 0.4 and 0.5 d the location of the interface is no longer pinned to the rim at the top of the cavity and takes a position lower on the side wall ($d_b \neq d$). This finding is consistent with Checco *et al.* who used small angle x-ray scattering to estimate the amount of gas in their surface structure¹¹. However in the 0.1 to 0.3 d the meniscus remains attached to the cavity rim ($d_b = d$). There is a positive correlation between the contact angle and d value. However, as mentioned before several factors change with d value; side wall angle and the radius of the cavity mouth which may cause this effect. The radius of bubbles, w_r , in the larger d values could be considered to perhaps be

pushing the upper limit of being a 'nano' bubble compared to those found on a flat surface. A possibility is that macro sized phenomena are more prevalent at this scale. However the contact angles in the lower d values are more consistent with nanobubbles on a flat surface and even in the 0.5 d structure the contact angle is much larger than in the macroscopic case. Most surprisingly the Laplace pressure, calculated from the radius of curvature is very strongly negative. So negative it in fact predicts a negative *absolute* pressure (Atmospheric Pressure + Laplace Pressure) in some cases. Even if the pressure is not negative in absolute terms, it is certainly low enough to cause the water to be vaporised. One might also expect that the negative curvature and pressure to lead to an expansion of the bubble until it reached a lower energy state with a larger curvature. This is especially puzzling in the 0.4 and 0.5 d structures, where the nanobubbles have receded into the cavity and are free to expand, moving the meniscus up the side of the cavity. The results of Checco *et al.* also indicated a negative curvature was present in nanobubbles that had receded into their parabolic cavities¹¹, however they concluded that their estimation of the angle of cavity wall could be the problem.

This calculation of pressure must be flawed. This can be attributed to either or both of two things:

1. The measured curvature of the bubble is incorrect ie. there is an imaging artefact, causing a false nanobubble profile.
2. The measured curvature of the bubble is correct and the equation for Laplace pressure no longer applies at this size.

With regard to point 1; there has been much discussion about the deformation of nanobubbles during the AFM measurement, leading to a distorted profile, affecting the height, width, radius of curvature, contact angle etc. This problem is especially hard to solve as AFM is the only method of obtaining detailed structural information about nanobubbles so no comparison of profiles can be made to check the AFMs accuracy. Indeed this is a difficult problem that all investigations observing nanobubbles using AFM must contend with. The nature of AFM imaging requires a force to be exerted by the tip onto the substrate. Several authors have looked at the same nanobubble covered region in a range of imaging conditions to quantify differences in the observed nanobubble profile. What is clear is that imaging using higher force leads to a reduction in both height and width¹⁷. With this in mind in our experiments the amplitude was slowly increased to use the smallest force possible which also gave a coherent image. However, with no means to make a secondary measurement to confirm the AFM data this cannot be ruled out.

With regard to point 2; the Laplace equation must break down at some point. For example if we *reductio ad absurdum* to a molecular scale of one or two gas molecules surrounded by a liquid the

concepts of pressure, curvature and surface tension are certainly no longer valid. It seems that the Young equation for contact angles does not apply at this length scale either, where the liquid side angle is often observed to be in the range of 50° larger when bubbles are nano sized. It is also agreed that the supposed high internal pressure given by the Laplace equation for nanobubbles on a flat surface should lead to a near immediate collapse of the nanobubble – however they are observed to persist for days with no change in volume. However we cannot conclusively say our observation of extreme curvature is due to this.

It is not possible to certain whether one or both of these mechanisms are at play.

One of the motivations to make such a surface is to reduce the force required to move a nanobubble; thus preventing coalescence and a reduction in nanobubble coverage which has been shown to occur when subject to more aggressive AFM imaging modes^{17,18}. It is possible to quantify this force using an analysis similar to the movement of a water drop¹⁹, which was also applied to nanobubbles in¹². The work done W to move a bubble or drop length l with force F is:

$$W = F l \quad (7.3)$$

Nb. Normally the term advancing contact angle refers to the advancing contact angle of a liquid drop not a bubble, where the situation is reversed, ie. the leading edge of a drop is equivalent to the trailing edge of a bubble as in both new solid-liquid interface is being created. Here as we are only talking about bubbles for the ease of discussion the advancing contact angle is defined as the leading edge of the bubble and receding to the trailing edge with respect to movement.

When a bubble is moved along a surface, at the leading edge solid-gas interface is being created and solid-liquid interface is being destroyed; the reverse is true at the trailing edge. If the contact angle were the same at both edges, no energy would be lost in the movement as the energy cost to swap solid-liquid to solid-gas interface at the leading edge would be recouped at the trailing edge. However, the effect of contact angle hysteresis causes more energy to be expended at the trailing edge than is recouped at the leading edge. From the Young equation the difference in force exerted per unit length of contact line Δf between the solid-gas and the solid-liquid interfaces where γ is surface tension and subscript sg is solid gas, sl is solid liquid, lg is liquid gas and θ is contact angle is:

$$\Delta f = \gamma_{sg} - \gamma_{sl} = \gamma_{lg} \cos\theta \quad (7.4)$$

So the force to move a bubble, where w is the width of the bubble (the length over which the change in interface occurs), θ_a is the advancing contact angle and θ_r is the receding contact angle is:

$$F_{flat} = w \gamma_{lg} (\cos(\theta_a) - \cos(\theta_r)) \quad (7.5)$$

When the bubble is confined to a cavity the leading edge must be pushed over the rim of the cavity, so the angle of the surface changes providing another barrier for movement, which in effect amplifies the contact angle hysteresis as shown in figure 5.7. The difference in angle between the cavity side wall and the top of the structures (τ) is subtracted from the advancing contact angle, so the force to move the bubbles from the cavity is:

$$F_{cav} = w \gamma_{lg} (\cos(\theta_a - \tau) - \cos\theta_r) \quad (7.6)$$

Zhang *et al.* attempted to measure the contact angle hysteresis of nanobubbles on a highly ordered pyrolytic graphite surface whilst growing and shrinking the nanobubbles by controlling the concentration of dissolved gas within the water²⁰. They found the hysteresis of a drop of water in air to be $18 \pm 3^\circ$ however the nanobubbles seemed to not exhibit any hysteresis although the error in their measurement was $\pm 6^\circ$. For example if the advancing contact angle on a flat surface was 163° and the receding was 157° (6° of hysteresis) if the bubble was in a cavity where τ , the difference in angle between cavity and the top of the surface was 53° (equivalent to a $0.2 d$ cavity) the force required to move the bubble must be more than 16 times stronger than on a flat surface (and many more times than that if the hysteresis is $< 6^\circ$).

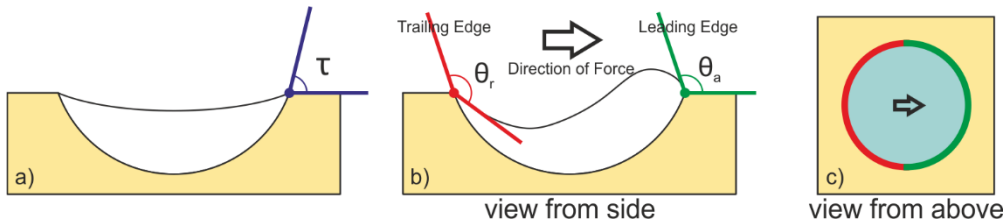


Figure 7.7 Sketches of cavity with a nanobubble viewed from the side and above. a) Nanobubble at equilibrium with the angle shown between sidewall and flat surface τ b) View from side of nanobubble in cavity with force applied from left to right. Areas in green indicate the leading

edge which has the advancing contact angle, areas in red are trailing edge which has the receding contact angle. c) View from above the nanobubble in cavity

To demonstrate the increased immobilisation of nanobubbles in cavities, contact imaging was used to exert a much larger force on the bubbles. A region of the 0.2 d surface was imaged consecutively in tapping mode, contact mode and tapping mode again (Figure 7.8). The initial tapping mode image, shows the presence of concave nanobubbles trapped within the cavities (the bubbles have a less intense purple colour). Contact mode imaging was done to try to move the nanobubbles, the image does not show any signs of nanobubbles as the tip penetrates the meniscus and traces the profile of the cavities. The surface was finally imaged in tapping mode again to observe the effect of contact mode imaging on the bubbles. An almost identical image is seen to the initial tapping mode with no coalescence or removed bubbles.

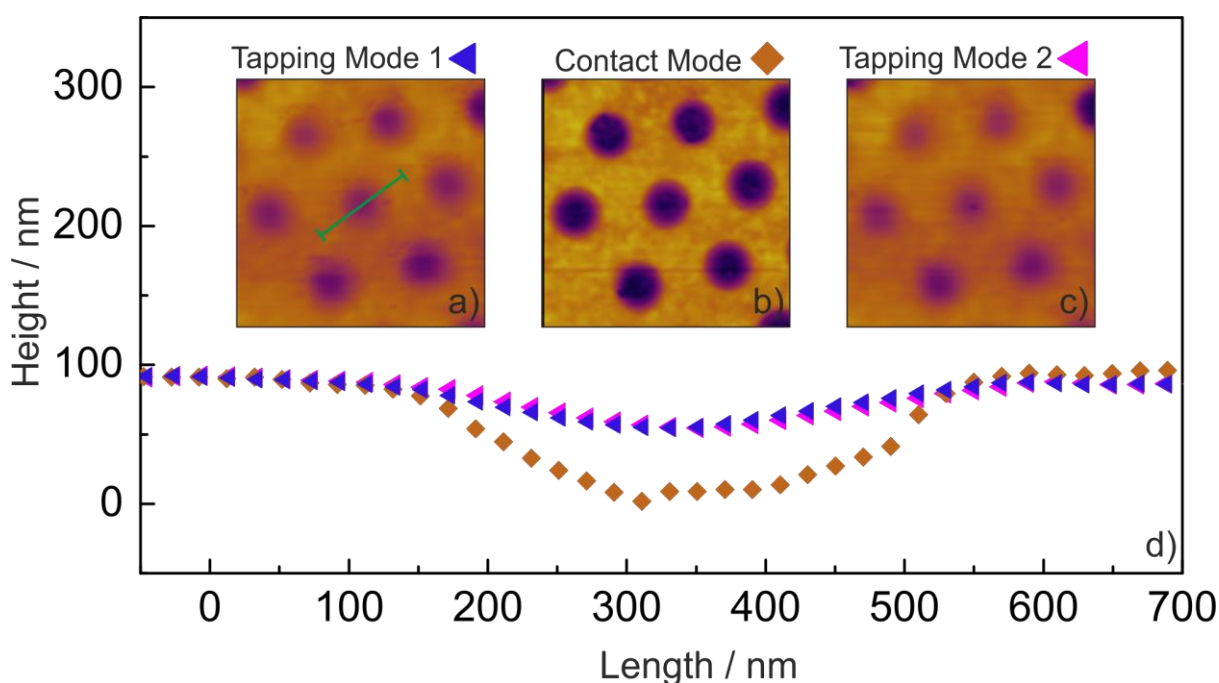


Figure 7.8 Atomic Force Microscopy images of the 0.2 d surface structure in a) tapping mode 1 b) contact mode c) tapping mode 2 and d) graph showing the profiles of each image along the red line in a). Tapping mode images were taken with setpoint ratio of 0.5.

The practicality of nucleating nanobubbles must also be considered if nanobubble laden surfaces are to be used in real world situations; the milder or closer to the operating conditions the better, which will most likely be room temperature ~ 20 °C. Seddon *et al.* identified the nucleation phase space of nanobubbles on a flat hydrophobized silicon wafer as a function of gas concentration and

temperature (figure 7.9) ²¹. The symbols on the graph from Seddon *et al.* are as follows: circles = nothing observed, crosses = nanobubbles, pluses = micropancakes (*micropancakes are similar gaseous domains, normally several microns in diameter but a height of only ~1 nm*) the yellow star is the liquid temperature and gas concentration used in this study coupled with the cavity surface structure (~22 °C and 100 % saturation). We see the nanobubbles in the cavity surface structures are nucleated well outside of the phase space expected for a flat surface. The macroscopic contact angle on the substrate is also known to be a determining factor in nanobubble nucleation; however for both studies this value is 110 ° so the increased phase space is attributed wholly to the cavity structures. Importantly with cavity structures, the liquid conditions of 22 °C and 100 % saturation mean no prior treatment to the water is needed to ensure nucleation, which is not the case with a flat surface. Most authors rely on the alcohol / water exchange method to produce nanobubbles to avoid the preparation of heated water at a specific gas concentration, but this can give varying results in itself.

It seems likely that nucleation characteristics change with d value; as the 0.4 and 0.5 d do not show a complete coverage of nanobubbles. It is interesting that the 'less' structured 0.1 d shows a full coverage whereas the 0.5 d does not in these conditions, one might expect it would be easier to trap bubbles in a more prominent surface structure.

The unreliable nucleation of nanobubbles has been an issue for those working with them. Different fractional coverages, sizes and shapes of nanobubbles can occur under seemingly similar nucleation conditions. The alcohol / water exchange method relies on the mixing of the two fluids, which is an inherently chaotic process, and is also dependant on cell shape and flow rate of fluid into and out of the cell; the exact method presumably changes between groups. The use of nanostructured cavities means a reliable coverage, size and shape of nanobubbles. The nanobubbles were also stable over a period of at least 7 hours with no change in volume.

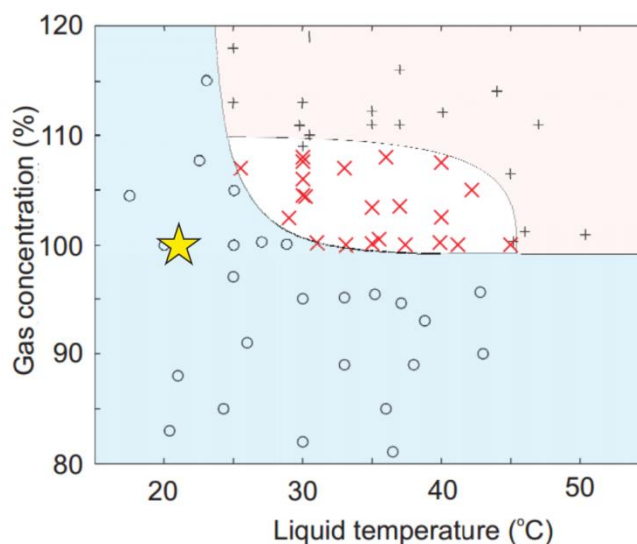


Figure 7.9 The nucleation phase space of nanobubbles from Seddon *et al.* ²¹. From the conditions and surface in their study circles = nothing observed, crosses = nanobubbles, pluses = micropancakes. From the surface and conditions in this study = the yellow star. The surface structure has increased the nucleation phase space of nanobubbles.

Several authors have noted the importance of the effect of meniscus angle and protrusion of bubbles on the slip length and therefore drag reducing properties of the surface ^{14, 22, 23}. Where the bubbles are either highly concave or convex the slip length can become negative, which acts to increase the drag force. A flat meniscus provides the largest possible slip length according to computer modelling studies, moderate curvature reduces the slip length and at $\sim 60^\circ$ of protrusion the benefits of the slip are completely outweighed by the curvature effect ^{14, 23}. By changing the d value, the nanobubble angle of protrusion could be effectively controlled to optimise the surface for maximum slip, however this also effects fractional area coverage of bubbles. For example at 0.3 d , where the bubble meniscus is still pinned to the rim of the cavity, the protrusion angle is -26° with a fractional area coverage of 76 %.

The coalescence of nanobubbles between two approaching hydrophobic surfaces causes the formation of capillary bridges which act to pull the two surfaces together; also called hydrophobic attraction.⁴ This adhesive force is very strong and greatly increases the observed friction between the surfaces.⁷

By containing nanobubbles within cavities this coalescence process would be hampered. As discussed the bubbles can have negative curvature (in the 0.2 – 0.5 d) so not protrude above the

top of the surface. This should prevent bridging coalescence to another surface by the tops of the cavities protecting the nanobubbles; thus could prevent the attractive force.

7.3 Conclusion

Structured surfaces have been made by templated electrodeposition around 600 nm polystyrene spheres from heights of 0.1 to 0.5 of the spheres diameter and modified with a hydrophobic self assembled monolayer. When submersed in water, stable nanoscopic bubbles are found to occupy the cavities. The surface structure successfully controls key properties of the bubbles: fractional coverage, width, height, contact angle, pressure and protrusion.

The bubbles in the 0.1 – 0.3 d surface structures have parameters consistent with nanobubbles on a flat surface in terms of height, width and contact angle. Bubbles in the 0.4 and 0.5 d are quite large when compared to conventional nanobubbles, although they still do not conform to macroscopic theory. The curvature of the nanobubble interface in the 0.2 – 0.5 d is negative and small. The pressure predicted from the Young-Laplace equation is negative in absolute terms, which is puzzling. The cause of this has not been resolved although it is thought to be due to imaging artefact or a break down of this equation at small length scales.

The theoretical understanding of the increased force required to move a bubble due to the three phase contact line moving over the cavity rim has been developed. Experimentally it proved impossible to remove the bubbles from the cavities even when subjected to contact mode imaging.

The nucleation phase space of nanobubbles was increased by a considerable amount due to the surface structure. This has great practical importance as no prior treatment to the substrate or water is required to guarantee good nanobubble coverage. Two very important parameters which relate to the resulting slip length of the surface are also effectively controlled with d value; the protrusion and the coverage. This surface structure could have great potential for use by other authors in the field to reproduce nanobubbles of a chosen height, width, contact angle or pressure for any desired application.

7.4 References

1. Tyrrell, J. W. G.; Attard, P. Images of nanobubbles on hydrophobic surfaces and their interactions. *Phys. Rev. Lett.* **2001**, 87 (17).
2. Lou, S. T.; Ouyang, Z. Q.; Zhang, Y.; Li, X. J.; Hu, J.; Li, M. Q.; Yang, F. J. Nanobubbles on solid surface imaged by atomic force microscopy. *Journal of Vacuum Science & Technology B* **2000**, 18 (5), 2573-2575.
3. Epstein, P.; Plesset, M. On the Stability of Gas Bubbles in Liquid - Gas Solutions. *The Journal of Chemical Physics* **1950**, 18, 1505.

4. Attard, P. Nanobubbles and the hydrophobic attraction. *Adv. Colloid Interface Sci.* **2003**, *104* (1), 75-91.
5. Wu, Z.; Chen, H.; Dong, Y.; Mao, H.; Sun, J.; Chen, S.; Craig, V. S.; Hu, J. Cleaning using nanobubbles: defouling by electrochemical generation of bubbles. *J. Colloid Interface Sci.* **2008**, *328* (1), 10-14.
6. Pashley, R. Effect of degassing on the formation and stability of surfactant-free emulsions and fine teflon dispersions. *The Journal of Physical Chemistry B* **2003**, *107* (7), 1714-1720.
7. Hampton, M. A.; Donose, B. C.; Taran, E.; Nguyen, A. V. Effect of nanobubbles on friction forces between hydrophobic surfaces in water. *J. Colloid Interface Sci.* **2009**, *329* (1), 202-207.
8. Bico, J.; Marzolin, C.; Quéré, D. Pearl drops. *EPL* **1999**, *47* (2), 220.
9. Abdelsalam, M. E.; Bartlett, P. N.; Kelf, T.; Baumberg, J. Wetting of regularly structured gold surfaces. *Langmuir* **2005**, *21* (5), 1753-1757.
10. Agrawal, A.; Park, J.; Ryu, D. Y.; Hammond, P. T.; Russell, T. P.; McKinley, G. H. Controlling the location and spatial extent of nanobubbles using hydrophobically nanopatterned surfaces. *Nano Lett.* **2005**, *5* (9), 1751-1756.
11. Checco, A.; Hofmann, T.; DiMasi, E.; Black, C. T.; Ocko, B. M. Morphology of air nanobubbles trapped at hydrophobic nanopatterned surfaces. *Nano Lett.* **2010**, *10* (4), 1354-1358.
12. Wang, Y.; Bhushan, B.; Zhao, X. Improved nanobubble immobility induced by surface structures on hydrophobic surfaces. *Langmuir* **2009**, *25* (16), 9328-9336.
13. Wang, Y.; Bhushan, B.; Zhao, X. Nanoindents produced by nanobubbles on ultrathin polystyrene films in water. *Nanotechnology* **2009**, *20* (4), 045301.
14. Steinberger, A.; Cottin-Bizonne, C.; Kleimann, P.; Charlaix, E. High friction on a bubble mattress. *Nature Materials* **2007**, *6* (9), 665-668.
15. Bartlett, P.; Baumberg, J.; Birkin, P. R.; Ghanem, M.; Netti, M. Highly ordered macroporous gold and platinum films formed by electrochemical deposition through templates assembled from submicron diameter monodisperse polystyrene spheres. *Chem. Mater.* **2002**, *14* (5), 2199-2208.
16. Cassie, A.; Baxter, S. Wettability of porous surfaces. *Trans. Faraday Society* **1944**, *40*, 546-551.
17. Walczyk, W.; Schön, P. M.; Schönherr, H. The effect of PeakForce tapping mode AFM imaging on the apparent shape of surface nanobubbles. *J. Phys.: Condens. Matter* **2013**, *25* (18), 184005.
18. Simonsen, A. C.; Hansen, P. L.; Klösgen, B. Nanobubbles give evidence of incomplete wetting at a hydrophobic interface. *J. Colloid Interface Sci.* **2004**, *273* (1), 291-299.
19. Furmidge, C. Studies at phase interfaces. I. The sliding of liquid drops on solid surfaces and a theory for spray retention. *Journal of Colloid Science* **1962**, *17* (4), 309-324.
20. Zhang, X. H.; Li, G.; Maeda, N.; Hu, J. Removal of induced nanobubbles from water/graphite interfaces by partial degassing. *Langmuir* **2006**, *22* (22), 9238-9243.
21. Seddon, J. R.; Kooij, E. S.; Poelsema, B.; Zandvliet, H. J.; Lohse, D. Surface bubble nucleation stability. *Phys. Rev. Lett.* **2011**, *106* (5), 056101.
22. Steinberger, A.; Cottin-Bizonne, C.; Kleimann, P.; Charlaix, E. Nanoscale flow on a bubble mattress: Effect of surface elasticity. *Phys. Rev. Lett.* **2008**, *100* (13), 134501.
23. Davis, A. M.; Lauga, E. Geometric transition in friction for flow over a bubble mattress. *Phys. Fluids* **2009**, *21*, 011701.

Chapter 8: Effect of Hydrophilic, Hydrophobic & Nanostructured Surfaces and Presence of Nanobubbles on Friction in a MEMS Contact

The aim of this work is to investigate the effect of hydrophobic, hydrophilic and nanostructured hydrophobic surface treatments on the friction in a MEMS tribometer. The presence or absence of nanobubbles is controlled to allow the assessment of any difference in friction associated with them.

8.1 Introduction

Microelectromechanical systems (MEMS) are devices which are built on a scale between 1 μm and 1 mm. In the last few decades MEMS devices have been developed for many new applications and have replaced larger macro sized systems. Examples include inkjet printer heads, read write heads for hard disk drives, micromirror arrays for display technologies and accelerometers found in a range of applications from airbags to mobile phones. MEMS devices are frequently fabricated from silicon which is micromachined to the desired form through a range of methods often involving photolithography, etching and thin film deposition techniques.

Despite these successes a major problem for MEMS devices is the poor tribological performance between sliding pairs where unacceptably high friction, wear and stiction (static friction) is common. The cause of these problems is partly due to the increase in surface to volume ratio as components are miniaturised; surface reduces as the square whereas the volume as the cube. This means surface effects such as capillary effects, skin friction drag, and van der Waal forces become much more important than body effects such as inertia. Poor tribological performance also stems from the ubiquitous use of silicon in MEMS devices, which has very poor tribological properties especially when rubbed against itself which is often the case.

Bare silicon is readily oxidised when exposed to the atmosphere leading hydroxyl termination at the surface which has strongly hydrophilic wetting properties. When two surfaces are contacted

water from the atmosphere can condense into capillary bridges between the roughness elements leading to a strong adhesive force which leads to stiction and high friction¹. Current methods to better the tribological properties of silicon based MEMS devices include boundary lubricants, surface coatings, vapour phase lubrication and liquid lubrication.

Boundary lubricants include hydrogen termination of the silicon or attachment of a long alkyl chain self assembled monolayers (SAMs) acts to make the silicon surface more hydrophobic and reduce its surface energy. This has been shown to be a very successful tactic to eliminate stiction between silicon parts and to reduce boundary friction². When the surface is hydrophobic the relative pressure in capillary bridges becomes less negative and so the work of adhesion is much reduced. Treatment of a silicon surface with the commonly used SAM octadecyltrichlorosilane (OTS) can reduce the static coefficient of friction from 2.1 to 0.11 and dynamic coefficient of friction ~ 4.9 to 0.08.³

The silicon can also be coated with standard tribological materials for example diamond like carbon, silicon carbide, alumina and titania. Both modification of the silicon surface chemically and coating with other materials is effective where relatively little sliding occurs. However when more challenging tribological conditions are encountered where components experience substantial amounts of relative motion vapour phase and liquid lubrication are more effective.

Initially liquid lubrication of MEMS devices was thought to be unappropriated as viscous dampening of the lubricant is more significant at smaller scales⁴ however more recently liquid lubrication of MEMS has been reconsidered. Ku *et al.* used a custom made MEMS tribometer where a stationary disk is loaded against a rotating disk (both flat silicon and 2 mm in diameter) to investigate a range of potential lubricants⁵. They found lubricants with low viscosity were effective and a classic Stribeck type curve was observed as speed increased, figure 8.1. The normal load for all conditions was 0.048 N (nominal pressure of 15 kPa), the viscosity of the lubricants at 25 °C was 0.888 cP for silicone, 0.890 cP for water, 3.032 cP for hexadecane and 28.0 cP for squalane.

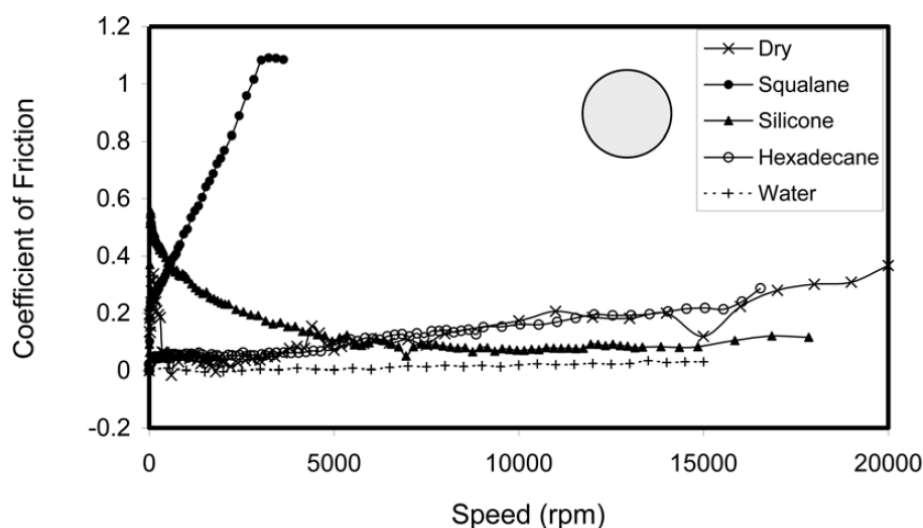


Figure 8.1 Stribeck type behaviour of a range of liquid lubricants for a flat-on-flat silicon contact using a custom built MEMS tribometer from Ku *et al.*⁵. The squalane data is stopped after ~ 4000 RPM as the maximum torque detectable by the tribometer was exceeded.

In full film hydrodynamic condition the phenomenon of fluid/wall slip could allow further reductions to friction⁶. As discussed in the literature review the drag reduction for a given slip length is dependent on the separation between the two surfaces. In a MEMS contact this spacing is typically $<2\ \mu\text{m}$ for a flat-on-flat contact⁷ meaning a modest slip length could lead to a substantial drag reduction. Spikes developed the concept of the ‘half-wetted bearing’ showing the feasibility of a low load low friction bearing with one hydrophobic surface allowing slip and the other hydrophilic to aid lubricant entrainment^{8,9}.

Several papers have reported a slip like effect for hydrophobic surfaces but not for hydrophilic surfaces. Choo *et al.* compared hydrophilic (mica) vs hydrophobic (mica with hydrolysed octadecyltriethoxysilane (OTE) self assembled monolayer) surfaces in hydrodynamic conditions¹⁰. The tribometer was a custom made rig which loaded a rotating steel wheel against a flat test sample with the desired surface properties. They showed that the mica with hydrophobic coating showed considerably less friction than the bare hydrophilic mica, figure 8.2. However the origin of the slip was not discussed.

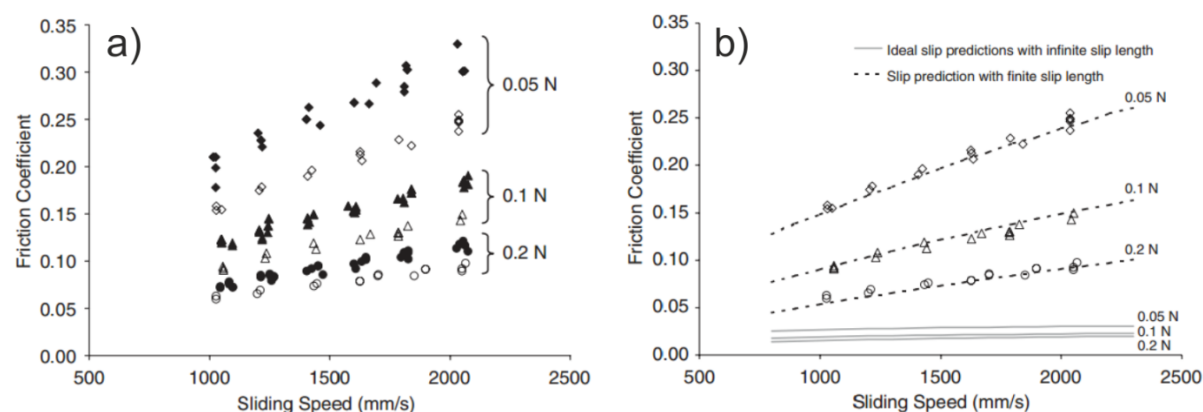


Figure 8.2 a) where solid black symbols indicate a hydrophilic surface and black outlines with white centre indicate a hydrophobic surface. b) Graph showing friction coefficient against sliding speed at 0.05, 0.1 and 0.2 N normal load for hydrophobic surfaces with dashed lines showing predicted slip length of 20 μm and solid lines infinite slip length.

Tretheway and Meinhart observed slip at hydrophobic walls in a microchannel which was not present for hydrophilic walls¹¹. They later proposed that the presence of nanobubbles on the hydrophobic surface caused slip on the liquid/gas interface¹².

It is frequently demonstrated that nanobubbles will only form on hydrophobic surfaces and not on hydrophilic ones. It is also known that slip could occur over the gas-liquid interface of the nanobubbles which has led to the reasonable suggestion that nanobubbles could be the cause of the slip⁶ and therefore explain reduced friction experienced by hydrophobic but not hydrophilic surfaces. Simulation of nanobubble covered surfaces have shown that slip lengths on the order of 100 nm should be expected although this is dependent on the curvature of the bubble surface¹³; much less than the 20 μm slip length calculated by Choo *et al.*¹⁰(figure 8.2 b) although the high shear rates used by Choo *et al.* could be responsible for the increase.

Others say the origin of slip is not due to interfacial nanobubbles instead propose electrostatic forces on the surface lead to slip¹⁴. The link between surface hydrophobicity, nanobubbles and slip remains poorly understood¹⁵.

In this work the custom built MEMS tribometer rig was used in a collaboration with the Tribology Group at Imperial College London. This tribometer is of the right scale to allow the discussed surface effects to have a significant impact on friction and has previously shown slip like behaviour using MAC-hexadecane as a lubricant¹⁶ and so is well suited for this study.

The effect of surface treatment on friction is investigated (flat hydrophobic, flat hydrophilic and nanostructured surfaces) lubricated by water and the relevance of nanobubbles on friction. The

MEMS tribometer rotates an upper sample against a stationary lower sample. Rubbing pairs of hydrophilic-on-hydrophilic, hydrophilic-on-hydrophobic and hydrophilic-on-nanostructured are compared with and without nanobubbles present in the contact (a test matrix shown in figure 8.3). The aim here is not to develop a fully comprehensive lubrication system for use in MEMS devices; however aspects of this work may inform future researchers how these surface properties may be used to their advantage when doing so.

		Upper Sample		
		Flat Hydrophilic		Flat Hydrophobic
Lower Sample	Flat Hydrophilic	Nanobubbles Absent	Nanobubbles Absent	
	Flat Hydrophobic	Nanobubbles Present	Nanobubbles Absent	Nanobubbles Absent
	Nanostructured Hydrophobic	Nanobubbles Present	Nanobubbles Absent	

Figure 8.3 Test matrix of upper and lower sample combinations and the presence or absence of nanobubbles in the contact used in the MEMS tribometer.

8.2 Experimental

The tribometer used in this work is a custom rig designed and built by the Tribology Group at Imperial College London, figure 8.4 shows a schematic of the contact⁷. The contact consists of two silicon disks 2 mm in diameter; an area type contact with nominal area of $3.14 \times 10^{-6} \text{ m}^2$. The upper disk is attached to the end of the shaft of a high speed electric motor via a self aligning coupling to minimise misalignment and the lower disk is mounted on a stationary platform with a system of elastic suspension beams. The height of the electric motor is adjusted by a computer-controlled stage which allows the upper disk to be loaded against the lower disk. The stiffness of the

suspension beams is calibrated to allow the normal load and torque to be gained from measurement of the displacement.

To measure rotational displacement a laser beam is deflected from a prism attached to the underside of the platform to a piezoelectric actuator and then reflected around 4 mirrors to increase the displacement of the beam and finally to a photodetector. A control loop between the photodetector and piezoelectric actuator holds the laser beam stationary on the photodetector allowing the voltage signal to the piezoelectric actuator to be calibrated to the rotational displacement of the platform. Measurement of the normal displacement is achieved using a laser displacement sensor underneath the platform which directly measures the distance from itself to the platform.

The normal load can be adjusted between 0.01 and 0.2 N, in this work the normal load was always 0.05N (nominal contact pressure 15.9 kPa). The rotational speed can be adjusted from 10 to 20 000 RPM. The sliding speed (u in ms^{-1}) is dependent on radius (r) within the contact and is related to the RPM by: $u = rpm \cdot \pi 2r / 60$ with the sliding speed being maximum at the circumference and 0 at the centre. This gives a maximum sliding speed of 2.09 ms^{-1} at the circumference of the disk when at 20 000 rpm, the highest motor speed.

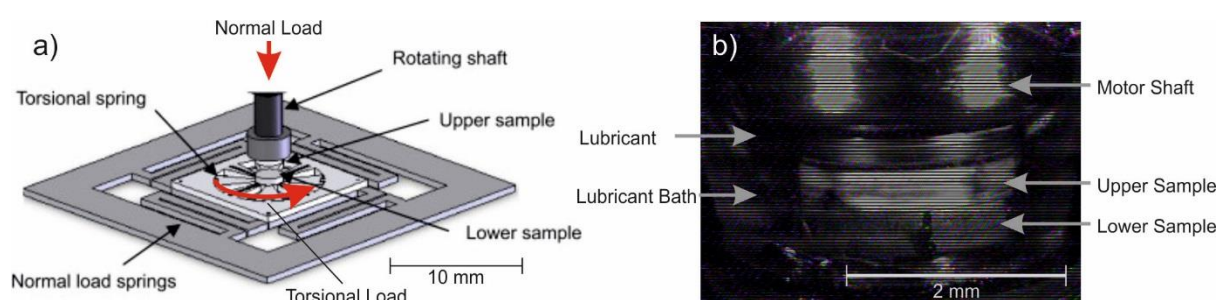


Figure 8.4 a) Schematic of the contacting parts of the MEMS tribometer adapted from Ku *et al.* ⁷

b) photograph of the contact

The upper and lower samples are fabricated out of bonded silicon on insulator wafer, <100> orientation, p-type boron doped. For hydrophilic samples the silicon was put in an oxygen plasma cleaner before each use which acts to clean the surface of any organic contaminants and oxidises the surface ensuring a very low ($< 10^\circ$) water contact angle. Flat hydrophobic samples were treated with octadecyltrichlorosilane (OTS) which forms a hydrophobic alkyl terminated monolayer on the surface which has a contact angle of 110° . The nanostructured surface was modified with 1-dodecanethiol immediately after the metal deposition, which forms an alkyl terminated monolayer on the surface which has a contact angle of $\sim 105^\circ$ on a flat nickel surface and $\sim 120^\circ$ on the nanostructured nickel in accordance with the Cassie-Baxter model of wetting. The surface roughness (R_a) of the samples was 0.1 – 0.8 nm for the silicon samples (Schmitt measurement

systems¹⁷) and 10 – 15 nm for the nickel deposit (Alicona Infinite Focus). The hardness (from the literature using nanoindentation) of silicon is 8.7 GPa¹⁸ and Nickel deposited from a saccharin doped Watts bath is 4.1 GPa¹⁹.

To fabricate the nanostructured samples the silicon surface was cleaned then 10 nm chromium and 100 nm gold were thermally deposited on to the surface. Chromium was used to enhance the adhesion to the silicon and gold was used as nickel electroplates readily onto it as the gold surface does not oxidise. Ideally the nanostructured surface would have been made of silicon and coated with OTS to minimise the number of variables however the desired cavity surface structure is not accessible through standard silicon micromachining techniques.

The templated electrodeposition was carried out in the same manner as discussed in the materials and methods chapter however was more challenging due to the small size of the samples. A silicon tab of $\sim 1 \text{ cm}^2$ holds 4 samples. To form the template 2 parafilm strips were placed along two of the edges of the tab. The solution containing the polystyrene spheres was deposited on to each of the sample in 2 μl drops using in micropipette. A glass cover slip was placed on the tab so it rested on the parafilm spacers and also touched the 4 drops placed on each of the samples. The assembly was left in a fridge at 12C° for one day to let the solution evaporate. This led to the formation of a hexagonally close packed 600 nm polystyrene spheres on the surface.

Nickel was then deposited around the polystyrene sphere template to a height of $\sim 105 \text{ nm}$ calculated from SEM images which equates to the $\sim 0.2 d$ in Chapter 7.

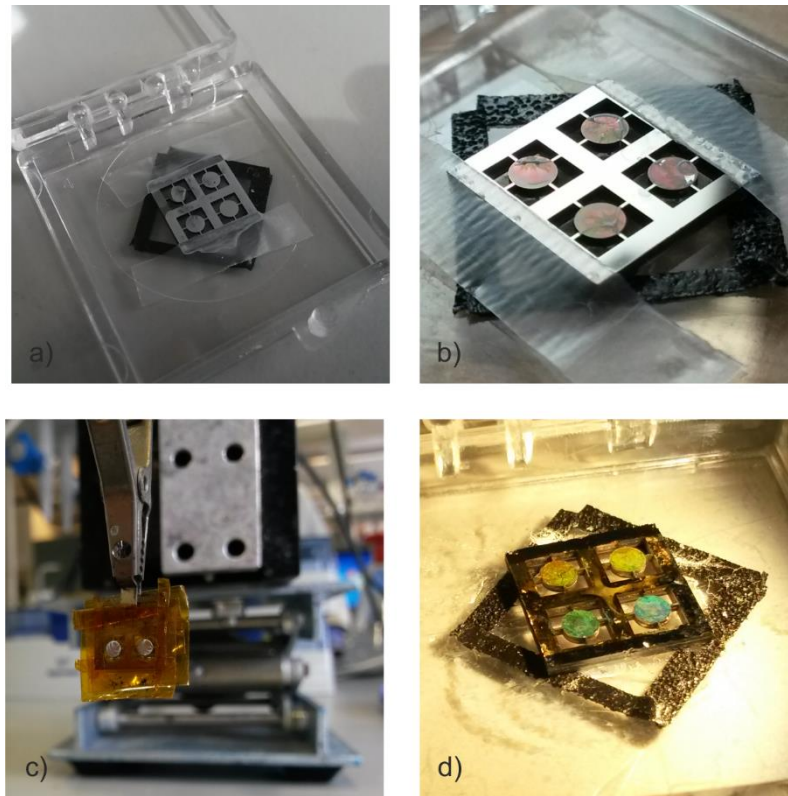


Figure 8.5 Fabrication of the nanostructured surface a) Solution containing polystyrene spheres deposited on samples and coverslip placed on top b) template on sample c) sample insulated with capton tape in area which don't require plating d) the finished sample the opalescent colours can be seen on the surface as they interact with visible light.

SEM images of the surface of the sample are shown in figure 8.5 a) and b). Hexagonally close packed cavities of ~ 450 nm in diameter can be seen on the surface, this implies a coating thickness of ~ 105 nm (around $0.2 d$). Due the poorer conductivity of nickel compared to gold (gold is 2.9 times as conductive) the SEM images are not as clear as the images of the gold sample shown in chapter 7. Figure 8.6 d) shows an SEM image of the same deposition height made of gold reproduced from chapter 7 to show the structure with increased clarity. Figure 8.6 c) also from chapter 7 shows the profiles from the AFM experiments of the nanobubbles found in the surface structure. This height of deposition of metal around the spheres was chosen as the curvature is not as extreme as in other structures and also has reasonable nanobubble coverage ($\sim 50\%$) to maximise any potential slip at the tribological contact. The material between the cavities also has a low aspect ratio (height divided by width) and should be more mechanically stable than higher aspect ratio structures which are likely to be more susceptible to wear.

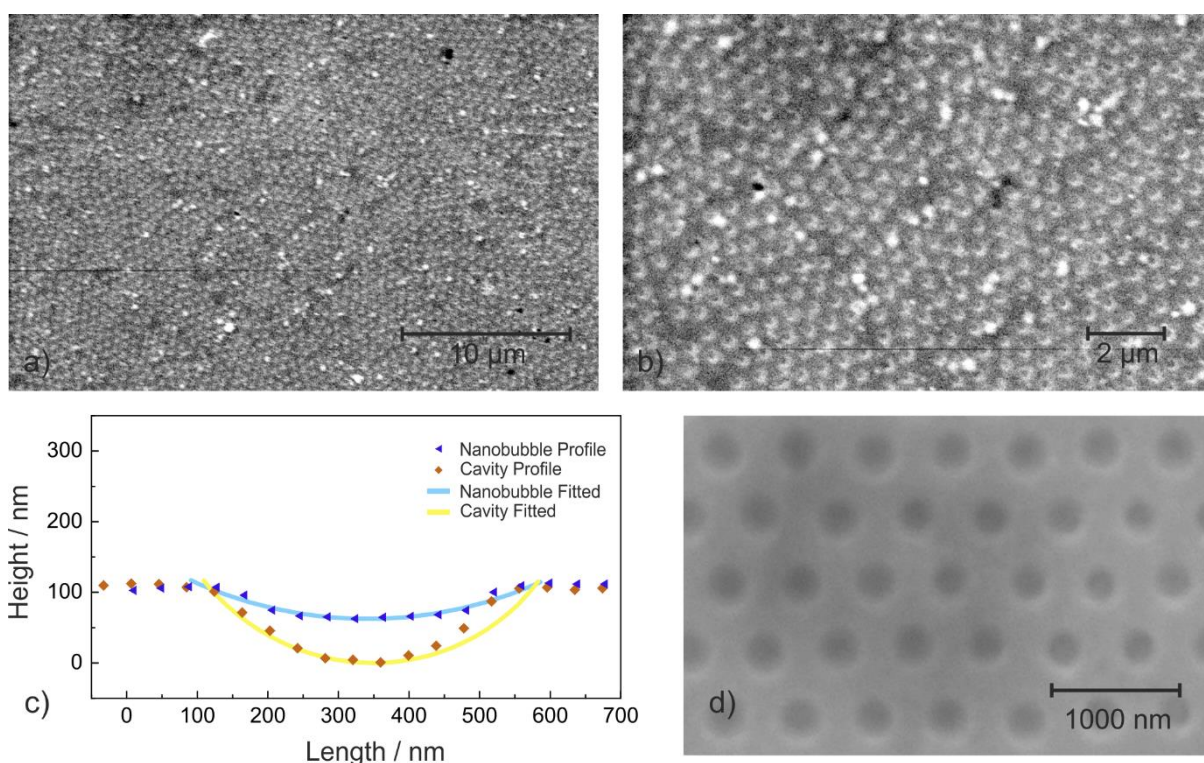


Figure 8.6 a),b) SEM images of the surface structure of the nanostructured samples made of nickel deposited to a height of ~ 105 nm around a 600 nm sphere template c) profiles of the nanobubble and cavity overlaid on one another from AFM images with fitted profiles (from chapter 7) d) SEM image of the 0.2 d gold structure (from chapter 7)

All samples are flat as opposed to a pad bearing which has also been used in previous work with this tribometer. The choice of a flat surface was made to maximise any evidence of slip as maximum reductions to friction are predicted where convergence is low⁸. The film thickness of the flat surface is also much lower which should lead to a greater friction reduction for a given slip. The formation of the polystyrene sphere template is also very sensitive to surface deformations which can inhibit the self assembly process and would be present on the pad bearing.

However this means that load support of the lubricating film in hydrodynamic conditions is not from fluid entrainment into a well defined geometric convergence; as is the case with the stepped on flat geometry where film thickness and coefficient of friction can be estimated by solving the Reynolds equation. In a flat on flat area contact hydrodynamic conditions are gained from the viscosity wedge effect described by Cameron²⁰. The sliding motion generates a temperature gradient in the film which leads to variations in viscosity in the lubricant. This has been shown to produce considerable load support where no geometric convergence is present. Further load support could occur through

Chapter 8

small misalignments between the upper and lower samples however these are thought to be small due to the repeatability of results. These mechanisms of load support are poorly understood and controlled which means estimation of the lubrication regime, film thickness and coefficient of friction is difficult for a flat on flat contact.

Throughout this work water (taken from a water purification system) is used as the lubricant for all of the conditions, and has a viscosity of 0.89 cP . Water has shown potential slip in a range of experiments and is the only liquid shown to allow stable surface nanobubbles. The presence of nanobubbles is controlled by careful preparation of water before each experiment. When the desired conditions required the absence of nanobubbles, the water was put in a vacuum desiccator before filling the bath and covering the lower sample. The whole assembly was then held under vacuum to ensure the solution was fully degased before the experiment was run. This has been shown to reliably remove nanobubbles from hydrophobic surfaces²¹.

When nanobubbles were required on a flat hydrophobic surface the ethanol/water solvent exchange method was used before every experiment. This is the most common method to obtain a coverage of nanobubbles on a hydrophobic surface and has been demonstrated numerous times^{22, 23} and therefore atomic force microscopy (AFM) images of nanobubbles on the flat silicon surface are not presented here.

The nanostructured surface described in chapter 7 has several perceived advantages over a flat surface.

1. No solvent exchange or other pretreatment is required for a coverage of nanobubbles.
2. The coverage is can be tuned and is repeatable
3. The curvature of the liquid/gas interface can be tuned
4. The nanobubbles are protected when they have negative curvature as they do not protrude above the surface
5. A larger force is required to move the nanobubble from the cavity than on a flat surface

In this work only the 0.2 d surface was used (deposition height of 120 nm through 600 nm diameter spheres) As shown in chapter 7 a full coverage of nanobubbles using the 0.2 d nanostructured sample was gained by using saturated water.

Throughout the results and discussion section the samples will be called hydrophobic, hydrophilic and nanostructured where:

Hydrophilic: flat silicon freshly cleaned in oxygen plasma contact angle 10°

Hydrophobic: flat silicon with OTS monolayer contact angle 110°

Nanostructured: Nickel templated around 600 nm spheres to a film thickness of 105 nm with 1-dodecanethiol monolayer contact angle 120°

Condition No.	Upper Sample	Lower Sample	Nanobubbles
1	Hydrophilic	Hydrophilic	No
2	Hydrophilic	Hydrophobic	No
3	Hydrophilic	Hydrophobic	Yes
4	Hydrophobic	Hydrophobic	No
5	Hydrophilic	Nanostructured	No
6	Hydrophilic	Nanostructured	Yes

Figure 8.7 Table showing the conditions tested

The conditions tested are shown in figure 8.7; conditions 1 and 2 will demonstrate the effect of changing one of the samples from hydrophilic to hydrophobic without nanobubbles present. From condition 3 the effect of introducing nanobubbles on the hydrophobic surface can be investigated. Condition 4 will show the effect of having both surfaces hydrophobic with no nanobubbles present. Conditions 5 and 6 will show the effect of the nanostructured sample on friction and whether the presence of nanobubbles is important.

Stribeck plots of coefficient of friction against speed were gained by increasing the speed of the motor and taking a measurement of friction averages over a 7 second period. The normal load was always 0.05N and the speed was increased logarithmically from 10 to 20,000 RPM. For each condition the test was run a minimum of 7 times, all plots show the average friction for each condition. Error bars show ± 1 standard deviation of the data. Results of conditions where one variable has been changed are discussed and compared to identify the effect on the friction. Post testing analysis of all of the surfaces is shown after the discussion of the friction data. After all results are presented general trends are identified and discussed.

As the hydrodynamic load support for this bearing is not generated by entrainment through a geometric convergence which means calculation of film thickness and lubrication regime is not possible. Lubrication regimes are suggested from the friction data following the classic Stribeck type behaviour with high friction at slow speeds (boundary lubrication) which then reduces to a minima with increasing speed (mixed lubrication) and then friction increases linearly with speed (hydrodynamic lubrication).

8.3 Results and Discussion

8.3.1 Hydrophilic/Hydrophilic & Hydrophilic/Hydrophobic No Nanobubbles

The difference between the hydrophilic/hydrophilic & hydrophilic/hydrophobic combinations without any nanobubbles (conditions 1 and 2) are presented in figure 8.8.

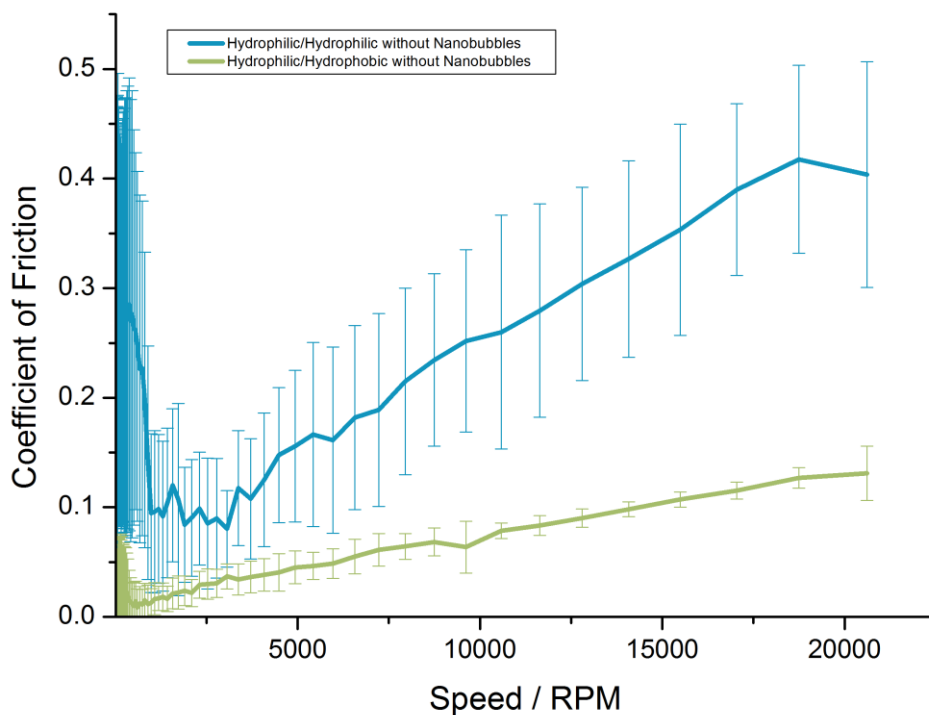


Figure 8.8 Plot of Coefficient of friction against speed for flat hydrophilic/hydrophilic & hydrophilic/hydrophobic with no nanobubbles present.

Hydrophilic/hydrophilic clearly has higher friction throughout the speed range however particularly in boundary and mixed lubrication conditions (0 to ~ 1000 RPM). There is also a very large standard deviation of the data as shown by the error bars indicating the friction behaviour of this combination is not very stable. As hydrodynamic conditions are approached the coefficient of friction drops to around 0.1 and then increases with speed as the lubricating film thickness increases.

The hydrophilic/hydrophobic combination has a markedly decreased coefficient of friction in boundary and mixed conditions when compared to the hydrophilic/hydrophilic combination. The coefficient of friction reaches values as low as 0.01 as it approaches hydrodynamic conditions and then increases throughout the hydrodynamic regime as expected through viscous losses.

The high friction of the hydrophilic/hydrophilic (bare silicon on silicon) contact in boundary and mixed conditions is expected as many groups have noted this previously². Scherge and Schaefer also showed stick/slip behaviour occurred in a silicon on silicon area contact at slow sliding speeds ($< 6 \mu\text{m s}^{-1}$) although in unlubricated conditions²⁴. Solvation effects could also cause stick-slip behaviour, which are more pronounced when surfaces are smooth and the molecular size of the lubricant is small; which is the case here²⁵. Contact of the silicon surfaces and stick/slip behaviour could explain the large standard deviation in boundary and mixed conditions. Post testing analysis of the surfaces (presented later) show some surface wear and evidence of surface contact.

Interestingly there is a significant difference in friction between the two combinations in hydrodynamic conditions when the surfaces are no longer in contact. Choo et al. showed a similar effect as discussed earlier (figure 8.3) attributing it to liquid slip at the wall of the hydrophobic surface¹⁰.

However it is possible the very high friction and large standard deviation observed in the hydrodynamic regime for the hydrophilic/hydrophilic contact could be in part due to surface contact through edge loading, for which there is evidence in post testing analysis. When compared to a similar condition run by Ku (flat on flat water lubricated) the friction is significantly higher, however the samples were not plasma cleaned before use and the author noted that the silicon adsorbed lubrication organic species from the air.¹⁷

Whether this is slip or not, this experiment clearly shows the marked decrease in friction due to the application of a hydrophobic SAM throughout the range of lubrication conditions.

8.3.2 Flat Hydrophilic/Hydrophobic Nanobubbles & No Nanobubbles

To look for the effect of nanobubbles on friction a flat hydrophilic/hydrophobic contact was compared with and without nanobubbles present on the surface, figure 8.9) (condition 2 and 3). It's clear there is no difference in friction between the two conditions. It is possible that nanobubbles present in the contact could be removed from the surface in the experiment by shear forces, or if they were not removed they did not have any significant impact on friction.

The formation of nanobubble capillary bridges if though to be the cause of the hydrophobic attraction cite. This has been shown to cause stiction in water submerged MEMS devices using cantilever beams. The results in figure 8.4 show that this effect is not significant in sliding contacts using hydrophilic/hydrophobic combinations.

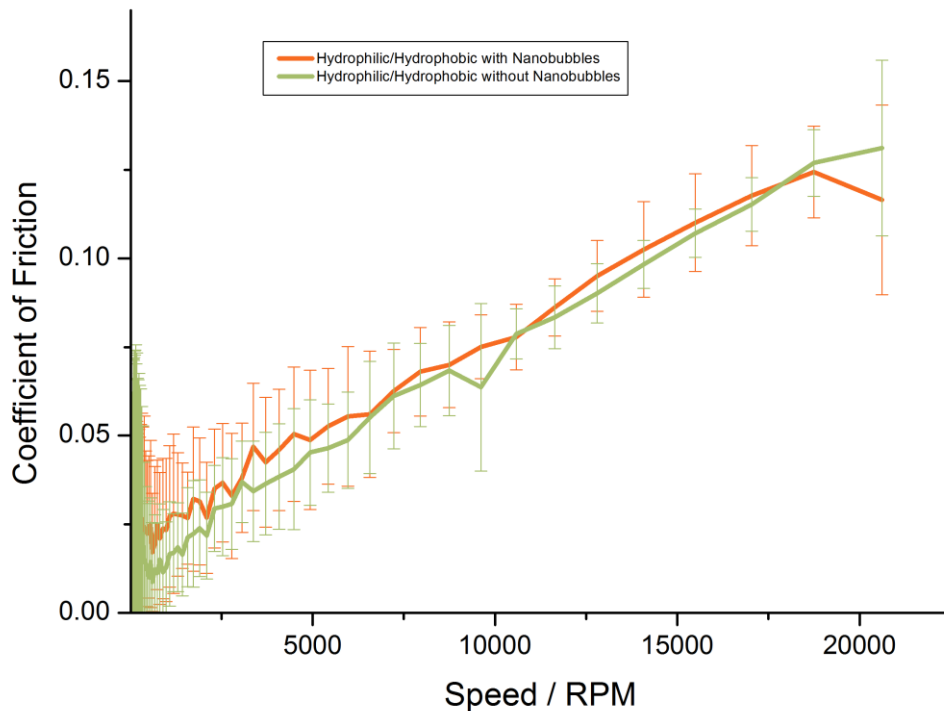


Figure 8.9 Plot of coefficient of friction against speed for flat hydrophilic/hydrophobic with and without nanobubbles present.

8.3.3 Hydrophilic/Nanostructured Nanobubbles & No Nanobubbles

The hydrophilic/nanostructured combination was compared with and without nanobubbles present on the surface, figure 8.10. In boundary and mixed conditions the sample with nanobubbles seems to have lower friction and in hydrodynamic conditions there is no difference between the

two. The coefficient of friction in hydrodynamic conditions is lower than a flat hydrophobic/hydrophilic contact so it seems the nanotexture of the surface could lead to friction reduction a mechanism unrelated to nanobubbles. However wear of the sample could have led to a change in friction for these experiments which is discussed later.

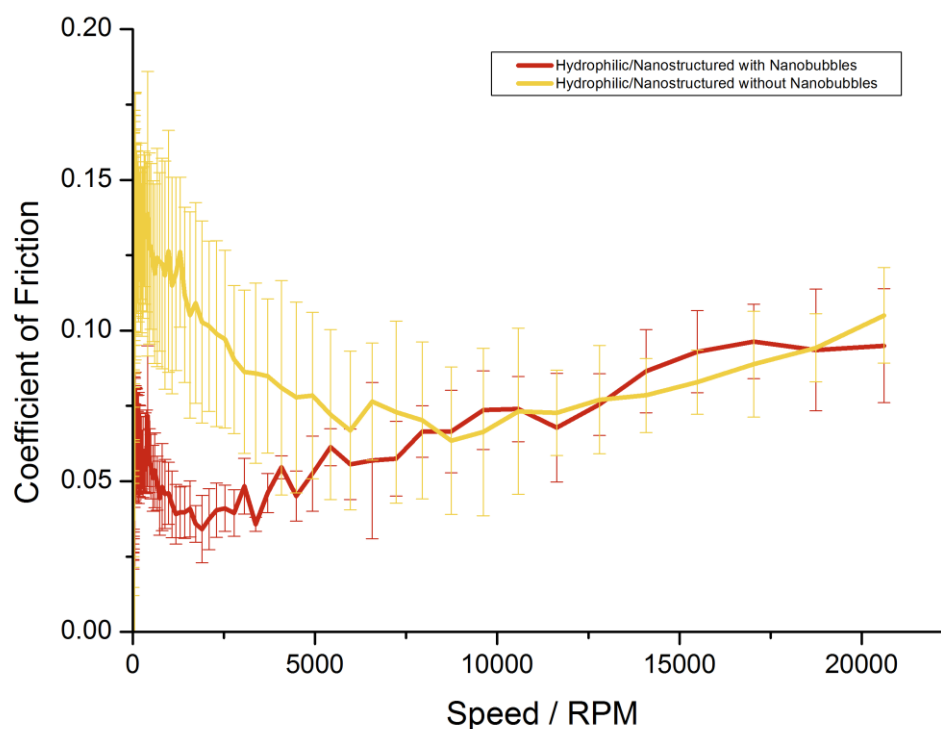


Figure 8.10 plot of Coefficient of friction against speed for Hydrophilic/Nanostructured Nanobubbles & No Nanobubbles

8.3.4 Hydrophobic/Hydrophobic & Hydrophilic/Hydrophobic No Nanobubbles

Finally hydrophobic/hydrophobic & hydrophilic/hydrophobic conditions are compared with no Nanobubbles present, figure 8.11. Initially friction is higher in the hydrophobic/hydrophobic pair up in boundary conditions and then is lower in hydrodynamic lubrication.

The higher friction in boundary conditions could be due to interaction of the SAMs from the two surfaces. It is worth noting that the high friction could not have been due to nanobubbles, which are thought to be the probable cause of the large long range adhesive force between submerged hydrophobic surfaces ²⁶.

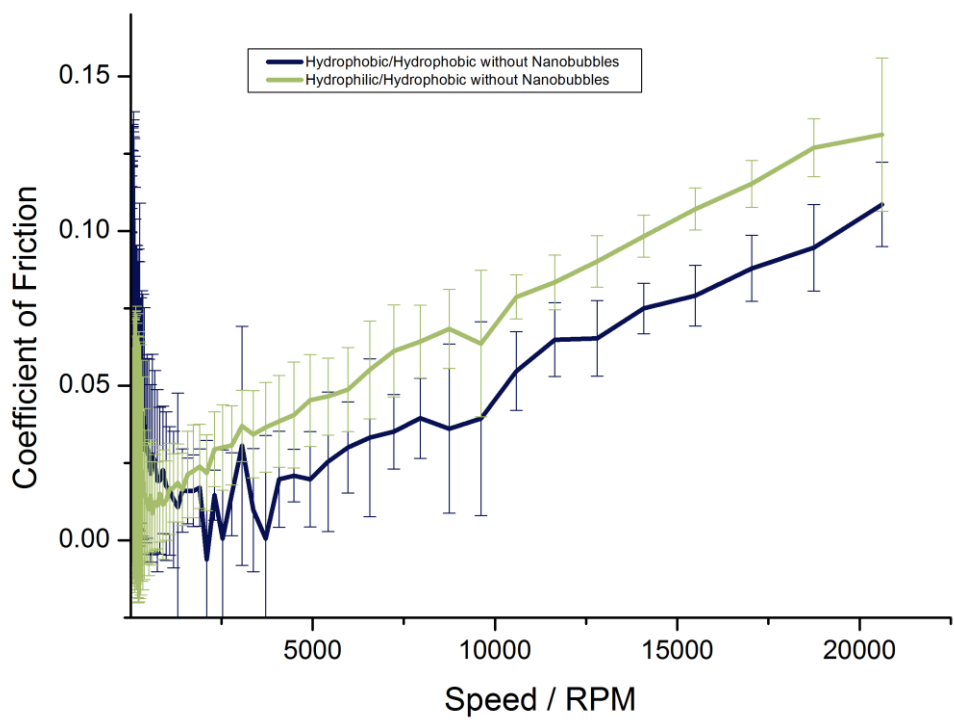


Figure 8.11 plot of Coefficient of friction against speed for Hydrophobic/Hydrophobic & Hydrophilic/Hydrophobic No Nanobubbles.

8.3.5 Analysis of Surfaces Post-Testing

Figure 12 shows SEM images of the samples post testing.

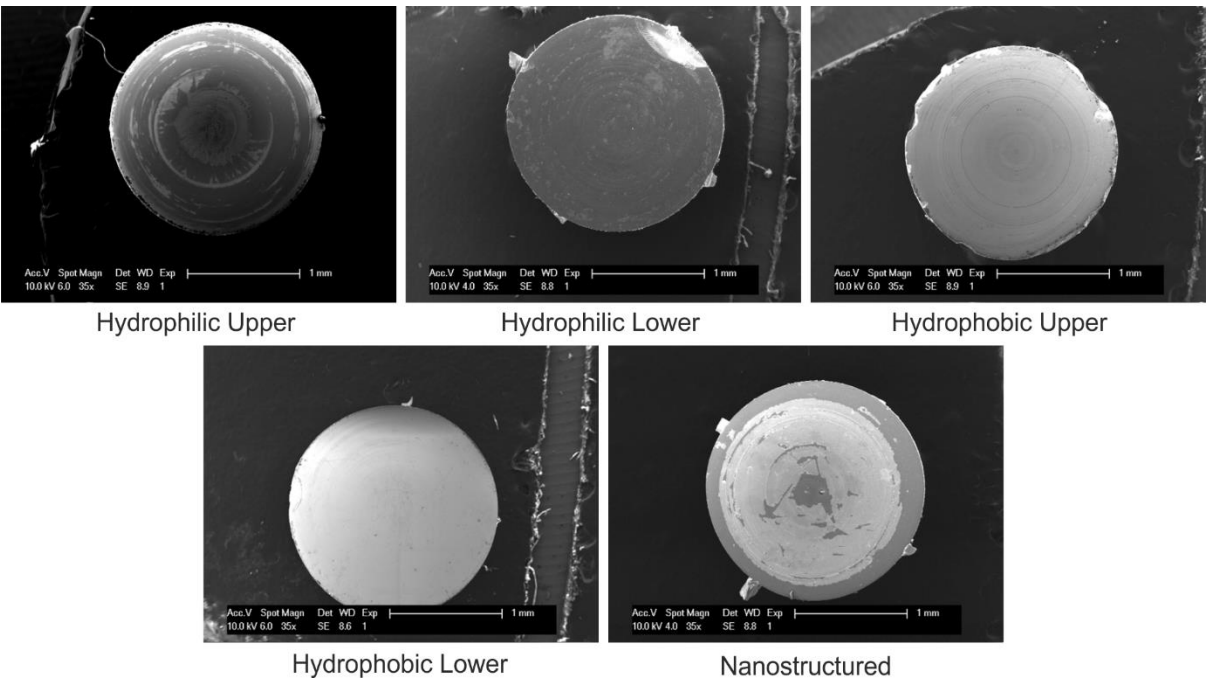


Figure 8.12 Scanning electron microscope images of the surfaces post testing.

On the hydrophilic upper sample some circumferential surface marks are seen. It is unclear whether this is due to some loss of material, and could not be clearly seen as material loss under SEM imaging so is likely to be very minimal if this is the case. EDX analysis was undertaken which showed that one area of the markings had a higher carbon content than unmarked reference. This could mean that some of the hydrophobic SAMS have transferred from the lower to upper disk. There is no evidence of material transfer of nickel from the nanostructured sample. There is some chipping to the edge of the sample which could be due to edge loading.

The hydrophobic upper also shows some circumferential surface marking, again on high magnification SEM imaging it was not obvious that these were due to material loss. There are two marks running across the surface probably due to handling of the sample on removal from the rig. Again some material loss is seen around the edge of the sample.

Both hydrophobic and hydrophilic lower samples look much less marked than the uppers however both have a small chip at the edge next to the struts which are required to hold them in the photoresist for fabrication.

The nanostructured sample shows some delamination of the nanostructured nickel coating around the edge of the sample. However the majority of cavity nanostructures were not destroyed by the testing.

There is no significant difference in wear based on the surface coating of the samples other than the nanostructured sample. The wear on the flat hydrophilic and hydrophobic silicon samples throughout testing is unlikely to have significantly impacted the observed friction as there was no correlation with the number of tests run using a given combination and the friction. However the nanostructured samples delamination could have led to a change in friction throughout the testing by changing the contact area and entrainment of debris into the contact, however friction remained relatively low throughout.

8.4 General Discussion and Conclusion

From the discussed experiments it is clear that the surface properties; hydrophobic (OTS coated silicon) or hydrophilic (silicon with oxidised surface) play a substantial role in the friction felt between sliding pairs on a MEMS scale. The most considerable difference is seen going from a

hydrophilic/hydrophilic pair to hydrophilic/hydrophobic. In the boundary and mixed lubrication regimes the reduction in friction is due to the presence of the SAM. It is not possible to conclusively say the origin of this change in friction in hydrodynamic conditions however it is clear that in this case the presence of surface nanobubbles are not the cause. The results are in keeping with the trend expected for slip on the hydrophobic surfaces and the subsequent friction reduction. If this is slip our results suggest that the origin is not based on a mechanism involving nanobubbles.

The difference between hydrophilic/hydrophobic and hydrophobic/hydrophobic is significant. This combination showed the lowest hydrodynamic friction but was higher in the boundary and mixed, possibly due to interaction of the two SAMs.

There is no evidence from our experiments that nanobubbles reduce friction by a slip mechanism. However this work does highlight the importance of SAMs to reduce friction throughout a range of sliding speeds in MEMS devices.

8.5 References

1. Scherge, M.; Li, X.; Schaefer, J. The effect of water on friction of MEMS. *Tribology Letters* **1999**, 6 (3-4), 215-220.
2. Srinivasan, U.; Houston, M. R.; Howe, R. T.; Maboudian, R. Alkyltrichlorosilane-based self-assembled monolayer films for stiction reduction in silicon micromachines. *Microelectromechanical Systems, Journal of* **1998**, 7 (2), 252-260.
3. Srinivasan, U.; Foster, J. D.; Habib, U.; Howe, R. T.; Maboudian, R.; Senft, D. C.; Dugger, M. T. *Lubrication of polysilicon micromechanisms with self-assembled monolayers*; Sandia National Labs., Albuquerque, NM (United States)1998.
4. Williams, J.; Le, H. Tribology and MEMS. *J. Phys. D: Appl. Phys.* **2006**, 39 (12), R201.
5. Ku, I.; Reddyhoff, T.; Wayte, R.; Choo, J.; Holmes, A.; Spikes, H. Lubrication of microelectromechanical devices using liquids of different viscosities. *Journal of Tribology* **2012**, 134 (1).
6. de Gennes, P.-G. On fluid/wall slippage. *Langmuir* **2002**, 18 (9), 3413-3414.
7. Ku, I.; Reddyhoff, T.; Choo, J.; Holmes, A.; Spikes, H. A novel tribometer for the measurement of friction in MEMS. *Tribology International* **2010**, 43 (5), 1087-1090.
8. Spikes, H. A. The half-wetted bearing. Part 1: extended Reynolds equation. *Proceedings of the Institution of Mechanical Engineers, Part J: Journal of Engineering Tribology* **2003**, 217 (1), 1-14.
9. Spikes, H. A. The half-wetted bearing. Part 2: potential application in low load contacts. *Proceedings of the Institution of Mechanical Engineers, Part J: Journal of Engineering Tribology* **2003**, 217 (1), 15-26.
10. Choo, J.; Spikes, H.; Ratoi, M.; Glovnea, R.; Forrest, A. Friction reduction in low-load hydrodynamic lubrication with a hydrophobic surface. *Tribology International* **2007**, 40 (2), 154-159.
11. Tretheway, D. C.; Meinhart, C. D. Apparent fluid slip at hydrophobic microchannel walls. *Phys. Fluids*. **2002**, 14 (3), L9-L12.
12. Tretheway, D. C.; Meinhart, C. D. A generating mechanism for apparent fluid slip in hydrophobic microchannels. *Phys. Fluids* **2004**, 16, 1509.
13. Hyväluoma, J.; Kunert, C.; Harting, J. Simulations of slip flow on nanobubble-laden surfaces. *J. Phys.: Condens. Matter* **2011**, 23 (18), 184106.

14. Bhushan, B.; Pan, Y.; Daniels, S. AFM characterization of nanobubble formation and slip condition in oxygenated and electrokinetically altered fluids. *J. Colloid Interface Sci.* **2013**, *392*, 105-116.
15. Maali, A.; Bhushan, B. Nanobubbles and their role in slip and drag. *J. Phys.: Condens. Matter* **2013**, *25* (18), 1-12.
16. Leong, J.; Reddyhoff, T.; Sinha, S.; Holmes, A.; Spikes, H. Hydrodynamic Friction Reduction in a MAC–Hexadecane Lubricated MEMS Contact. *Tribology Letters* **2013**, *49* (1), 217-225.
17. Ku, I. S. Y. Lubrication of high sliding silicon micromachines. Imperial College London 2010.
18. Bhushan, B.; Li, X. Micromechanical and tribological characterization of doped single-crystal silicon and polysilicon films for microelectromechanical systems devices. *J. Mater. Res.* **1997**, *12* (01), 54-63.
19. Bhardwaj, M.; Balani, K.; Balasubramaniam, R.; Pandey, S.; Agarwal, A. Effect of current density and grain refining agents on pulsed electrodeposition of nanocrystalline nickel. *Surf. Eng.* **2011**, *27* (9), 642-648.
20. Cameron, A. The viscosity wedge. *ASLE transactions* **1958**, *1* (2), 248-253.
21. Seddon, J. R.; Kooij, E. S.; Poelsema, B.; Zandvliet, H. J.; Lohse, D. Surface bubble nucleation stability. *Phys. Rev. Lett.* **2011**, *106* (5), 056101.
22. Lou, S.-T.; Ouyang, Z.-Q.; Zhang, Y.; Li, X.-J.; Hu, J.; Li, M.-Q.; Yang, F.-J. Nanobubbles on solid surface imaged by atomic force microscopy. *Journal of Vacuum Science & Technology B: Microelectronics and Nanometer Structures* **2000**, *18* (5), 2573-2575.
23. Hampton, M. A.; Donose, B. C.; Nguyen, A. V. Effect of alcohol–water exchange and surface scanning on nanobubbles and the attraction between hydrophobic surfaces. *J. Colloid Interface Sci.* **2008**, *325* (1), 267-274.
24. Scherge, M.; Schaefer, J. Microtribological investigations of stick/slip phenomena using a novel oscillatory friction and adhesion tester. *Tribology Letters* **1998**, *4* (1), 37-42.
25. Gao, J.; Luedtke, W.; Landman, U. Structures, solvation forces and shear of molecular films in a rough nano-confinement. *Tribology letters* **2000**, *9* (1-2), 3-13.
26. Attard, P. Nanobubbles and the hydrophobic attraction. *Adv. Colloid Interface Sci.* **2003**, *104* (1), 75-91.

Chapter 9: Conclusions and Future Work

9.1 Conclusion of Results Chapters

9.1.1 General Conclusion on Superhydrophobic Work Chapters 4, 5 & 6

This strand of investigation started by characterising the wetting properties of the hydrophobic close packed cavities in Chapter 4. This work highlighted some interesting and novel wetting phenomena, notably that the Petal effect could be achieved with 1 layer of structural hierarchy and the pinning effect of close packed cavities can give rise to dodecahedral drops. The large contact angle hysteresis indicated that water was penetrating into the cavities and therefore a method to actively replenish gas was required to maintain the Cassie state.

This led to the work in Chapter 5 where the surface was modified to insulate the top of the structure with a hydrophobic polymer and control of the surface using electrochemical methods. Dissolution of the gas from the cavities was confirmed by measuring the capacitance of the metal surface which increased with the expanding water/solid interface as gas was displaced. To top up the cavities as gas dissolved the surface was held a potential which led to hydrogen evolution. However once the surface was fully wetted the Cassie state could not be regained. This work is significant in the fact that it shows the double layer hierarchy used by Kim is not a necessity for the surface to replenish gas as it lost. The added functionality of non-visual measurement of the wetted area will prove a very useful feature in situations where large areas of superhydrophobic surface are used. Recent towing tank tests have not been able to measure this very important parameter, without which a good understanding of the drag results is not possible.

Chapter 6 sought to solve the problem of full dewetting by directing nucleation to the base of cavities using a hydrophobic polymer layer. The growth of gas within the cavity was modelled using finite element analysis to show that new gas would not leave the surface as bubbles if nucleation was directed to the base of the cavity. To create the cavities a high speed milling machine was used to make a hole into a layered construction of PTFE and steel. The full dewetting process was observed using a microscope and confirmed using capacitance measurements. This result shows that full dewetting is possible with the right surface design, a very important step toward the real

world application of superhydrophobic surfaces and has fulfilled the aims set out at the beginning of this Thesis.

9.1.2 General Conclusion on Nanobubble Work Chapters 7 & 8

The strand of work looking at nanobubbles started by using an atomic force microscope to investigate the nanoscale wetting properties of nanobubbles within hydrophobic cavities of different depths. This study has generated the first images of nanobubbles in cavities, previous work in the literature had only inferred the presence of nanobubbles in cavities using SAX which did not provide structural information. In most cases a high coverage of nanobubbles within the cavities could be achieved without methods required to generate nanobubbles on flat surfaces, such as the solvent exchange method. This is a considerable advantage to those wishing to work with nanobubbles. The nanobubbles were stable to dissolution, persisting for at least 7 hours and also stable to contact mode imaging. Although the motivations to study the nanoscale wetting of this surface were related to slip and drag reductions these surfaces could find use in any area in which uniformly sized nanobubbles are required.

Using the 0.2 d surface generated from the work in chapter 7, the frictional properties were compared with and without nanobubbles present and also compared with flat hydrophilic and hydrophobic surfaces with and without nanobubbles present using a MEMS tribometer. The stribek curves showed that the presence of nanobubbles had no effect on friction, a negative but significant result. This study did highlight a substantial reduction in friction by using hydrophobic SAMS on the bearing surfaces which had not previously been demonstrated using these tribological conditions.

9.2 Future Work

The work in both strands of this thesis has led to more ideas and questions to be answered. The most important and interesting topics of future work are listed here.

9.2.1 Superhydrophobic Surfaces

9.2.1.1 Full Dewetting of Cavities in Close Packed Array

Further work based on Chapter 6 Full Dewetting of a Cavity should initially focus on the dewetting of an array of close packed cavities. According to the theory using the same diameter cavities with a 50 μm spacing between cavities would lead to a 300 μm slip length, capable reducing drag on ships. The testing would take on a similar methodology used in Chapter 6 to observe the dewetting

process. The use of an optical microscope capable of generating three dimensional images could add to the understanding of the dewetting process.

9.2.1.2 Measurement of Slip Over Close Packed Array of Cavities

Once it has been shown that an array of cavities can fully dewet and maintain the dewetted state it should be a priority to measure the slip length achieved using this surface. Measurement of the slip length in laminar flow conditions could be carried out using the cone and plate rheometry technique¹, measurement of pressure drop² or an inbuilt shear measurement device³. The dewetting of the surface should also be tested under flow conditions. Measurement of the slip length will allow quantification of drag reduction in a range of laminar flow conditions. Measurement of the drag reduction in turbulent flow conditions should also be measured, currently this is only possible using the inbuilt shear measurement technique.

9.2.1.3 Measurement of dissolution using capacitance measurement

Using the capacitance measurement technique developed in chapter 5 the dissolution of gas from the larger 500 μm diameter cavities should be investigated under a range of conditions. The effect of fluid flow past a superhydrophobic surface has not been investigated.

9.2.1.4 Production of large area surfaces at low cost

Methods by which to fabricate large areas of the surface which do not rely on machining of individual cavities should also be investigated. The current method of machining individual holes is not suitable for large areas due to the length of time it would take. Using a master from which features are moulded could offer a fast and cheap way to make large areas of surface quickly.

9.2.2 Nanobubbles

9.2.2.1 Investigation of Extreme Curvature

As discussed in Chapter 7 the Laplace pressure calculated from the curvature of nanobubbles found within some of the cavities predicts an absolute pressure of less than zero. Whether this is an imaging artefact or if it is the true curvature is currently unknown. Recently Walczyk et al. have shown the evolution of the nanobubble profile with imaging force using 'peakforce tapping mode' (an imaging mode proprietary to the AFM manufacturer Bruker) where the force with which the surface is imaged is held constant⁴. By imaging the nanobubbles under a range of peak force loads

the relationship between imaging conditions and nanobubbles profile would be elucidated. This would help to understand if the profiles in the study in Chapter 7 are correct.

9.2.2.2 Electrochemically Generated Hydrogen Nanobubbles

Zhang et al. have demonstrated the generation of nanobubbles containing hydrogen gas using electrolysis⁵. A similar experiment should be done using the surfaces fabricated in Chapter 7 to see if good nanobubble coverage can be established within the cavities from a degassed environment.

9.2.2.3 Nanobubble Adhesion

Nanobubbles are thought to be the cause of the long range hydrophobic attraction, where they form capillary bridges between the surfaces which leads to a large attractive force between surfaces; this can be problematic in a range of situations. Chapter 7 showed that the nanobubbles in cavities do not protrude above the tops of the cavities and therefore would not be able to form capillary bridges. This could be useful as a surface which is hydrophobic but does not suffer from the long range hydrophobic attraction. This would be best tested using a surface force apparatus.

9.2.2.4 Nanobubble templated electrodeposition

The nanobubbles within the cavities could be used as a template around which further metal deposition is made. This could lead to a broader range of surface features accessible through non lithographic means.

9.2.2.5 Nanobubble Drainage Force

The work in chapter 8 showed that there was no difference in friction in the MEMS tribometer between surfaces with and without nanobubbles present. To have a higher sensitivity one method which could measure slip could be a drainage force experiment. Here an AFM tip with a sphere attached is held close and moved through the water. The lateral displacement of the cantilever can be measured from which the degree of slip can be evaluated. This technique would provide much milder conditions for the nanobubbles as there would be no contact with another surface and shear rate would be much lower. One could also easily image the surface before and after the test to observe changes in the nanobubbles.

9.3 References

1. Lee, C.; Choi, C.-H.; Kim, C.-J. C. Structured surfaces for a giant liquid slip. *Phys. Rev. Lett.* **2008**, *101* (6), 064501.
2. Choi, C.-H.; Ulmanella, U.; Kim, J.; Ho, C.-M.; Kim, C.-J. Effective slip and friction reduction in nanogated superhydrophobic microchannels. *Phys. Fluids*. **2006**, *18* (8), 087105.

3. Sun, G.; Park, H.; Kim, C.-J. Development of a Miniature Shear Sensor for Direct Comparison of Skin-Friction Drags.
4. Walczyk, W.; Schön, P. M.; Schönherr, H. The effect of PeakForce tapping mode AFM imaging on the apparent shape of surface nanobubbles. *J. Phys.: Condens. Matter* **2013**, 25 (18), 184005.
5. Zhang, L.; Zhang, Y.; Zhang, X.; Li, Z.; Shen, G.; Ye, M.; Fan, C.; Fang, H.; Hu, J. Electrochemically controlled formation and growth of hydrogen nanobubbles. *Langmuir* **2006**, 22 (19), 8109-8113.

List of References

Abdelsalam, M. E.; Bartlett, P. N.; Kelf, T.; Baumberg, J. Wetting of regularly structured gold surfaces. *Langmuir* **2005**, *21* (5), 1753-1757.

Agrawal, A.; Park, J.; Ryu, D. Y.; Hammond, P. T.; Russell, T. P.; McKinley, G. H. Controlling the location and spatial extent of nanobubbles using hydrophobically nanopatterned surfaces. *Nano Lett.* **2005**, *5* (9), 1751-1756.

Aljallis, E.; Sarshar, M. A.; Datla, R.; Sikka, V.; Jones, A.; Choi, C.-H. Experimental study of skin friction drag reduction on superhydrophobic flat plates in high Reynolds number boundary layer flow. *Phys. Fluids* **2013**, *25*, 025103.

Attard, P. Nanobubbles and the hydrophobic attraction. *Adv. Colloid Interface Sci.* **2003**, *104* (1), 75-91.

Bain, C. D.; Whitesides, G. M. Formation of monolayers by the coadsorption of thiols on gold: variation in the length of the alkyl chain. *J. Am. Chem. Soc.* **1989**, *111* (18), 7164-7175.

Barthlott, W.; Neinhuis, C. Purity of the sacred lotus, or escape from contamination in biological surfaces. *Planta* **1997**, *202* (1), 1-8.

Bartlett, P. N. Electrodeposition of Nanostructured Films Using Self-Organizing Templates. *Interface-Electrochemical Society* 2004, *13* (4), 28-33.

Bartlett, P.; Baumberg, J.; Birkin, P. R.; Ghanem, M.; Netti, M. Highly ordered macroporous gold and platinum films formed by electrochemical deposition through templates assembled from submicron diameter monodisperse polystyrene spheres. *Chem. Mater.* **2002**, *14* (5), 2199-2208.

Bartlett, P. N.; Birkin, P. R.; Ghanem, M. A. Electrochemical deposition of macroporous platinum, palladium and cobalt films using polystyrene latex sphere templates. *Chem. Commun.* **2000**, (17), 1671-1672.

Bartlett, P. N.; Birkin, P. R.; Ghanem, M. A.; Toh, C.-S. Electrochemical syntheses of highly ordered macroporous conducting polymers grown around self-assembled colloidal templates. *J. Mater. Chem.* **2001**, *11* (3), 849-853.

Baudry, J.; Charlaix, E.; Tonck, A.; Mazuyer, D. Experimental evidence for a large slip effect at a nonwetting fluid-solid interface. *Langmuir* **2001**, *17* (17), 5232-5236.

Bibliography

Ben-Ali, S.; Cook, D. A.; Evans, S. A.; Thienpont, A.; Bartlett, P. N.; Kuhn, A. Electrocatalysis with monolayer modified highly organized macroporous electrodes. *Electrochem. Commun.* **2003**, *5* (9), 747-751.

Bhardwaj, M.; Balani, K.; Balasubramaniam, R.; Pandey, S.; Agarwal, A. Effect of current density and grain refining agents on pulsed electrodeposition of nanocrystalline nickel. *Surf. Eng.* **2011**, *27* (9), 642-648.

Bhushan, B.; Chae Jung, Y. Wetting study of patterned surfaces for superhydrophobicity. *Ultramicroscopy* **2007**, *107* (10), 1033-1041.

Bhushan, B.; Her, E. K. Fabrication of superhydrophobic surfaces with high and low adhesion inspired from rose petal. *Langmuir* **2010**, *26* (11), 8207-8217.

Bhushan, B.; Li, X. Micromechanical and tribological characterization of doped single-crystal silicon and polysilicon films for microelectromechanical systems devices. *J. Mater. Res.* **1997**, *12* (01), 54-63.

Bhushan, B.; Nosonovsky, M. The rose petal effect and the modes of superhydrophobicity. *Phil. Trans. R. Soc. A* **2010**, *368* (1929), 4713-4728.

Bhushan, B.; Pan, Y.; Daniels, S. AFM characterization of nanobubble formation and slip condition in oxygenated and electrokinetically altered fluids. *J. Colloid Interface Sci.* **2013**, *392*, 105-116.

Bico, J.; Marzolin, C.; Quéré, D. Pearl drops. *EPL* **1999**, *47* (2), 220.

Birembaut, F.; Perney, N.; Pechstedt, K.; Bartlett, P. N.; Russell, A. E.; Baumberg, J. J. Sharp - Cornered Liquid Drops by Wetting of Nanoscale Features. *small* **2008**, *4* (12), 2140-2142.

Bobji, M. S.; Kumar, S. V.; Asthana, A.; Govardhan, R. N. Underwater sustainability of the "Cassie" state of wetting. *Langmuir* **2009**, *25* (20), 12120-12126.

Bonaccorso, E.; Butt, H.-J.; Craig, V. S. Surface roughness and hydrodynamic boundary slip of a Newtonian fluid in a completely wetting system. *Phys. Rev. Lett.* **2003**, *90* (14), 144501.

Boreyko, J. B.; Chen, C.-H. Restoring superhydrophobicity of lotus leaves with vibration-induced dewetting. *Phys. Rev. Lett.* **2009**, *103* (17), 174502.

Borkent, B. M.; Dammer, S. M.; Schönherr, H.; Vancso, G. J.; Lohse, D. Superstability of surface nanobubbles. *Phys. Rev. Lett.* **2007**, *98* (20), 204502.

- Borkent, B. M.; de Beer, S.; Mugele, F.; Lohse, D. On the shape of surface nanobubbles. *Langmuir* **2009**, *26* (1), 260-268.
- Brenner, M. P.; Lohse, D. Dynamic equilibrium mechanism for surface nanobubble stabilization. *Phys. Rev. Lett.* **2008**, *101* (21), 214505.
- Brussieux, C.; Viers, P.; Roustan, H.; Rakib, M. Controlled electrochemical gas bubble release from electrodes entirely and partially covered with hydrophobic materials. *Electrochim. Acta* **2011**, *56* (20), 7194-7201.
- Cahn, J. W.; Hilliard, J. E. Free energy of a nonuniform system. I. Interfacial free energy. *The Journal of chemical physics* **1958**, *28* (2), 258-267.
- Cameron, A. The viscosity wedge. *ASLE transactions* **1958**, *1* (2), 248-253.
- Cao, L.; Hu, H.-H.; Gao, D. Design and fabrication of micro-textures for inducing a superhydrophobic behavior on hydrophilic materials. *Langmuir* **2007**, *23* (8), 4310-4314.
- Cao, L.; Jones, A. K.; Sikka, V. K.; Wu, J.; Gao, D. Anti-icing superhydrophobic coatings. *Langmuir* **2009**, *25* (21), 12444-12448.
- Cassie, A.; Baxter, S. Wettability of porous surfaces. *Trans. Faraday Society* **1944**, *40*, 546-551.
- Checco, A.; Hofmann, T.; DiMasi, E.; Black, C. T.; Ocko, B. M. Morphology of air nanobubbles trapped at hydrophobic nanopatterned surfaces. *Nano Lett.* **2010**, *10* (4), 1354-1358.
- Choi, C.-H.; Kim, C.-J. Large slip of aqueous liquid flow over a nanoengineered superhydrophobic surface. *Phys. Rev. Lett.* **2006**, *96* (6), 066001.
- Choi, C.-H.; Ulmanella, U.; Kim, J.; Ho, C.-M.; Kim, C.-J. Effective slip and friction reduction in nanogated superhydrophobic microchannels. *Phys. Fluids*. **2006**, *18* (8), 087105.
- Choi, C.-H.; Westin, K. J. A.; Breuer, K. S. Apparent slip flows in hydrophilic and hydrophobic microchannels. *Phys. Fluids* **2003**, *15*, 2897.
- Choo, J.; Glovnea, R.; Forrest, A.; Spikes, H. A low friction bearing based on liquid slip at the wall. *Journal of Tribology* **2007**, *129* (3), 611-620.

Bibliography

Choo, J.; Spikes, H.; Ratoi, M.; Glovnea, R.; Forrest, A. Friction reduction in low-load hydrodynamic lubrication with a hydrophobic surface. *Tribology International* **2007**, *40* (2), 154-159.

Cottin-Bizonne, C.; Barentin, C.; Charlaix, É.; Bocquet, L.; Barrat, J.-L. Dynamics of simple liquids at heterogeneous surfaces: Molecular-dynamics simulations and hydrodynamic description. *The European Physical Journal E* **2004**, *15* (4), 427-438.

Cottin-Bizonne, C.; Jurine, S.; Baudry, J.; Crassous, J.; Restagno, F.; Charlaix, E. Nanorheology: An investigation of the boundary condition at hydrophobic and hydrophilic interfaces. *The European Physical Journal E* **2002**, *9* (1), 47-53.

Craig, V. S. J. Very small bubbles at surfaces—the nanobubble puzzle. *Soft Matter* **2011**, *7* (1), 40-48.

Dammer, S. M.; Lohse, D. Gas enrichment at liquid-wall interfaces. *Phys. Rev. Lett.* **2006**, *96* (20), 206101.

Davis, A. M.; Lauga, E. Geometric transition in friction for flow over a bubble mattress. *Phys. Fluids* **2009**, *21*, 011701.

Day, M. A. The no-slip condition of fluid dynamics. *Erkenntnis* **1990**, *33* (3), 285-296.

de Gennes, P.-G. On fluid/wall slippage. *Langmuir* **2002**, *18* (9), 3413-3414.

Debenedetti, P. G. *Metastable liquids: concepts and principles*; Princeton University Press 1996.

Dhariwal, R.; Flockhart, S. Finite element investigation into proposed bearing mechanism for a fluid driven micro actuator. *Microsystem technologies* **1999**, *5* (4), 200-204.

Dhindsa, M. S.; Smith, N. R.; Heikenfeld, J.; Rack, P. D.; Fowlkes, J. D.; Doktycz, M. J.; Melechko, A. V.; Simpson, M. L. Reversible electrowetting of vertically aligned superhydrophobic carbon nanofibers. *Langmuir* **2006**, *22* (21), 9030-9034.

Ducker, W. A. Contact angle and stability of interfacial nanobubbles. *Langmuir* **2009**, *25* (16), 8907-8910.

Epstein, A. H. Millimeter-scale, MEMS gas turbine engines. In *Proceedings of ASME Turbo Expo*, 2003, pp 1-28.

Epstein, P.; Plesset, M. On the Stability of Gas Bubbles in Liquid - Gas Solutions. *The Journal of Chemical Physics* **1950**, *18*, 1505.

Erbil, H. Y.; Demirel, A. L.; Avci, Y.; Mert, O. Transformation of a simple plastic into a superhydrophobic surface. *Science* **2003**, *299* (5611), 1377-1380.

Extrand, C. Criteria for ultralyophobic surfaces. *Langmuir* **2004**, *20* (12), 5013-5018.

Feng, L.; Zhang, Y.; Xi, J.; Zhu, Y.; Wang, N.; Xia, F.; Jiang, L. Petal effect: a superhydrophobic state with high adhesive force. *Langmuir* **2008**, *24* (8), 4114-4119.

Finger, A.; Johannsmann, D. Hemispherical nanobubbles reduce interfacial slippage in simple liquids. *PCCP* **2011**, *13* (40), 18015-18022.

Furmidge, C. Studies at phase interfaces. I. The sliding of liquid drops on solid surfaces and a theory for spray retention. *Journal of Colloid Science* **1962**, *17* (4), 309-324.

Gao, J.; Luedtke, W.; Landman, U. Structures, solvation forces and shear of molecular films in a rough nano-confinement. *Tribology letters* **2000**, *9* (1-2), 3-13.

Goldstein, S. Fluid mechanics in the first half of this century. *Annu. Rev. Fluid. Mech.* **1969**, *1* (1), 1-29.

Govardhan, R.; Srinivas, G.; Asthana, A.; Bobji, M. Time dependence of effective slip on textured hydrophobic surfaces. *Phys. Fluids*. **2009**, *21* (5), 052001.

Hampton, M.; Nguyen, A. Nanobubbles and the nanobubble bridging capillary force. *Adv. Colloid Interface Sci.* **2010**, *154* (1), 30-55.

Hampton, M. A.; Donose, B. C.; Nguyen, A. V. Effect of alcohol–water exchange and surface scanning on nanobubbles and the attraction between hydrophobic surfaces. *J. Colloid Interface Sci.* **2008**, *325* (1), 267-274.

Hampton, M. A.; Donose, B. C.; Taran, E.; Nguyen, A. V. Effect of nanobubbles on friction forces between hydrophobic surfaces in water. *J. Colloid Interface Sci.* **2009**, *329* (1), 202-207.

Hendy, S.; Lund, N. Effective slip lengths for flows over surfaces with nanobubbles: The effects of finite slip. *J. Phys.: Condens. Matter* **2009**, *21* (14), 144202.

Holmberg, M.; Kühle, A.; Garnæs, J.; Mørch, K. A.; Boisen, A. Nanobubble trouble on gold surfaces. *Langmuir* **2003**, *19* (25), 10510-10513.

Bibliography

- Hyv luoma, J.; Kunert, C.; Harting, J. Simulations of slip flow on nanobubble-laden surfaces. *J. Phys.: Condens. Matter* **2011**, *23* (18), 184106.
- Ishida, N.; Inoue, T.; Miyahara, M.; Higashitani, K. Nano bubbles on a hydrophobic surface in water observed by tapping-mode atomic force microscopy. *Langmuir* **2000**, *16* (16), 6377-6380.
- Jin, M.; Feng, X.; Feng, L.; Sun, T.; Zhai, J.; Li, T.; Jiang, L. Superhydrophobic aligned polystyrene nanotube films with high adhesive force. *Adv. Mater.* **2005**, *17* (16), 1977-1981.
- Krupenkin, T. N.; Taylor, J. A.; Wang, E. N.; Kolodner, P.; Hodes, M.; Salamon, T. R. Reversible wetting-dewetting transitions on electrically tunable superhydrophobic nanostructured surfaces. *Langmuir* **2007**, *23* (18), 9128-9133.
- Ku, I.; Reddyhoff, T.; Choo, J.; Holmes, A.; Spikes, H. A novel tribometer for the measurement of friction in MEMS. *Tribology International* **2010**, *43* (5), 1087-1090.
- Ku, I.; Reddyhoff, T.; Wayte, R.; Choo, J.; Holmes, A.; Spikes, H. Lubrication of microelectromechanical devices using liquids of different viscosities. *Journal of Tribology* **2012**, *134* (1).
- Ku, I. S. Y. Lubrication of high sliding silicon micromachines. Imperial College London 2010.
- Kwon, H.-M.; Paxson, A. T.; Varanasi, K. K.; Patankar, N. A. Rapid deceleration-driven wetting transition during pendant drop deposition on superhydrophobic surfaces. *Phys. Rev. Lett.* **2011**, *106* (3), 036102.
- Laplace, P. S. *Traite de m canique c leste*; l'Imprimerie de Crapelet 1805; Vol. 4.
- Lau, K. K.; Bico, J.; Teo, K. B.; Chhowalla, M.; Amaratunga, G. A.; Milne, W. I.; McKinley, G. H.; Gleason, K. K. Superhydrophobic carbon nanotube forests. *Nano Lett.* **2003**, *3* (12), 1701-1705.
- Lauga, E.; Stone, H. A. Effective slip in pressure-driven Stokes flow. *J. Fluid Mech.* **2003**, *489* (8), 55-77.
- Lee, C.; Choi, C.-H.; Kim, C.-J. C. Structured surfaces for a giant liquid slip. *Phys. Rev. Lett.* **2008**, *101* (6), 064501.
- Lee, C.; Kim, C.-J. Underwater restoration and retention of gases on superhydrophobic surfaces for drag reduction. *Phys. Rev. Lett.* **2011**, *106* (1), 014502.
- Lee, C.; Kim, C.-J. Wetting and Active Dewetting Processes of Hierarchically Constructed Superhydrophobic Surfaces Fully Immersed in Water. *Journal of Microelectromechanical Systems* **2012**, *21* (3), 712-720.

Lee, C.; Kim, C.-J. C. Maximizing the giant liquid slip on superhydrophobic microstructures by nanostructuring their sidewalls. *Langmuir* **2009**, *25* (21), 12812-12818.

Leong, J.; Reddyhoff, T.; Sinha, S.; Holmes, A.; Spikes, H. Hydrodynamic Friction Reduction in a MAC–Hexadecane Lubricated MEMS Contact. *Tribology Letters* **2013**, *49* (1), 217-225.

Ljunggren, S.; Eriksson, J. C. The lifetime of a colloid-sized gas bubble in water and the cause of the hydrophobic attraction. *Colloids and Surfaces A: Physicochemical and Engineering Aspects* **1997**, *129*, 151-155.

Lloyd, B. P.; Bartlett, P. N.; Wood, R. J. Wetting of Surfaces made of Hydrophobic Cavities. *Langmuir* **2015**, *31* (34), 9325-9330.

Lou, S.-T.; Ouyang, Z.-Q.; Zhang, Y.; Li, X.-J.; Hu, J.; Li, M.-Q.; Yang, F.-J. Nanobubbles on solid surface imaged by atomic force microscopy. *Journal of Vacuum Science & Technology B: Microelectronics and Nanometer Structures* **2000**, *18* (5), 2573-2575.

Lv, P.; Xue, Y.; Shi, Y.; Lin, H.; Duan, H. Metastable states and wetting transition of submerged superhydrophobic structures. *Phys. Rev. Lett.* **2014**, *112* (19), 196101.

Maali, A.; Bhushan, B. Nanobubbles and their role in slip and drag. *J. Phys.: Condens. Matter* **2013**, *25* (18), 1-12.

McHale, J. P.; Garimella, S. V. Nucleate boiling from smooth and rough surfaces–Part 1: Fabrication and characterization of an optically transparent heater–sensor substrate with controlled surface roughness. *Exp. Therm Fluid Sci.* **2013**, *44*, 456-467.

Nosonovskii, M.; Bhushan, B. *Multiscale dissipative mechanisms and hierarchical surfaces: friction, superhydrophobicity, and biomimetics*; Springer 2008.

Orazem, M. E.; Tribollet, B. *Electrochemical impedance spectroscopy*; John Wiley & Sons, 2011.

Park, H.; Sun, G.; Kim, C.-J. C. In *Turbulent drag reduction on superhydrophobic surfaces confirmed by built-in shear sensing*, Micro Electro Mechanical Systems (MEMS), 2013 IEEE 26th International Conference on, 2013; IEEE, pp 1183-1186.

Parker, J. L.; Claesson, P. M.; Attard, P. Bubbles, cavities, and the long-ranged attraction between hydrophobic surfaces. *The Journal of Physical Chemistry* **1994**, *98* (34), 8468-8480.

Bibliography

- Pashley, R. Effect of degassing on the formation and stability of surfactant-free emulsions and fine teflon dispersions. *The Journal of Physical Chemistry B* **2003**, 107 (7), 1714-1720.
- Patankar, N. A. Hydrophobicity of Surfaces with Cavities: Making Hydrophobic Substrates from Hydrophilic Materials? *J. Adhesion Sci. Technol.* **2009**, 23 (3), 413-433.
- Patankar, N. A. Mimicking the lotus effect: influence of double roughness structures and slender pillars. *Langmuir* **2004**, 20 (19), 8209-8213.
- Pit, R.; Hervet, H.; Leger, L. Direct experimental evidence of slip in hexadecane: solid interfaces. *Phys. Rev. Lett.* **2000**, 85 (5), 980.
- Poetes, R.; Holtzmann, K.; Franze, K.; Steiner, U. Metastable underwater superhydrophobicity. *Phys. Rev. Lett.* **2010**, 105 (16), 166104.
- Qu, M.; Zhang, B.; Song, S.; Chen, L.; Zhang, J.; Cao, X. Fabrication of Superhydrophobic Surfaces on Engineering Materials by a Solution - Immersion Process. *Adv. Funct. Mater.* **2007**, 17 (4), 593-596.
- Rothstein, J. P. Slip on superhydrophobic surfaces. *Annu. Rev. Fluid. Mech.* **2010**, 42, 89-109.
- Scherge, M.; Li, X.; Schaefer, J. The effect of water on friction of MEMS. *Tribology Letters* **1999**, 6 (3-4), 215-220.
- Scherge, M.; Schaefer, J. Microtribological investigations of stick/slip phenomena using a novel oscillatory friction and adhesion tester. *Tribology Letters* **1998**, 4 (1), 37-42.
- Seddon, J. R.; Kooij, E. S.; Poelsema, B.; Zandvliet, H. J.; Lohse, D. Surface bubble nucleation stability. *Phys. Rev. Lett.* **2011**, 106 (5), 056101.
- Seddon, J. R.; Zandvliet, H. J.; Lohse, D. Knudsen gas provides nanobubble stability. *Phys. Rev. Lett.* **2011**, 107 (11), 116101.
- Seo, H.; Yoo, M.; Jeon, S. Influence of nanobubbles on the adsorption of nanoparticles. *Langmuir* **2007**, 23 (4), 1623-1625.
- Shateri Khalil-Abad, M.; Yazdanshenas, M. E. Superhydrophobic antibacterial cotton textiles. *J. Colloid Interface Sci.* **2010**, 351 (1), 293-298.
- Simonsen, A. C.; Hansen, P. L.; Klösgen, B. Nanobubbles give evidence of incomplete wetting at a hydrophobic interface. *J. Colloid Interface Sci.* **2004**, 273 (1), 291-299.

Spikes, H. A. The half-wetted bearing. Part 1: extended Reynolds equation. *Proceedings of the Institution of Mechanical Engineers, Part J: Journal of Engineering Tribology* **2003**, 217 (1), 1-14.

Spikes, H. A. The half-wetted bearing. Part 2: potential application in low load contacts. *Proceedings of the Institution of Mechanical Engineers, Part J: Journal of Engineering Tribology* **2003**, 217 (1), 15-26.

Srinivasan, U.; Foster, J. D.; Habib, U.; Howe, R. T.; Maboudian, R.; Senft, D. C.; Dugger, M. T. *Lubrication of polysilicon micromechanisms with self-assembled monolayers*; Sandia National Labs., Albuquerque, NM (United States)1998.

Srinivasan, U.; Houston, M. R.; Howe, R. T.; Maboudian, R. Alkyltrichlorosilane-based self-assembled monolayer films for stiction reduction in silicon micromachines. *Microelectromechanical Systems, Journal of* **1998**, 7 (2), 252-260.

Steinberger, A.; Cottin-Bizonne, C.; Kleimann, P.; Charlaix, E. High friction on a bubble mattress. *Nature Materials* **2007**, 6 (9), 665-668.

Steinberger, A.; Cottin-Bizonne, C.; Kleimann, P.; Charlaix, E. Nanoscale flow on a bubble mattress: Effect of surface elasticity. *Phys. Rev. Lett.* **2008**, 100 (13), 134501.

Sun, G.; Park, H.; Kim, C.-J. Development of a Miniature Shear Sensor for Direct Comparison of Skin-Friction Drags.

Switkes, M.; Ruberti, J. Rapid cryofixation/freeze fracture for the study of nanobubbles at solid-liquid interfaces. *Appl. Phys. Lett.* **2004**, 84 (23), 4759-4761.

Thompson, P. A.; Troian, S. M. A general boundary condition for liquid flow at solid surfaces. *Nature* **1997**, 389 (6649), 360-362.

Trasatti, S.; Petrii, O. Real surface area measurements in electrochemistry. *Pure Appl. Chem.* **1991**, 63 (5), 711-734.

Tretheway, D.; Stone, S.; Meinhart, C. Effects of Absolute Pressure and Dissolved Gasses on Apparent Fluid Slip in Hydrophobic Microchannels. In *APS Division of Fluid Dynamics Meeting Abstracts*, 2004; Vol. 1, pp 561-564.

Tretheway, D. C.; Meinhart, C. D. Apparent fluid slip at hydrophobic microchannel walls. *Phys. Fluids.* **2002**, 14 (3), L9-L12.

Bibliography

Tretheway, D. C.; Meinhart, C. D. A generating mechanism for apparent fluid slip in hydrophobic microchannels. *Phys. Fluids* **2004**, *16*, 1509.

Tuberquia, J. C.; Song, W. S.; Jennings, G. K. Investigating the Superhydrophobic Behavior for Underwater Surfaces Using Impedance-Based Methods. *Anal. Chem.* **2011**, *83* (16), 6184-6190.

Tyrrell, J. W. G.; Attard, P. Images of nanobubbles on hydrophobic surfaces and their interactions. *Phys. Rev. Lett.* **2001**, *87* (17).

van Limbeek, M. A.; Seddon, J. R. Surface nanobubbles as a function of gas type. *Langmuir* **2011**, *27* (14), 8694-8699.

Vincent, J. Superhydrophobic spray NeverWet enters US market in a \$20 can. *The Independant*, 21/06/2013, 2013.

Walczyk, W.; Schön, P. M.; Schönherr, H. The effect of PeakForce tapping mode AFM imaging on the apparent shape of surface nanobubbles. *J. Phys.: Condens. Matter* **2013**, *25* (18), 184005.

Wang, S.; Jiang, L. Definition of superhydrophobic states. *Adv. Mater.* **2007**, *19* (21), 3423-3424.

Wang, Y.; Bhushan, B. Boundary slip and nanobubble study in micro/nanofluidics using atomic force microscopy. *Soft Matter* **2010**, *6* (1), 29-66.

Wang, Y.; Bhushan, B.; Zhao, X. Improved nanobubble immobility induced by surface structures on hydrophobic surfaces. *Langmuir* **2009**, *25* (16), 9328-9336.

Wang, Y.; Bhushan, B.; Zhao, X. Nanoindents produced by nanobubbles on ultrathin polystyrene films in water. *Nanotechnology* **2009**, *20* (4), 045301.

Weijs, J. H.; Lohse, D. Why surface nanobubbles live for hours. *Phys. Rev. Lett.* **2013**, *110* (5), 054501.

Wenzel, R. N. Resistance of solid surfaces to wetting by water. *Industrial & Engineering Chemistry* **1936**, *28* (8), 988-994.

Williams, J.; Le, H. Tribology and MEMS. *J. Phys. D: Appl. Phys.* **2006**, *39* (12), R201.

Wu, Z.; Chen, H.; Dong, Y.; Mao, H.; Sun, J.; Chen, S.; Craig, V. S.; Hu, J. Cleaning using nanobubbles: defouling by electrochemical generation of bubbles. *J. Colloid Interface Sci.* **2008**, *328* (1), 10-14.

- Xu, M.; Sun, G.; Kim, C.-J. Infinite Lifetime of Underwater Superhydrophobic States. *Phys. Rev. Lett.* **2014**, *113* (13), 136103.
- Xue-Hua, Z.; Gang, L.; Zhi-Hua, W.; Xiao-Dong, Z.; Jun, H. Effect of temperature on the morphology of nanobubbles at mica/water interface. *Chinese Physics* **2005**, *14* (9), 1774.
- Yang, S.; Dammer, S. M.; Bremond, N.; Zandvliet, H. J.; Kooij, E. S.; Lohse, D. Characterization of nanobubbles on hydrophobic surfaces in water. *Langmuir* **2007**, *23* (13), 7072-7077.
- Yang, S.; Tsai, P.; Kooij, E. S.; Prosperetti, A.; Zandvliet, H. J.; Lohse, D. Electrolytically generated nanobubbles on highly orientated pyrolytic graphite surfaces. *Langmuir* **2009**, *25* (3), 1466-1474.
- Ybert, C.; Barentin, C.; Cottin-Bizonne, C.; Joseph, P.; Bocquet, L. Achieving large slip with superhydrophobic surfaces: Scaling laws for generic geometries. *Phys. Fluids* **2007**, *19*, 123601.
- Young, T. An essay on the cohesion of fluids. *Philos. Trans. R. Soc. London* **1805**, *95*, 65-87.
- Zhang, F.; Zhao, L.; Chen, H.; Xu, S.; Evans, D. G.; Duan, X. Corrosion resistance of superhydrophobic layered double hydroxide films on aluminum. *Angew. Chem. Int. Ed.* **2008**, *47* (13), 2466-2469.
- Zhang, J.; Li, J.; Han, Y. Superhydrophobic PTFE surfaces by extension. *Macromol. Rapid Commun.* **2004**, *25* (11), 1105-1108.
- Zhang, L.; Zhang, Y.; Zhang, X.; Li, Z.; Shen, G.; Ye, M.; Fan, C.; Fang, H.; Hu, J. Electrochemically controlled formation and growth of hydrogen nanobubbles. *Langmuir* **2006**, *22* (19), 8109-8113.
- Zhang, X. H. Quartz crystal microbalance study of the interfacial nanobubbles. *PCCP* **2008**, *10* (45), 6842-6848.
- Zhang, X. H.; Khan, A.; Ducker, W. A. A nanoscale gas state. *Phys. Rev. Lett.* **2007**, *98* (13), 136101.
- Zhang, X. H.; Li, G.; Maeda, N.; Hu, J. Removal of induced nanobubbles from water/graphite interfaces by partial degassing. *Langmuir* **2006**, *22* (22), 9238-9243.
- Zhang, X. H.; Maeda, N.; Craig, V. S. Physical properties of nanobubbles on hydrophobic surfaces in water and aqueous solutions. *Langmuir* **2006**, *22* (11), 5025-5035.

Bibliography

Zhang, X. H.; Quinn, A.; Ducker, W. A. Nanobubbles at the interface between water and a hydrophobic solid. *Langmuir* **2008**, *24* (9), 4756-4764.

Zhu, X.; Zhang, C.; Liu, X.; Hansen, O.; Xiao, S.; Mortensen, N. A.; Zi, J. Evaporation of Water Droplets on “Lock-and-Key” Structures with Nanoscale Features. *Langmuir* **2012**, *28* (25), 9201-9205.

Zhu, Y.; Granick, S. Rate-dependent slip of Newtonian liquid at smooth surfaces. *Phys. Rev. Lett.* **2001**, *87* (9), 096105.